An embedded-FEM approach accounting for the size effect in nanocomposites

Dang Phong Bach, Delphine Brancherie, Ludovic Cauvin

To cite this version:

Dang Phong Bach, Delphine Brancherie, Ludovic Cauvin. An embedded-FEM approach accounting for the size effect in nanocomposites. Computational Mechanics, 2022, 70 (4), pp.745-762. 10.1007/s00466-022-02194-7 . hal-03721426

HAL Id: hal-03721426
https://utc.hal.science/hal-03721426v1

Submitted on 12 Jul 2022

An Embedded-FEM approach accounting for the size effect in nanocomposites

Journal:	*Computational Mechanics*
Manuscript ID	CM-21-0340.R1
Manuscript Type:	Original Paper
Date Submitted by the Author:	11-Mar-2022
Complete List of Authors:	BACH, Phong; Université de Technologie de Compiègne, Ingénierie mécanique BRANCHERIE, Delphine; Université de Techonologie de Compiègne - Laboratoire Roberval, Cauvin, Ludovic; Université de Techonologie de Compiègne - Laboratoire Roberval, Ingénierie mécanique
Keywords:	Nanocomposite, Size effect, Finite element method, Surface elasticity, homogenization

Computational Mechanics manuscript No.
(will be inserted by the editor)

An Embedded-FEM approach accounting for the size effect in nanocomposites

Dang Phong Bach · Delphine Brancherie · Ludovic Cauvin

Received: date / Accepted: date

Abstract A numerical approach based on the Embedded Finite Element Method (E-FEM) has been elaborated in order to model size effect in nanocomposites. For this purpose, the E-FEM standard Statically and Kinematically Optimal Nonsymmetric (SKON) formulation is enhanced to incorporate a surface elasticity at the interface between the matrix and the inclusions. The results obtained with the proposed approach for a couple of problems have been compared to analytical solutions and other numerical approaches. This study has been carried out considering both linear and nonlinear behaviors of the materials. The developed approach is shown to be an efficient tool for the evaluation and prediction of the mechanical behavior of nanocomposite materials.

Keywords Nanocomposite · Size effect · Finite element method · Surface elasticity · Homogenization

1 Introduction

Due to their remarkable physical properties (mechanical, electrical, ...), composite materials with nano-fillers, also known as nanocomposites, have raised a great interest over the last decade. One of the main features of nanocomposites compared to conventional composites is the so-called size effect they exhibit: for a given volume fraction of nano-fillers, the macroscopic behavior depends on the size of the fillers [1–5]. This size effect, due to local phenomena at the atomic scale [6, 7] is usually attributed to the increase of the ratio interface area to bulk volume. In the case of nanocomposites, the ratio between the interface regions and the bulk is much higher than for standard composites, the phenomena taking place at the interfacial regions are no longer negligible, leading to a modification of the macroscopic behavior of the material.

From the modeling point of view, the size effect can be modeled by adding an imperfect interface or interphase between the matrix and the inclusion. The estimation of the macroscopic and effective properties of the material are obtained based on advanced homogenization techniques. Since standard experimental setups are not able to access the local phenomena arising at the nano or even sub-nano (atomic) scales, Molecular Dynamic (MD) simulations are often employed to “identify” the model parameters needed in continuum mechanics based modelisation (see for instance [6, 8, 9] for interface parameters identification by MD simulations or [10–14] for interphase models).

Regarding analytical approaches, two different types of models are considered to account for the interfacial effects : either surface elasticity on zero-thickness interfaces [7, 15–22] or elastic non-zero thickness interphase [23, 24] are considered. The main limitation of all these studies remains in their restriction to quite simple shapes for the inclusions (spheres, cylinders, ...). Moreover, the extension of these approaches to non-linear behaviors is not straightforward. Several analytical efforts have been conducted to estimate the macroscopic yield strength of nanoporous materials [25–28]. Nevertheless, a complete model of nonlinear behaviors of

---

DP. Bach (✉) · D. Brancherie · L. Cauvin

Alliance Sorbonne Universités,
Université de Technologie de Compiègne,
Laboratoire Roberval FRE UTC-CNRS 2012 - Compiègne, France

E-mail: dang-phong.bach@utc.fr
delphine.brancherie@utc.fr
ludovic.cauvin@utc.fr

nanocomposite materials is still not easy to elaborate on from analytical solutions. The development of dedicated numerical approaches is, therefore, necessary to circumvent all these limitations. However, very few contributions are related to numerical description and implementation of such interface/interphase models in Finite Element (FE) codes. These developments are based mainly on the standard Finite Element method with the interface/surface-type element as in [29–31] or the eXtended Finite Element Method (X-FEM) in [32–35]. The evaluation of these two numerical approaches in the context of nanocomposite has been presented in our previous work [36].

We propose in the present paper an alternative numerical approach for modeling the size effect in nanocomposites. The proposed approach is based on the Embedded FEM (E-FEM) method usually used to handle strong discontinuities (see, for instance [37,38]) and less frequently to describe weak discontinuities [39, 40]. In this paper, we propose an extension of the E-FEM weak discontinuity version to the modelling of nanocomposites size effect with surface elasticity. To that purpose, we first compare the three E-FEM commonly considered formulations, namely, Statically and Kinematically Optimal Nonsymmetric (SKON), Statically Optimal Symmetric (SOS), and Kinematically Optimal Symmetric (KOS) in terms of numerical performances. Such formulations have been intensively compared in the literature for the case of strong discontinuities (see [41, 42]) but, to the best of our knowledge, such a comparison has never been conducted for the case of weak discontinuities. On the basis of this comparison, we propose an extension of the SKON formulation to account for surface elasticity. The surface linear elasticity theory of Gurtin [43] is then used to describe the tangential behavior of the interface and the equilibrium of the interface is given by the generalized Young-Laplace equation [44, 45]. The proposed approach is validated for linear elastic materials and extended to nonlinear behavior of the matrix and the inclusion.

The rest of the paper is organized as follows: the governing equations in the context of coherent interface are first presented in section 2. A two-field variational formulation of the problem suitable for embedded finite element (E-FEM) approximation is then provided, leading to a set of two equilibrium equations related to the global and the local level. Due to the introduction of surface elasticity on the interface, additional surface terms appear in both global and local equations. In section 3, we present the discretization technique and the resolution strategy for the adopted E-FEM approach. By using the “operator split method” and the “static condensation”, a standard FE problem is retrieved. In section 4, we present a comparative study of the three commonly adopted formulations for the E-FEM approach. This comparison in first carried out for the case of standard weak discontinuities. In section 5, we apply the proposed numerical approach to the case of nanocomposites with surface elasticity. The results related to convergence analysis, linear homogenization with periodic microstructure, and random microstructure are provided and compared to analytical solutions as well as to other numerical approaches. A very first application to nonlinear behavior of the matrix and inclusions is presented. Finally, in section 6, several conclusions and prospects are drawn.

2 Governing equations

In this section, we first present the problem of a two-phase composite material with coherent interface and its governing equations. In particular, we derive an enhanced assumed strain formulation of the problem in hand. On this basis and after introduction of dedicated E-FEM interpolations, the resulting discretised weak form of the problem is presented.

2.1 Equilibrium equations and boundary conditions

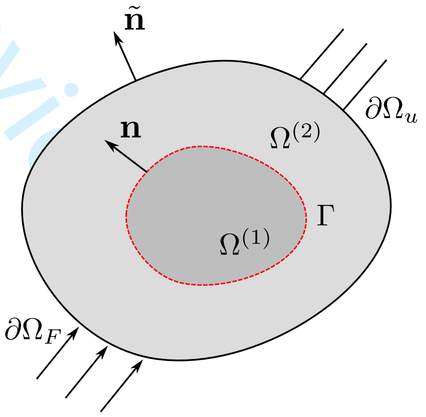

Fig. 1: Problem definition: two phases material with imperfect interface.

We consider a continuum bounded domain $\Omega \subset \mathbb{R}^d$ ($d = 2$ or 3), with boundary $\partial\Omega$ ($\partial\Omega = \partial\Omega_F \cup \partial\Omega_u$ and $\partial\Omega_F \cap \partial\Omega_u = \varnothing$). The outward unit normal to $\partial\Omega$ is denoted $\tilde{\mathbf{n}}$. This domain consists of two phases $\Omega^{(1)}$ and $\Omega^{(2)}$ which, in the rest of the paper, will denote inclusion and matrix, respectively. These two phases are partitioned by an imperfect interface Γ (see Fig.1). The unit normal vector to Γ is denoted as $\mathbf{n}$, its direction is conventionally taken from $\Omega^{(1)}$ towards $\Omega^{(2)}$. The jump of a quantity $\{\bullet\}$ over the interface is defined by $[\![\{\bullet\}]\!] = \{\bullet\}^{(1)} - \{\bullet\}^{(2)}$. The surface gradient and surface divergence operators are respectively defined by:

$$\nabla_s\{\bullet\} := \nabla\{\bullet\}\cdot\mathbf{P} \quad \text{and} \quad \mathbf{div}_s := \nabla_s\{\bullet\} : \mathbf{P}\ , \tag{1}$$

$$\text{with} \quad \mathbf{P} := \mathbf{I} - \mathbf{n}\otimes\mathbf{n}\ , \tag{2}$$

where $\mathbf{I}$ is the second-order unit tensor while $\mathbf{P}$ is the second-order projection operator on the interface Γ.

The bulk equilibrium equations in $\Omega^{(l)}$ $(l = 1, 2)$ are given by:

$$\mathbf{div}\boldsymbol{\sigma}^{(l)} + \mathbf{b} = \mathbf{0} \quad \text{in} \quad \Omega^{(l)},\ l = 1, 2\ . \tag{3}$$

where $\boldsymbol{\sigma}$ denotes the bulk Cauchy stress tensor and $\mathbf{b}$ denotes a volume force.

The Neumann and Dirichlet boundary conditions on $\partial\Omega$ are defined by:

$$\boldsymbol{\sigma}\cdot\tilde{\mathbf{n}} = \boldsymbol{F} \quad \text{on } \partial\Omega_F \quad \text{and} \quad \mathbf{u} = \bar{\mathbf{u}} \quad \text{on } \partial\Omega_u\ , \tag{4}$$

where $\boldsymbol{F}$ is the external force on $\partial\Omega_F$ and $\bar{\mathbf{u}}$ is the displacement prescribed on $\partial\Omega_u$.

An elastic coherent interface Γ is considered between the matrix $\Omega^{(2)}$ and the inclusion $\Omega^{(1)}$. According to the generalized Young-Laplace equation [44, 45] the equilibrium of the interface Γ is given by:

$$[\![\boldsymbol{\sigma}]\!]\cdot\mathbf{n} + \mathbf{div}_s\boldsymbol{\sigma}_s = \mathbf{0} \quad \text{on} \quad \Gamma\ , \tag{5}$$

where $\boldsymbol{\sigma}_s$ is the surface stress tensor.

Contrary to the classical continuum mechanics hypothesis, the generalized Young-Laplace equation allows a jump of the traction across the interface Γ. Using the decomposition of the traction jump vector into its normal and tangential components, Eq.(5) can be rewritten as:

$$\begin{cases} \mathbf{P}^{\perp}\cdot[\![\boldsymbol{\sigma}]\!]\cdot\mathbf{n} = -(\boldsymbol{\sigma}_s : \mathbb{K})\mathbf{n} \\ \mathbf{P}\cdot[\![\boldsymbol{\sigma}]\!]\cdot\mathbf{n} = -\mathbf{P}\cdot\mathbf{div}_s\boldsymbol{\sigma}_s \end{cases} \quad \text{on} \quad \Gamma\ . \tag{6}$$

The first equation of Eqs.(6) relates to the interface equilibrium in the normal direction where $\mathbf{P}^{\perp} := \mathbf{n}\otimes\mathbf{n}$ and $\mathbb{K}$ the curvature tensor defined by

$$\mathbb{K} = -\nabla_s\mathbf{n} = -\nabla\mathbf{n}\cdot\mathbf{P}\ . \tag{7}$$

The surface gradient of the normal vector gives the curvature tensor whose eigenvalues correspond to the principal curvatures of the interface. For 2D cases, the interface becomes a curved line and $\mathbb{K}$ admits the simple representation :

$$\mathbb{K} = \kappa\mathbf{P} = \frac{1}{R}\mathbf{P} \tag{8}$$

where κ and R are the curvature and the radius of curvature of the interface, respectively. In the case of a straight line interface $(R = \infty$ and $\kappa = 0)$, the right part of this equation vanishes even for non-zero interface stress. The second equation of Eqs.(6) expresses that the non-uniformity of the interface stress will cause the discontinuity of the bulk shear stress.

Combining the two equations of Eqs.(6) allows to rewrite Eq.(5) as follows:

$$[\![\boldsymbol{\sigma}]\!]\cdot\mathbf{n} + (\boldsymbol{\sigma}_s : \mathbb{K})\mathbf{n} + \mathbf{P}\cdot\mathbf{div}_s\boldsymbol{\sigma}_s = \mathbf{0} \quad \text{on} \quad \Gamma\ . \tag{9}$$

This form of the generalized Young-Laplace equation has been used in [21, 22] and will be used in the present work. In the classical case, the surface stress $\boldsymbol{\sigma}_s$ vanishes and Eqs.(5), (6) and (9) reduce to the standard traction continuity equation:

$$[\![\boldsymbol{\sigma}]\!]\cdot\mathbf{n} = \mathbf{0} \quad \text{on} \quad \Gamma\ . \tag{10}$$

According to the coherent interface model, there is no decohesion at the interface Γ so that, considering Hadamard's compatibility conditions, we have the following kinematic conditions on Γ:

$$\begin{cases} [\![\mathbf{u}]\!] = \mathbf{0}\ , \\ [\![\boldsymbol{\epsilon}]\!] = (\mathbf{a}\otimes\mathbf{n} + \mathbf{n}\otimes\mathbf{a}) \qquad \mathbf{a}\in\mathbf{R}^d\ . \end{cases} \tag{11}$$

2.2 Constitutive equations for the bulk and the interface

2.2.1 Linear elastic behavior

The bulk constitutive laws in the context of linear elasticity are given by:

$$\boldsymbol{\sigma} = \mathbb{C}^{(l)} : \boldsymbol{\epsilon} \quad \text{in} \quad \Omega^{(l)},\ (l = 1, 2)\ , \tag{12}$$

where $\mathbb{C}^{(l)}$ is the fourth-order elastic stiffness tensor associated with domain $\Omega^{(l)}$.

On the interface, we introduce a surface/interface elasticity as proposed by Gurtin and Murdoch [43] in the following form:

$$\boldsymbol{\sigma}_s = \tau_o\mathbf{I}_2 + 2(\mu_s - \tau_o)\boldsymbol{\epsilon}_s + (\lambda_s + \tau_o)\mathbf{tr}(\boldsymbol{\epsilon}_s)\mathbf{I}_2\ , \tag{13}$$

where $\boldsymbol{\epsilon}_s$ denotes the surface strain tensor, μ_s and λ_s are the surface Lame's constants characterizing the interface elasticity, $\mathbf{I}_2$ represents the surface second order identity tensor and τ_o is the surface tension. Eq.(13) is considered as the constitutive law of the interface and in the absence of τ_o, it can be written as:

$$\boldsymbol{\sigma}_s = \mathbb{C}^s : \boldsymbol{\epsilon}_s\ , \tag{14}$$

where $\mathbb{C}^s$ is the surface elastic stiffness tensor.

2.2.2 Non linear behavior

The bulk constitutive relations for nonlinear behaviors are written in an incremental form as:

$$\dot{\boldsymbol{\sigma}} = \mathbb{C}^{(l)} : \dot{\boldsymbol{\epsilon}} \qquad \text{in} \quad \Omega^{(l)},\ (l = 1, 2)\ , \tag{15}$$

with

$$\mathbb{C}^{(l)} = \begin{cases} \mathbb{C}^{(l)} & \text{elastic response} \\ \mathbb{C}^{ep} & \text{plastic response} \end{cases} \tag{16}$$

where $\mathbb{C}^{ep}$ is the elastoplastic tangent modulus computed following [46,47] at each iteration.

2.3 Weak form of the governing problem

2.3.1 Strain enhancement

As already mentioned, our goal, in this paper, is to derive an Embedded Finite Element formulation to account for the imperfect interface between the matrix and the inclusion. E-FEM interpolations are based on mixed type formulations with independent strains and displacements fields. Based on the Enhanced Assumed Strain approach [48], we derive the weak form of the problem previously presented in its strong form. In the Enhanced Assumed Strain approach (or equivalently in the so-called incompatible mode method [49]), the infinitesimal real strain field $\boldsymbol{\epsilon}$ is decomposed into the compatible part $\nabla^s \mathbf{u}$ and an added enhanced field denoted here as $\boldsymbol{\gamma}$:

$$\boldsymbol{\epsilon} = \nabla^s \mathbf{u} + \boldsymbol{\gamma} = \nabla^s \mathbf{u} + \boldsymbol{\gamma}_b + \boldsymbol{\gamma}_s \delta_\Gamma\ . \tag{17}$$

where $\boldsymbol{\gamma}_b$ is the enhanced bulk strain and $\boldsymbol{\gamma}_s$ is the enhanced surface strain on Γ. δ_Γ is defined as:

$$\delta_\Gamma = \begin{cases} 1 & \text{on} \quad \Gamma \\ 0 & \text{otherwise}\,. \end{cases} \tag{18}$$

The surface strain is the projection of the bulk strain on the tangential direction of the interface:

$$\begin{aligned} \boldsymbol{\epsilon}_s &= \mathbf{P} \cdot\ \boldsymbol{\epsilon} \cdot \mathbf{P} \qquad \text{on} \quad \Gamma \\ &= \mathbf{P} \cdot (\nabla^s \mathbf{u}) \cdot \mathbf{P} + \mathbf{P} \cdot \boldsymbol{\gamma}_b \cdot \mathbf{P} + \mathbf{P} \cdot \boldsymbol{\gamma}_s \cdot \mathbf{P}\ . \end{aligned} \tag{19}$$

According to the Hadamard's compatibility conditions (11), there is no strain jump in the tangential direction of the interface. The bulk strain enhancement in this direction is therefore unnecessary, so that: $\mathbf{P} \cdot \boldsymbol{\gamma}_b \cdot \mathbf{P} = \mathbf{0}$. The enhanced surface strain $\boldsymbol{\gamma}_s$ is defined on Γ, as a tangential superficial tensor field, therefore: $\boldsymbol{\gamma}_s = \mathbf{P} \cdot \boldsymbol{\gamma}_s \cdot \mathbf{P}$. The surface strain field can be then expressed in the form:

$$\boldsymbol{\epsilon}_s = \mathbf{P} \cdot (\nabla^s \mathbf{u}) \cdot \mathbf{P} + \boldsymbol{\gamma}_s \qquad \text{on} \quad \Gamma\ . \tag{20}$$

Following the idea of the Enhanced Assumed Strain method, not only the real but also the virtual strain field is enhanced in the same way.

$$\delta\boldsymbol{\epsilon} = \nabla^s \delta\mathbf{u} + \delta\boldsymbol{\gamma} = \nabla^s \delta\mathbf{u} + \delta\boldsymbol{\gamma}_b + \delta\boldsymbol{\gamma}_s \delta_\Gamma\ . \tag{21}$$

In the same manner, the virtual surface strain field is written in the form:

$$\delta\boldsymbol{\epsilon}_s = \mathbf{P} \cdot (\nabla^s \delta\mathbf{u}) \cdot \mathbf{P} + \delta\boldsymbol{\gamma}_s \qquad \text{on} \quad \Gamma\ . \tag{22}$$

2.3.2 Variational formulation with coherent interface

If we omit for a sake of simplicity the body force, the Hu-Washizu functional for $\Omega^{(1)}$, $\Omega^{(2)}$ are written in Eq. (23) and Eq. (24).

$$\Pi^{(1)}(\delta\mathbf{u},\, \delta\boldsymbol{\sigma},\, \delta\boldsymbol{\gamma}) = \int\limits_{\Omega^{(1)}} \left(\nabla^s \mathbf{u} : \boldsymbol{\sigma}^{(1)} - \boldsymbol{\epsilon} : \boldsymbol{\sigma}^{(1)} + \frac{1}{2}\boldsymbol{\epsilon} : \mathbb{C}^{(1)} : \boldsymbol{\epsilon} \right) d\Omega - \int\limits_{\Gamma} \mathbf{u} \cdot \left(\boldsymbol{\sigma}^{(1)} \cdot \mathbf{n} \right) d\Gamma - \int\limits_{\partial\Omega_F^{(1)} \setminus \Gamma} \mathbf{u} \cdot \mathbf{F} dS\ . \tag{23}$$

$$\Pi^{(2)}(\delta\mathbf{u},\, \delta\boldsymbol{\sigma},\, \delta\boldsymbol{\gamma}) = \int\limits_{\Omega^{(2)}} \left(\nabla^s \mathbf{u} : \boldsymbol{\sigma}^{(2)} - \boldsymbol{\epsilon} : \boldsymbol{\sigma}^{(2)} + \frac{1}{2}\boldsymbol{\epsilon} : \mathbb{C}^{(2)} : \boldsymbol{\epsilon} \right) d\Omega + \int\limits_{\Gamma} \mathbf{u} \cdot \left(\boldsymbol{\sigma}^{(2)} \cdot \mathbf{n} \right) d\Gamma - \int\limits_{\partial\Omega_F^{(2)} \setminus \Gamma} \mathbf{u} \cdot \mathbf{F} dS\ . \tag{24}$$

$$\Pi^{(s)}(\delta\mathbf{u},\, \delta\boldsymbol{\sigma}_s,\, \delta\boldsymbol{\gamma}) = \int\limits_{\Gamma} \left((\mathbf{P} \cdot \nabla^s \mathbf{u} \cdot \mathbf{P}) : \boldsymbol{\sigma}_s - \boldsymbol{\epsilon}_s : \boldsymbol{\sigma}_s + \frac{1}{2}\boldsymbol{\epsilon}_s : \mathbb{C}^s : \boldsymbol{\epsilon}_s \right) d\Gamma + \int\limits_{\Gamma} \mathbf{u} \cdot [\![\boldsymbol{\sigma}]\!] \cdot \mathbf{n} d\Gamma\ . \tag{25}$$

$$\begin{aligned} \Pi^{tot}(\delta\mathbf{u},\, \delta\boldsymbol{\sigma},\, \delta\boldsymbol{\sigma}_s,\, \delta\boldsymbol{\gamma}) = &\int\limits_{\Omega \setminus \Gamma} (\nabla^s \mathbf{u} : \boldsymbol{\sigma} - \boldsymbol{\epsilon} : \boldsymbol{\sigma} + \frac{1}{2}\boldsymbol{\epsilon} : \mathbb{C} : \boldsymbol{\epsilon}) d\Omega \quad + \\ &\int\limits_{\Gamma} \left((\mathbf{P} \cdot \nabla^s \mathbf{u} \cdot \mathbf{P}) : \boldsymbol{\sigma}_s - \boldsymbol{\epsilon}_s : \boldsymbol{\sigma}_s + \frac{1}{2}\boldsymbol{\epsilon}_s : \mathbb{C}^s : \boldsymbol{\epsilon}_s \right) d\Gamma - \int\limits_{\partial\Omega_F} \mathbf{u} \cdot \mathbf{F} dS\ . \end{aligned} \tag{26}$$

$$\forall(\delta\mathbf{u},\,\delta\boldsymbol{\sigma},\,\delta\boldsymbol{\sigma}_s,\,\delta\boldsymbol{\gamma})\begin{cases}\displaystyle\int\limits_{\Omega\setminus\Gamma}\nabla^s\delta\mathbf{u}:\hat{\boldsymbol{\sigma}}(\boldsymbol{\epsilon})\,d\Omega+\int\limits_{\Gamma}(\mathbf{P}\cdot\nabla^s\delta\mathbf{u}\cdot\mathbf{P}):\hat{\boldsymbol{\sigma}}_s(\boldsymbol{\epsilon}_s)\,d\Gamma-\int\limits_{\partial\Omega_F}\delta\mathbf{u}\cdot\mathbf{F}\,dS=\mathbf{0} & \text{(27a)}\\ \displaystyle\int\limits_{\Omega\setminus\Gamma}\delta\boldsymbol{\sigma}:\boldsymbol{\gamma}_b\,d\Omega=\mathbf{0} & \text{(27b)}\\ \displaystyle\int\limits_{\Gamma}\delta\boldsymbol{\sigma}_s:\boldsymbol{\gamma}_s\,d\Gamma=\mathbf{0} & \text{(27c)}\\ \displaystyle\int\limits_{\Omega\setminus\Gamma}\delta\boldsymbol{\gamma}_b:(\hat{\boldsymbol{\sigma}}(\boldsymbol{\epsilon})-\boldsymbol{\sigma})\,d\Omega+\int\limits_{\Gamma}\delta\boldsymbol{\gamma}_s:(\hat{\boldsymbol{\sigma}}_s(\boldsymbol{\epsilon}_s)-\boldsymbol{\sigma}_s)\,d\Gamma=\mathbf{0} & \text{(27d)}\end{cases}$$

$$\forall(\delta\mathbf{u},\,\delta\boldsymbol{\gamma})\begin{cases}\displaystyle\int\limits_{\Omega\setminus\Gamma}\nabla^s\delta\mathbf{u}:\hat{\boldsymbol{\sigma}}(\boldsymbol{\epsilon})\,d\Omega+\int\limits_{\Gamma}(\mathbf{P}\cdot\nabla^s\delta\mathbf{u}\cdot\mathbf{P}):\hat{\boldsymbol{\sigma}}_s(\boldsymbol{\epsilon}_s)\,d\Gamma-\int\limits_{\partial\Omega_F}\delta\mathbf{u}\cdot\mathbf{F}\,dS=\mathbf{0} & \text{(28a)}\\ \displaystyle\int\limits_{\Omega_e\setminus\Gamma_e}\delta\boldsymbol{\gamma}:\hat{\boldsymbol{\sigma}}(\boldsymbol{\epsilon})\,d\Omega+\int\limits_{\Gamma_e}\delta\boldsymbol{\gamma}_s:\hat{\boldsymbol{\sigma}}_s(\boldsymbol{\epsilon}_s)\,d\Gamma=\mathbf{0} & \text{(28b)}\end{cases}$$

Similarly, as we consider a coherent interface model, the surface elasticity energy has also to be taken into account. The interface contribution $\Pi^{(s)}$ of the interface Γ is written as in Eq. (25), where $[\![\boldsymbol{\sigma}]\!]\cdot\mathbf{n}=\left(\boldsymbol{\sigma}^{(1)}-\boldsymbol{\sigma}^{(2)}\right)\cdot\mathbf{n}$ acts like a body force along the interface.

By combining Eq.(23), Eq.(24) and Eq.(25), the total functional written on $\Omega^{(1)}\cup\Omega^{(2)}\cup\Gamma$ takes the form presented in Eq. (26).

With the fact that $\delta\boldsymbol{\gamma}=\delta\boldsymbol{\gamma}_b$ in $\Omega\setminus\Gamma$ and $\delta\boldsymbol{\gamma}{=}\delta\boldsymbol{\gamma}_s$ on Γ, the stationarity of Π^{tot} is written in Eq. (27) where $\hat{\boldsymbol{\sigma}}(\boldsymbol{\epsilon})$, $\hat{\boldsymbol{\sigma}}_s(\boldsymbol{\epsilon}_s)$ denote the bulk stress and the surface stress field obtained from the constitutive law of the bulk and the interface (linear and elastic in our case).

Following the idea of the Enhanced Assumed Strain method, the L_2-orthogonality between the stress fields and the enhanced strain fields is enforced. Hence, Eq. (27b) and Eq. (27c) are satisfied and in Eq. (27d), we have:

$$\int\limits_{\Omega\setminus\Gamma}\delta\boldsymbol{\gamma}_b:\boldsymbol{\sigma}\,d\Omega=\mathbf{0}\quad\text{and}\quad\int\limits_{\Gamma}\delta\boldsymbol{\gamma}_s:\boldsymbol{\sigma}_s\,d\Gamma=\mathbf{0}\,. \tag{29}$$

We finally end up with the system presented in Eq. (28).

3 Finite Element implementation

In this section, we present the finite element formulation built in the framework of E-FEM formulations. In particular, we detail the extension of the formulation to the case of elastic imperfect interfaces and the proposed enhancement of the strain field interpolation.

3.1 Strain fields interpolation

To build proper kinematic discontinuities, we can start from the displacement field and derive the strain enhancement. In the case of a weak discontinuity problem like the one on hand, the displacement field is continuous across the interface Γ separating the two phases $\Omega^{(1)}$ and $\Omega^{(2)}$ whereas the strain field is discontinuous. Let's consider an element (e) crossed by Γ, element (e) being composed of n nodes i $(i=1,...,n)$. We denote as $\mathbf{N}_i(\mathbf{x})$ the shape function associated to node i and $\mathbf{u}_i$ the corresponding nodal displacement vector.

The displacement field on element (e) can be written in the form:

$$\mathbf{u}^h(\mathbf{x})=\sum_{i=1}^{n}\mathbf{N}_i(\mathbf{x})\mathbf{u}_i+\mathbf{M}(\mathbf{x})\mathbf{a}\,, \tag{30}$$

where $\mathbf{M}(\mathbf{x})$ is an added shape function, continuous at Γ and $\mathbf{a}$ is a vector of additional local degrees of freedom.

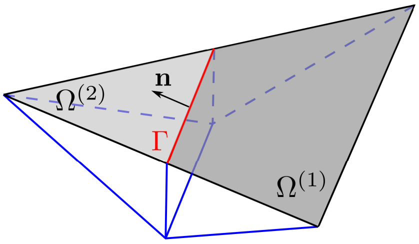

Fig. 2: Shape function $\mathbf{M}(\mathbf{x})$ in an enhanced element

Function $\mathbf{M}(\mathbf{x})$ is chosen consistent with a weak kinematic discontinuity in the form :

$$\mathbf{M}(\mathbf{x}) = \varphi(\mathbf{x})\mathcal{H}_\Gamma(\mathbf{x}) - \sum_{i \in \Omega^{(1)}} \mathbf{N}_i(\mathbf{x})\varphi_i \ , \tag{31}$$

where $\mathcal{H}_\Gamma$ denotes the Heaviside function defined as :

$$\mathcal{H}_\Gamma(\mathbf{x}) = \begin{cases} 0 & \text{if} \quad \mathbf{x} \in \Omega^{(2)} \\ 1 & \text{if} \quad \mathbf{x} \in \Omega^{(1)} \end{cases} \tag{32}$$

$\varphi(\mathbf{x})$ is here chosen to ensure that $\mathbf{M}(\mathbf{x})$ equals 0 on all nodes of the element. To allow for a strain discontinuity, the function $\varphi(\mathbf{x})$ is here chosen as the restriction to the element of the signed distance from $\mathbf{x}$ to the interface Γ, φ_i corresponds to the evaluation of $\varphi(\mathbf{x})$ on node i. With such a choice, the unit normal vector to the interface Γ is given by:

$$\mathbf{n}(\mathbf{x}_\Gamma) = \frac{\nabla\varphi}{||\nabla\varphi||}(\mathbf{x}_\Gamma) \ , \tag{33}$$

with $\mathbf{x}_\Gamma$ a point on Γ.

In this work, we choose linear triangular elements. To be consistent with the chosen interpolation, function φ is approximated by a linear function as:

$$\varphi^h(\mathbf{x}) = \sum_{i=1}^{n} \mathbf{N}_i(\mathbf{x})\varphi_i \tag{34}$$

such a choice leads to constant normal vector $\mathbf{n}^h$ per element corresponding to a linear approximation of the (eventually curved) interface. The normal vector to the interface is therefore constant in the considered element (see Fig. 2). Hence, the components of the normal vector $\mathbf{n}(\mathbf{x})$ can be evaluated at every point $\mathbf{x}$ in the considered element by:

$$\mathbf{n}(\mathbf{x}) = \frac{\nabla\varphi^h(\mathbf{x})}{||\nabla\varphi^h(\mathbf{x})||} \tag{35}$$

Considering Eq.(30) and the chosen expression for the added function $\mathbf{M}$, the real strain field can be written in the form:

$$\boldsymbol{\epsilon}(\mathbf{x}) = \underbrace{\mathbf{B}(\mathbf{x})\mathbf{u}}_{\nabla^s\mathbf{u}} + \underbrace{\mathbf{G}_r(\mathbf{x})\mathbf{a}}_{\gamma_b} \quad \text{in} \quad \Omega\backslash\Gamma \ , \tag{36}$$

with

$$\mathbf{G}_r(\mathbf{x}) = \mathbf{L}\mathbf{M}(\mathbf{x}) = \mathcal{N}\mathcal{H}_\Gamma(\mathbf{x}) - \sum_{i \in \Omega^{(1)}} \mathbf{B}_i(\mathbf{x})\varphi_i \ , \tag{37}$$

where $\mathbf{L}$ is the matrix operator associated with the symmetric gradient ∇^s and, following the Voigt notation, $\mathcal{N}$ is defined as (for 2D plane strain problems)

$$\mathcal{N} = \begin{bmatrix} n_x & 0 \\ 0 & n_y \\ n_y & n_x \end{bmatrix} . \tag{38}$$

Note that with such a definition, the enhanced part of the real strain tensor satisfies the kinematic conditions corresponding to a so-called weak discontinuity.

On the same way, the interpolation of the virtual strain field is defined as

$$\delta\boldsymbol{\epsilon}(\mathbf{x}) = \underbrace{\mathbf{B}(\mathbf{x})\delta\mathbf{u}}_{\nabla^s\delta\mathbf{u}} + \underbrace{\mathbf{G}_v(\mathbf{x})\delta\mathbf{a}}_{\delta\gamma_b} \quad \text{in} \quad \Omega\backslash\Gamma \ , \tag{39}$$

where $\mathbf{G}_v$ is built as a modified version of $\mathbf{G}_r$.

Based on the choice of the interpolation functions $\mathbf{G}_r$ and $\mathbf{G}_v$, the literature suggests three different formulations for E-FEM approaches:

- Kinematically Optimal Symmetric (KOS) which properly describes the kinematic aspect, where:

$$\gamma_b = \mathbf{G}_r\mathbf{a} \qquad \text{and} \qquad \delta\gamma_b = \mathbf{G}_r\delta\mathbf{a} \, . \tag{40}$$

- Statically Optimal Symmetric (SOS) which nicely satisfies the static equilibrium condition, where:

$$\gamma_b = \mathbf{G}_v\mathbf{a} \qquad \text{and} \qquad \delta\gamma_b = \mathbf{G}_v\delta\mathbf{a} \, . \tag{41}$$

- Statically Kinematically Optimal Nonsysmetric (SKON) which allows representing both aspects of statics and kinematics, where:

$$\gamma_b = \mathbf{G}_r\mathbf{a} \qquad \text{and} \qquad \delta\gamma_b = \mathbf{G}_v\delta\mathbf{a} \, . \tag{42}$$

$\mathbf{G}_v$ can be obtained by following the procedure proposed for the method of incompatible modes [50] leading to :

$$\mathbf{G}_v(\mathbf{x}) = \mathbf{G}_r(\mathbf{x}) - \frac{1}{V}\int_{\Omega^e} \mathbf{G}_r(\mathbf{x})d\Omega \, . \tag{43}$$

We then obtain, for three nodes triangular elements :

$$\begin{aligned} \mathbf{G}_v^{(1)}(\mathbf{x}) &= \frac{V^{(2)}}{V}\mathcal{N} \quad \text{in} \quad \Omega^{(1)} \\ \mathbf{G}_v^{(2)}(\mathbf{x}) &= -\frac{V^{(1)}}{V}\mathcal{N} \quad \text{in} \quad \Omega^{(2)} \ , \end{aligned} \tag{44}$$

where $V^{(1)}$ and $V^{(2)}$ denotes the volume (for 3D problems or area for 2D problems) of $\Omega^{(1)}$ and $\Omega^{(2)}$, respectively.

The three formulations have already been tested in the context of the E-FEM methods for the description of cohesive interfaces in [41]. It has been shown that SKON has better performances than the corresponding symmetrical formulations (SOS and KOS). For the case of weak discontinuities with coherent interfaces as we consider in the present work, a comparison in terms of numerical performances of these three formulations is presented in section 4.

As regards the interpolations, the surface strains associated with the interface Γ are built in a very similar way as for the bulk (see Eq. (36) and Eq. (39)):

$$\begin{aligned} \boldsymbol{\epsilon}_s^h &= \mathcal{M}\mathbf{B}\mathbf{u} + \mathbf{G}_{rs}\mathbf{a} \quad \text{on} \quad \Gamma \,, \\ \delta\boldsymbol{\epsilon}_s^h &= \mathcal{M}\mathbf{B}\delta\mathbf{u} + \mathbf{G}_{vs}\delta\mathbf{a} \text{ on } \quad \Gamma \,. \end{aligned} \tag{45}$$

where matrix $\mathcal{M}$ is defined as :

$$\mathcal{M} = \begin{bmatrix} P_{11}^2 & P_{12}^2 & P_{11}P_{12} \\ P_{12}^2 & P_{22}^2 & P_{12}P_{22} \\ 2P_{11}P_{12} & 2P_{12}P_{22} & (P_{12}^2 + P_{11}P_{22}) \end{bmatrix} , \tag{46}$$

with P_{11}, P_{12}, P_{22} the components of the projection tensor $\mathbf{P}$.

The expressions of $\mathbf{G}_{rs}$, $\mathbf{G}_{vs}$ will be discussed in the next subsection where they are used to describe the equilibrium of the interface, given by the generalized Young-Laplace equation Eq. (9).

3.2 Finite Element formulation and resolution strategy

Introducing Eq. (36), Eq. (39) and Eq. (45) into the system of equations (28), the discretized problem reads as follows:

$$\mathop{\mathrm{A}}_{e=1}^{N\text{elem}} [\mathbf{f}_{int}^{\Omega_e \setminus \Gamma_e} + \mathbf{f}_{int}^{\Gamma_e} - \mathbf{f}_{ext}^{e}] = \mathbf{0} \,, \tag{47}$$

$$\mathbf{h}_e = \int_{\Omega_e^{(1)}} (\mathbf{G}_v^{(1)})^T \hat{\boldsymbol{\sigma}}^{(1)} \, d\Omega + \int_{\Omega_e^{(2)}} (\mathbf{G}_v^{(2)})^T \hat{\boldsymbol{\sigma}}^{(2)} \, d\Omega + \int_{\Gamma_e} \mathbf{G}_{vs}^T \hat{\boldsymbol{\sigma}}_s \, d\Gamma = \mathbf{0} \quad \forall e \text{ cut by } \Gamma \,, \tag{48}$$

where $\mathop{\mathrm{A}}_{e=1}^{N\text{elem}}$ denotes the assembly process and with

$$\mathbf{f}_{int}^{\Omega_e \setminus \Gamma_e} = \int_{\Omega_e^{(1)}} \mathbf{B}^T \mathbf{C}^{(1)} \left(\mathbf{B}\mathbf{u} + \mathbf{G}_r^{(1)}\mathbf{a} \right) d\Omega + \int_{\Omega_e^{(2)}} \mathbf{B}^T \mathbf{C}^{(2)} \left(\mathbf{B}\mathbf{u} + \mathbf{G}_r^{(2)}\mathbf{a} \right) d\Omega \,, \tag{49}$$

$$\mathbf{f}_{int}^{\Gamma_e} = \int_{\Gamma_e} \mathbf{B}^T \mathcal{M}^T \mathbf{C}^{(s)} \left(\mathcal{M}\mathbf{B}\mathbf{u} + \mathbf{G}_{rs}\mathbf{a} \right) d\Gamma \,, \tag{50}$$

$$\mathbf{f}_{ext}^{e} = \int_{\Omega_e} \mathbf{N}^T \mathbf{b} d\Omega + \int_{\partial\Omega_F} \mathbf{N}^T \mathbf{F} dS \,, \tag{51}$$

Due to the form of the interpolation of the enhanced strain fields, Eq. (48) is an elementary equation solved independently on each element crossed by the interface Γ. Taking into account the expression of $\mathbf{G}_v$ Eq. (44), we obtain the following local equation:

$$\mathbf{h}_e = \frac{V^{(2)}}{V} \int_{\Omega_e^{(1)}} \mathcal{N}^T \hat{\boldsymbol{\sigma}}^{(1)} d\Omega - \frac{V^{(1)}}{V} \int_{\Omega_e^{(2)}} \mathcal{N}^T \hat{\boldsymbol{\sigma}}^{(2)} d\Omega + \int_{\Gamma_e} \mathbf{G}_{vs}^T \hat{\boldsymbol{\sigma}}_s d\Gamma = \mathbf{0} \,. \tag{52}$$

With the fact that we consider here 3 nodes triangular elements, where the stress fields are constant both in the bulks $\Omega_e^{(1)}$ and $\Omega_e^{(2)}$ and the interface Γ, Eq.(52) becomes :

$$\frac{V^{(2)}V^{(1)}}{V} \mathcal{N}^T [\![\hat{\boldsymbol{\sigma}}]\!] + A\mathbf{G}_{vs}^T \hat{\boldsymbol{\sigma}}_s = \mathbf{0} \,, \tag{53}$$

where A is the length (surface in 3D case) of the portion of Γ crossing the considered element.

The interpolation function $\mathbf{G}_{vs}$ will be chosen to ensure that the local equation (52) corresponds to the equilibrium equation of the coherent interface, namely the generalized Young-Laplace (Eq. (9)). We can notice that $\mathcal{N}^T [\![\hat{\boldsymbol{\sigma}}]\!]$ is the Voigt's notation of $[\![\hat{\boldsymbol{\sigma}}]\!] \mathbf{n}$. Since $\hat{\boldsymbol{\sigma}}_s$ and $\mathbb{K}$ are symmetric tensors, combining Eq. (9) and Eq. (53) leads to:

$$\frac{V^{(2)}V^{(1)}}{V} \left[\mathbf{n}\mathcal{K}^T \hat{\boldsymbol{\sigma}}_s + \mathbf{P}\mathbf{div}_s(\hat{\boldsymbol{\sigma}}_s) \right] = A\mathbf{G}_{vs}^T \hat{\boldsymbol{\sigma}}_s \,, \tag{54}$$

where $\mathcal{K}$ is the Voigt's notation of the curvature tensor $\mathbb{K}$.

For the three nodes triangular element, the surface stress is constant, and Eq. (54) is written at the element level. Therefore, the surface divergence of the interface stress $\mathbf{div}_s\boldsymbol{\sigma}_s$ vanishes :

$$\frac{V^{(2)}V^{(1)}}{V} \mathbf{n}\mathcal{K}^T \hat{\boldsymbol{\sigma}}_s = A\mathbf{G}_{vs}^T \hat{\boldsymbol{\sigma}}_s \,. \tag{55}$$

It should be pointed out here that the non-uniform distribution of the interface stress (related to $\mathbf{div}_s\boldsymbol{\sigma}_s$) is taken into account at the global level through the global equilibrium equation (47). We obtain the expression of $\mathbf{G}_{vs}$ in the form:

$$\mathbf{G}_{vs} = \frac{V^{(2)}V^{(1)}}{VA} \mathcal{K}\mathbf{n}^T \,. \tag{56}$$

For 3D case, the curvature tensor $\mathcal{K}$ can be determined through the radii of curvature (in different directions) of the interface. For 2D case, introducing (8) in Eq. (56) gives:

$$\mathbf{G}_{vs} = \frac{V^{(2)}V^{(1)}}{VA} \frac{1}{R} \mathcal{P}\mathbf{n}^T \,, \tag{57}$$

where $\mathcal{P}$ is the Voigt's notation of $\mathbf{P}$.

It can be pointed out here that the computation of $\mathbf{G}_{vs}$ requires the geometrical features of the interface (curvature tensor $\mathcal{K}$, or radius R). In the general case where the radius of curvature is not available or when the interface changes its shape with respect to time as in fluid mechanics, the value of the radius of curvature can be numerically estimated through the nodal values of the signed distance to the interface (level-set) [51], denoted in this paper as $\varphi(\mathbf{x})$ (see Eq. (34)).

In the bulk, where the SKON formulation is employed, $\mathbf{G}_r$ is built in order to ensure the kinematic compatibility condition (between the enhanced strain and the displacement field) while $\mathbf{G}_v$ is built to imply the satisfaction of the traction continuity condition as well as the patch test (see [48]). On the interface, the kinematic compatibility condition is not required since the interface is not explicitly discretized. Therefore, the SOS formulation (see Eq. (41)) is used here for the interface:

$$\mathbf{G}_s = \mathbf{G}_{rs} = \mathbf{G}_{vs} = \frac{V^{(2)}V^{(1)}}{VA}\frac{1}{R}\mathcal{P}\mathbf{n}^T \; . \tag{58}$$

All these interpolations $\mathbf{G}_r, \mathbf{G}_v$ and $\mathbf{G}_s$ (Eqs. (37), (44), and (58)) allow to rewrite Eq. (47) and Eq. (48) in the following matrix form:

$$\begin{cases} \mathop{\mathrm{A}}\limits_{e=1}^{Nelem} \left(\mathbf{K}^e_{uu}\,\mathbf{u} + \mathbf{K}^e_{ua}\,\mathbf{a}\right) = \mathop{\mathrm{A}}\limits_{e=1}^{Nelem} \mathbf{f}^e_{ext} & \text{(59a)} \\ \mathbf{K}^e_{\mathrm{au}}\,\mathbf{u} + \mathbf{K}^e_{aa}\,\mathbf{a} = \mathbf{h}_e \quad \forall e \text{ cut by } \Gamma & \text{(59b)} \end{cases}$$

where

$$\begin{aligned} \mathbf{K}^e_{uu} &= \int_{\Omega_e^{(1)}} \mathbf{B}^T\mathbf{C}^{(1)}\mathbf{B}\,d\Omega + \int_{\Omega_e^{(2)}} \mathbf{B}^T\mathbf{C}^{(2)}\mathbf{B}\,d\Omega \\ &\quad + \int_{\Gamma_e} \mathbf{B}^T\mathcal{M}^T\mathbf{C}^{(s)}\mathcal{M}\mathbf{B}\,d\Gamma \; , \\ \mathbf{K}^e_{ua} &= \int_{\Omega_e^{(1)}} \mathbf{B}^T\mathbf{C}^{(1)}\mathbf{G}_r^{(1)}\,d\Omega + \int_{\Omega_e^{(2)}} \mathbf{B}^T\mathbf{C}^{(2)}\mathbf{G}_r^{(2)}\,d\Omega \\ &\quad + \int_{\Gamma_e} \mathbf{B}^T\mathcal{M}^T\mathbf{C}^{(s)}\mathbf{G}_s\,d\Gamma \; , \\ \mathbf{K}^e_{au} &= \int_{\Omega_e^{(1)}} (\mathbf{G}_v^{(1)})^T\mathbf{C}^{(1)}\mathbf{B}\,d\Omega + \int_{\Omega_e^{(2)}} (\mathbf{G}_v^{(2)})^T\mathbf{C}^{(2)}\mathbf{B}\,d\Omega \\ &\quad + \int_{\Gamma_e} \mathbf{G}_s^T\mathbf{C}^{(s)}\mathcal{M}\mathbf{B}\,d\Gamma \; , \\ \mathbf{K}^e_{aa} &= \int_{\Omega_e^{(1)}} (\mathbf{G}_v^{(1)})^T\mathbf{C}^{(1)}\mathbf{G}_r^{(1)}\,d\Omega \\ &\quad + \int_{\Omega_e^{(2)}} (\mathbf{G}_v^{(2)})^T\mathbf{C}^{(2)}\mathbf{G}_r^{(2)}\,d\Omega + \int_{\Gamma_e} \mathbf{G}_s^T\mathbf{C}^{(s)}\mathbf{G}_s\,d\Gamma \; , \end{aligned} \tag{60}$$

$\mathbf{C}^{(1)}$, $\mathbf{C}^{(2)}$,$\mathbf{C}^{(s)}$ correspond to the matrix form of the elastic tensor for phase (1), phase (2) and the interface Γ, respectively ($l = 1, 2, s$).

$$\mathbf{C}^{(l)} = \begin{bmatrix} (\lambda^{(l)} + 2\mu^{(l)}) & \lambda^{(l)} & 0 \\ \lambda^{(l)} & (\lambda^{(l)} + 2\mu^{(l)}) & 0 \\ 0 & 0 & \mu^{(l)} \end{bmatrix} . \tag{61}$$

The system (59) is solved by taking advantage of the fact that equations (59b) are written at the element level. An "operator split" method is then considered for the resolution: equation (59b) is solved at the element level in order to obtain the variables $\mathbf{a}$ for each element crossed by the interface, then, after a static condensation procedure [52] at the element level, nodal displacements $\mathbf{u}$ are obtained as solution of:

$$\mathop{\mathrm{A}}\limits_{e=1}^{Nelem} \widetilde{\mathbf{K}}^e\mathbf{u} = \mathop{\mathrm{A}}\limits_{e=1}^{Nelem} \mathbf{f}^e_{ext} \tag{62}$$

with

$$\widetilde{\mathbf{K}}^e = \mathbf{K}^e_{uu} - \mathbf{K}^e_{ua}(\mathbf{K}^e_{aa})^{-1}\mathbf{K}^e_{au} \; . \tag{63}$$

Due to static condensation, the size of the final global system (62) to be solved is not modified from the standard FEM code. Hence, no matter how many inclusions and interfaces exist in the RVE, the size of the problem is preserved and only depends on the number of nodes of the mesh.

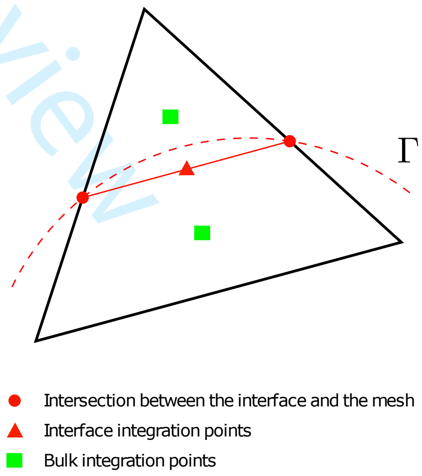

Fig. 3: Element cut by the interface Γ, approximated interface and integration points in E-FEM.

As the enrichment does not affect the degree of interpolation of the fields in the element (contrary to X-FEM enrichment), the numerical integration procedure only needs one integration point for each subdomain in the considered element (see Fig.3).

4 Performance of the three E-FEM formulations

In this section, we aim at comparing the numerical performance of the three E-FEM formulations usually considered in the literature and referred to as SOS (Statically Optimal Symmetric), KOS (Kinematically Optimal Symmetric), and SKON (Statically Kinematically Optimal Nonsysmetric). Such comparisons have already been conducted in the case of strong discontinuities, leading to the conclusion that, for linear elements, the SKON formulation gives the best results regarding the convergence and alleviates all the difficulties due to stress locking [41, 42]. Since we consider, in this work, weak discontinuities, the classical first Eshelby problem and two phases problem are chosen to test the efficiency of the three formulations.

The interface is here considered as a perfect interface, no surface elasticity is taken into account. In that case, the generalized Young-Laplace equation (Eqs. (5), (6) and (9)) reduces to the standard traction continuity $[\![\boldsymbol{\sigma}]\!] \cdot \mathbf{n} = \mathbf{0}$.

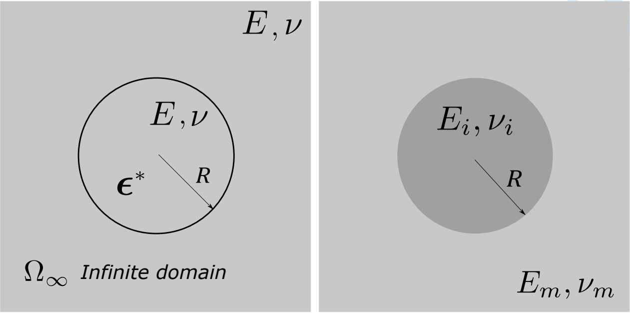

(a) Eshelby problem (b) Two phases

Fig. 4: Classical first Eshelby problem and two phases problem ($R = 1nm, f = 0.2$).

For the Eshelby problem, we consider a bounded domain surrounding a cylindrical inclusion (see Fig. 4a) and we conduct the computations by prescribing the analytical solution in terms of displacements on the boundary of the finite domain. In the results presented in this section, the loading conditions correspond to a dilational eigenstrain $\boldsymbol{\epsilon}^*$ prescribed to the inclusion and such that $\epsilon^* = \epsilon^*_{11} = \epsilon^*_{22} = 0.5\%, \epsilon^*_{33} = 0$. The Young modulus E of the material is set to 3 GPa and the Poisson ratio is set to 0.3.

For the two phases problem, the considered RVE represented in 4b is considered and subjected to an hydrostatic stress by prescribing, on the boundary of the domain, the exact solution in terms of displacement given in [53]. The material constants are chosen as: $E_i = 1$ GPa, $\nu_i = 0.25$, and $E_m = 10$ GPa, $\nu_m = 0.3$.

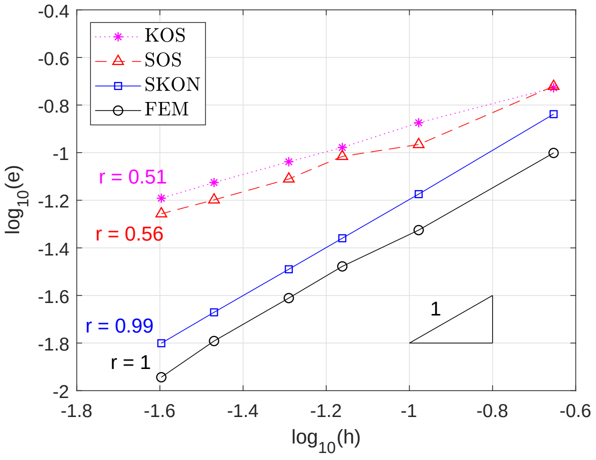

(a) Eshelby problem

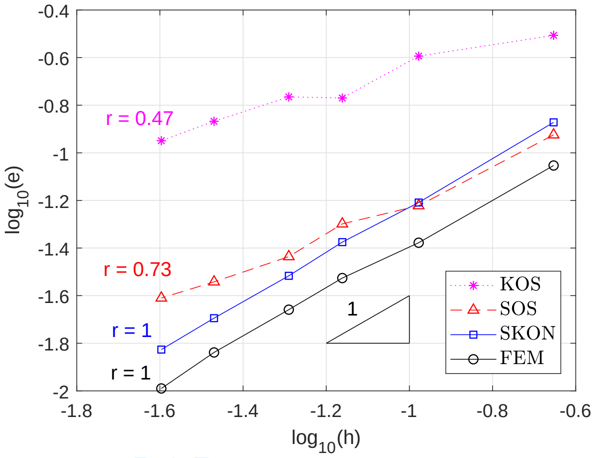

(b) Two phases material

Fig. 5: Convergence analysis of three formulations of E-FEM in treating the first Eshelby problem and the two phases material problem.

The performance of the different numerical approaches is evaluated through the error and convergence rate. The error is computed as the relative energy norm error of the difference between the exact solution given in [53] and the numerical solution:

$$\mathrm{e} = \sqrt{\frac{\int_\Omega (\boldsymbol{\epsilon}^h(\mathbf{x}) - \boldsymbol{\epsilon}(\mathbf{x})) : \mathbb{C} : (\boldsymbol{\epsilon}^h(\mathbf{x}) - \boldsymbol{\epsilon}(\mathbf{x}))\, \mathrm{d}\Omega}{\int_\Omega \boldsymbol{\epsilon}(\mathbf{x}) : \mathbb{C} : \boldsymbol{\epsilon}(\mathbf{x}) \mathrm{d}\Omega}}, \quad (64)$$

where $\boldsymbol{\epsilon}^h$ is the computed strain and $\boldsymbol{\epsilon}$ is the analytical solution. The results of conforming FEM is also added to the comparison as a reference result.

As shown in Fig. 5, the convergence of the SKON formulation is the best among the three formulations of E-FEM. The expected conforming FEM rate of convergence r = 1 is recovered for SKON. Nevertheless, most of the works based on E-FEM for the representation of weak discontinuities consider a SOS formulation [39,40] for its performance in ensuring the traction continuity condition.

5 Numerical results

Based on the performance test above, we will consider a SKON formulation for the next numerical examples incorporating a surface elasticity. The results of the proposed numerical approach will be validated and exploited for both linear and nonlinear behaviors of material.

5.1 Eshelby problem with surface elasticity

This first example aims at validating the proposed numerical approach on the Eshelby problem with surface elasticity (see Fig.6a). The considered problem corresponds to a cylindrical inclusion immersed in an infinite elastic domain. An elastic interface is introduced between the infinite domain and the inclusion. As for the classical Eshelby problem, a uniform dilational eigenstrain $\boldsymbol{\epsilon}^*$ is prescribed in the inclusion. We consider here that $\epsilon^* = \epsilon^*_{11} = \epsilon^*_{22} = 0.5\%, \epsilon^*_{33} = 0$. The Young modulus E of the material is set to 3 GPa and the Poisson ratio to 0.3. For the numerical computation, only a bounded domain is considered around the inclusion and the analytical solution [15–18] in terms of displacements is prescribed on the boundary of the finite domain. The convergence analysis obtained from the proposed approach is compared to those of two numerical approaches available in the literature namely the "Interface element" approach and the X-FEM approach (see meshes in Figs. 6c, 6d, 6e), which have been studied in our previous work [36].

Fig.7 presents the comparison in terms of convergence rate and efficiency of the three numerical approaches for the case without ($k_s = 0$ N/m) and with surface elasticity ($k_s = 6.092$ N/m corresponding to $\lambda_s = 6.842$ N/m, $\mu_s = -0.375$ N/m [6]). It can be seen that the convergence of E-FEM and "Interface element" is not affected by the presence of surface elasticity, the expected rate of convergence r ≈ 1 is recovered whatever the surface elasticity parameters. The accuracy of the three strategies involved in this comparison shows that the E-FEM solution is slightly less accurate than the "Interface element" solution. The degradation of the convergence rate of the X-FEM method, when surface elasticity is considered, has been reported in [32,36].

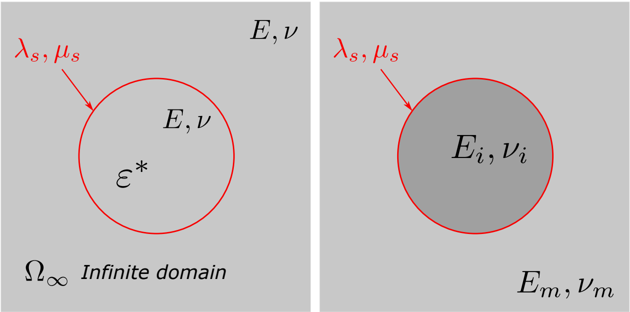

(a) Eshelby problem (b) Two-phases material

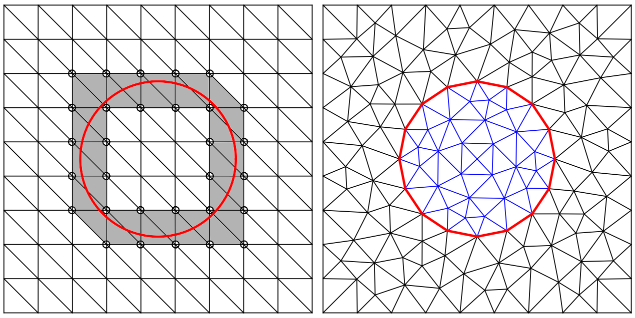

(c) X-FEM mesh (d) Interface element

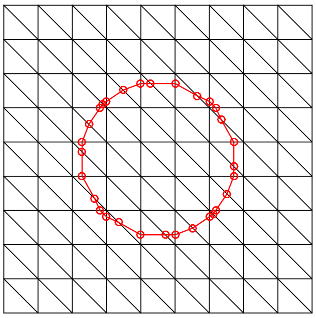

(e) E-FEM mesh

Fig. 6: Surface elasticity is taken into account in the plane strain model.

5.2 Two phases nanomaterial

In the following, we consider the problem of the linear homogenization of a two phases material with coherent interfaces. Homogenization is performed assuming a periodic microstructure (see Fig. 8a), the considered RVE is the unit-cell represented in Fig. 6b. The chosen material properties are as follows: $\nu_m = \nu_i = 0.32$, $E_m = 70$ GPa, $E_i = 7$ GPa and $\lambda_s = 6.842$ N/m, $\mu_s = -0.375$ N/m (corresponding to $k_s = 6.092$ N/m). The computation of the effective bulk modulus is based on the total deformation energy (bulk energy + interface en-

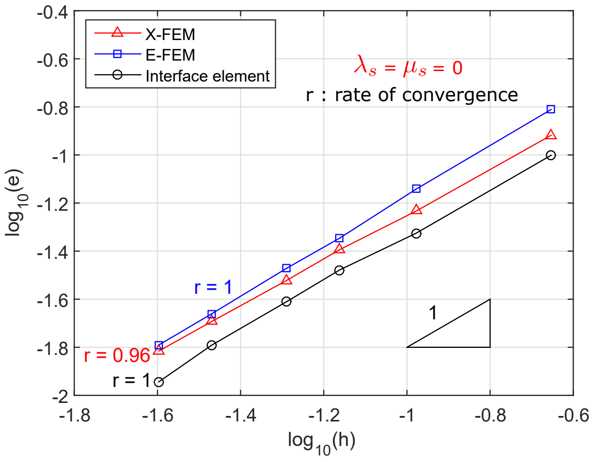

(a) Without surface elasticity

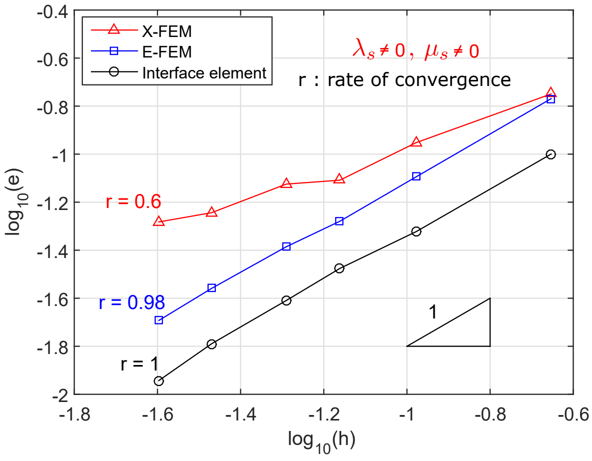

(b) With surface elasticity

Fig. 7: Convergence analysis for the Eshelby problem with and without surface elasticity for the three methods: E-FEM, X-FEM, and Interface element.

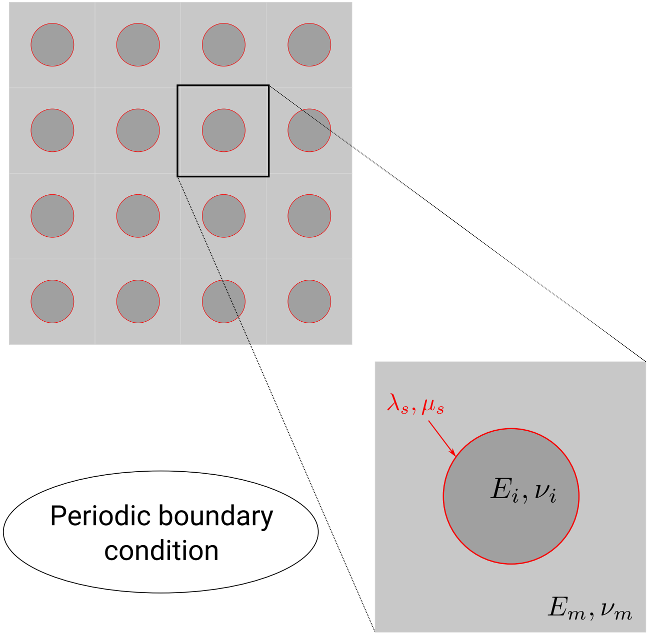

(a) Periodic microstructure

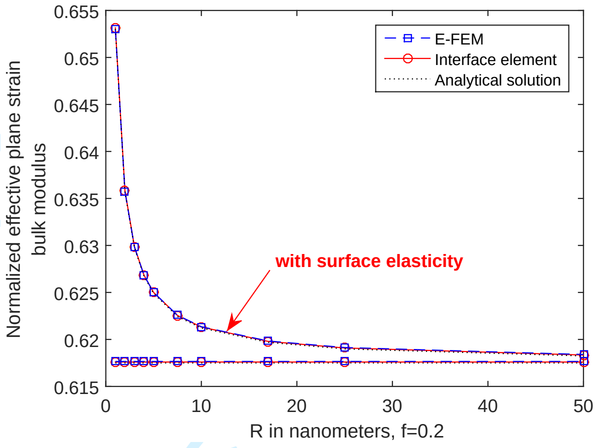

(b) Normalized effective bulk modulus

Fig. 8: Size effect in effective plane-strain bulk modulus for circular inclusion ($f = 0,2$, $E_m = 70$ GPa, $E_i = 0,1E_m$, $\nu_m = \nu_i = 0,32$).

ergy) and the assumption of isotropic effective properties. The normalized effective bulk modulus obtained for the cases with and without surface elasticity versus inclusion radius for a fixed volume fraction $f = 0.2$ is presented in Fig. 8b. An excellent agreement not only between the numerical approaches (E-FEM and Interface element) but also between numerical and analytical results (GSCM model, Le Quang and He [20]) is observed. On a physical point of view, it may be noticed that the size effect observed for the case accounting for surface elasticity is more pronounced for a small radius of the nano-inclusions.

As mentioned in the introduction, the limitation of analytical solutions remains on the fact that only the simple shapes (circular) of inclusions can be considered. In order to show the ability of the numerical approach in dealing with more complex geometries, several cases with ellipse and non-convex arbitrary shapes of inclusions are considered in the following. In these cases, for the purposes of the comparison, we have chosen to construct an effective "bulk modulus" on the basis of the isotropy assumption although that may not be the case for arbitrary microstructures. Note that this choice does not affect the conclusions on the observed size effects.

For the case of an ellipse cylindrical inclusion with $a = 2b$ (a : major axis, b : minor axis) presented in Fig. 9a, we recall that the radius of curvature of any point

$C(x, y)$ on the ellipse is calculated by

$$R_c = \frac{a^2}{b}\left(1 - \frac{(a^2 - b^2)x^2}{a^4}\right)^{3/2} \quad . \tag{65}$$

No analytical results for the case of ellipse cylindrical inclusions are available in the literature, the results obtained with the "Interface element" are therefore used as reference results. The normalized effective bulk modulus versus the minor axis b of the ellipse inclusion is shown in Fig. 9b.

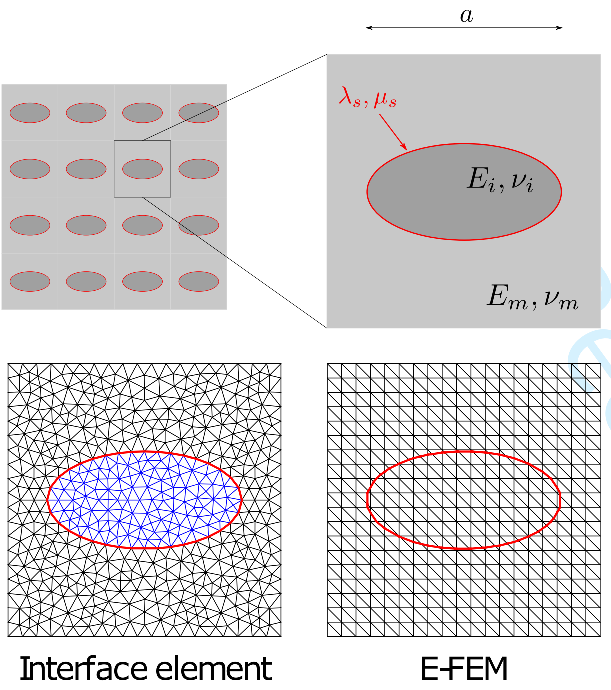

(a) Ellipse cylindrical inclusions

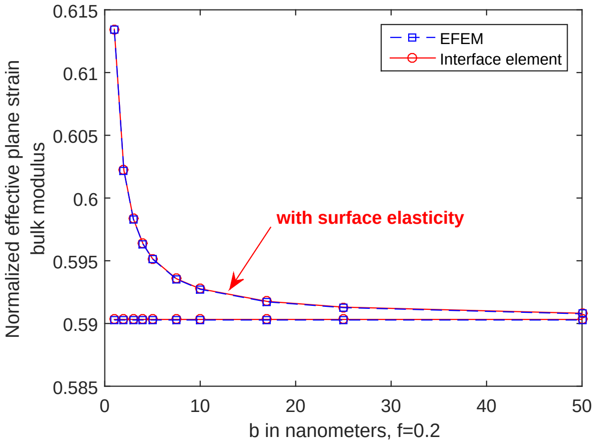

(b) Normalized effective bulk modulus

Fig. 9: Size effect in effective plane-strain bulk modulus for ellipse inclusion ($f = 0.2$, $E_m = 70$ GPa, $E_i = 0.1E_m$, $\nu_m = \nu_i = 0.32$).

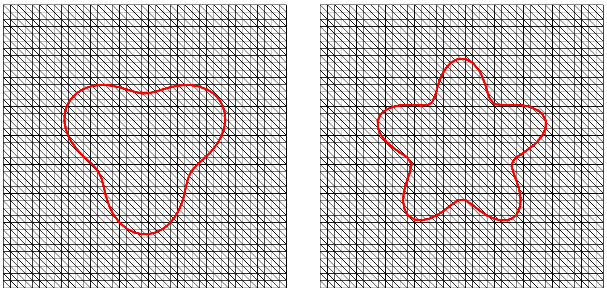

(a) $A = 0.25R_o$ and $B = 3$ (b) $A = 0.25R_o$ and $B = 5$

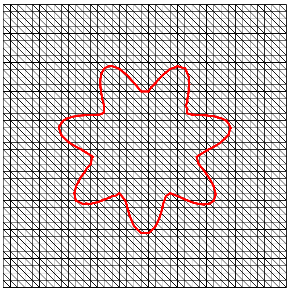

(c) $A = 0.25R_o$ and $B = 7$

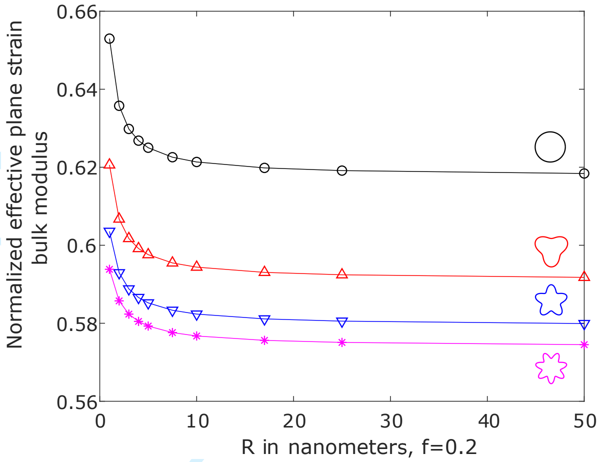

(d) Normalized effective bulk modulus

Fig. 10: Size effect and shape dependence in normalized effective bulk modulus ($f = 0.2$, $E_m = 70$ GPa, $E_i = 0.1E_m$, $\nu_m = \nu_i = 0.32$).

With the proposed approach, it is possible to introduce imperfect interfaces accounting for surface energy even for complex inclusion shapes. For this purpose, we also investigate non-convex arbitrary shapes of inclusions. To that end, the following radius function is used

$$R(\alpha) = R_o + Asin(B\alpha), \quad \alpha = [0, 2\pi[\; , \tag{66}$$

with R_o the reference radius. A and B are deterministic constants which define the amplitude and the period of oscillations of the radius with the angular position α.

With this function, the area of the inclusion is given as:

$$V = \frac{4A^2B\pi + 8AR_o + 8B\pi R_o^2 - 8AR_o cos(2B\pi)}{8B} + \frac{A^2 sin(4B\pi)}{8B} . \tag{67}$$

We choose here $A = 0.25R_o$ and $B \in [3, 5, 7]$. The shapes corresponding to these choices are presented in Figs. 10a, 10b, 10c. Due to the complexity of the geometry, analytical solutions are no more available. We observe in Fig. 10d a great influence of the inclusion shape on the effective bulk modulus. For a fixed volume fraction, a decrease of the bulk modulus according to the increase of the number of oscillations can be reported. This tendency has also been shown both with the X-FEM approach in [32] and FEM-based conformal mapping techniques in [54]. Moreover, we can note that the size effect for different shapes of inclusion is clearly shown.

5.3 Random microstrutures

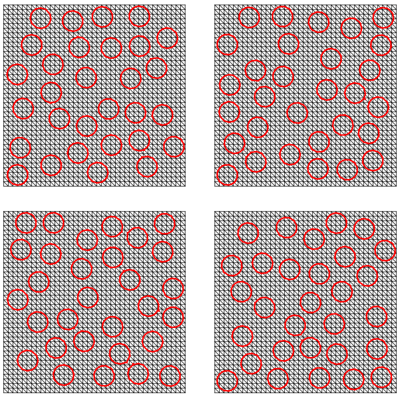

(a) E-FEM

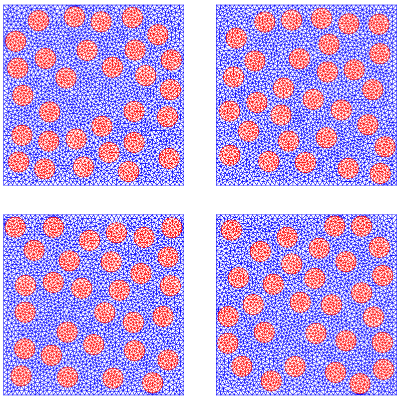

(b) Interface element

Fig. 11: Several samples for 30 randomly distributed nano-inclusions.

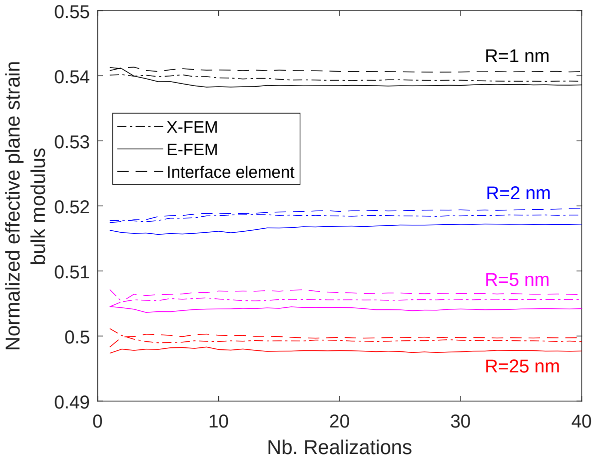

(a) Statistical convergence

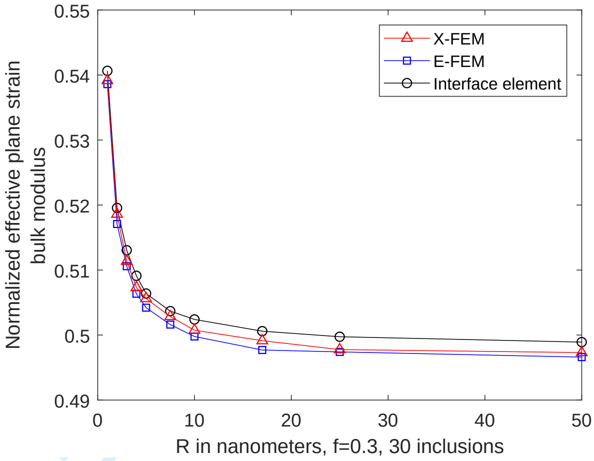

(b) Size effect

Fig. 12: Size effect for effective plane-strain bulk modulus with randomly distributed nano-inclusions ($f = 0.3$, $E_m = 70$ GPa, $E_i = 0.1E_m$, $\nu_m = \nu_i = 0.32$; $\lambda_s = 6.842$ N/m, $\mu_s = -0.375$ N/m, corresponding to $k_s = 6.092$ N/m).

To get closer to realistic micro-structures, different RVEs consisting of randomly distributed nano-inclusions are analyzed. We investigate here a domain with 30 monodisperse inclusions (see Fig. 11). The radius of the inclusions is chosen in a range from 1 nm to 50 nm while their volume fraction is fixed to $f = 0.3$. For each size of inclusion, we generate a random microstructure and calculate the homogenized bulk modulus until we reach the statistical convergence of the average value of the effective bulk modulus (see Fig.12a). The results obtained from the proposed approach are compared with those of X-FEM and the Interface element approach [36]. The expected size effect is observed for the three approaches in Fig. 12b.

	X-FEM	E-FEM	Interface element
Number of standard d.o.f	20000	20000	21528
Number of additional d.o.f	4560	4560	0
Total unknowns	24560	24560	21528
Number of integration points each enriched element	9 (2 on Γ)	2 (1 on Γ)	$\emptyset$
Size of elemental stiffness matrix	12×12	6×6	6×6
Final size of global stiffness matrix	$4.10^4 \times 4.10^4$	$2.10^4 \times 2.10^4$	21528×21528
Relative computing time for 1 realization	2.36	1.02	1

Table 1: Comparison of computational cost (X-FEM vs E-FEM vs Interface Element).

The computational costs of the different approaches are compared in Table 1. Note that the calculation time presented in this work has to be compared only qualitatively and has a relative meaning since no code optimization process has been done. We notice that X-FEM and E-FEM have the same number of additional degrees of freedom over the whole domain. However, due to the nodal enrichment strategy, the elemental and global stiffness matrices of X-FEM have double size compared to standard FEM. Moreover, the X-FEM enrichment makes the interpolations of the fields in the enriched element one order higher than for standard FEM. Therefore, it requires more integration points in the bulk and on the interface of the enriched element. On the contrary, the local enhancement of E-FEM allows condensing the additional degrees of freedom at the element level leading to a size of the final global system identical to that of standard FEM. The required memory space and the computational time of E-FEM and Interface element approaches are almost identical. For the approaches performed on the regular mesh which do not require any discretization effort, the results given by E-FEM and X-FEM are very close but the proposed approach is less costly than X-FEM.

5.4 Nonlinear behavior

After being validated and exploited for linear behaviors, the developed numerical approach is employed here to deal with non-linear material behavior. In the very first example here, we consider the interface as a linear elastic material. For the bulk, a von Mises type elastoplastic law with linear isotropic hardening is considered :

$$f_{(\boldsymbol{\sigma},q)} = \| \operatorname{dev}(\boldsymbol{\sigma}) \| - \sqrt{\frac{2}{3}}(\sigma_y - q) \ , \qquad (68)$$

where σ_y is the elastic limit stress and q is the stress-like variable associated to hardening. Since we deal with a non-linear problem, a standard Newton-Raphson procedure and a return mapping integration [46, 47, 55] of elastoplasticity model have been used.

After linearization, the local equilibrium equations are rewritten under an incremental form. The linearization form of the local one (Eq. (59b)) is given as:

$$Lin\left[\mathbf{h}_e\left(\mathbf{u}^{(i)}_{n+1}, \mathbf{a}^{(i),(k)}_{n+1}\right)\right] = -\mathbf{h}_e\left(\mathbf{u}^{(i)}_{n+1}, \mathbf{a}^{(i),(k)}_{n+1}\right) + \left([\mathbf{K}^e_{aa}]^{(i),(k)}_{n+1}\right) \Delta\mathbf{a}^{(i),(k)}_{n+1} = 0 \ , \qquad (69)$$

where i, k are the global and local iteration, respectively and n denotes global load step.

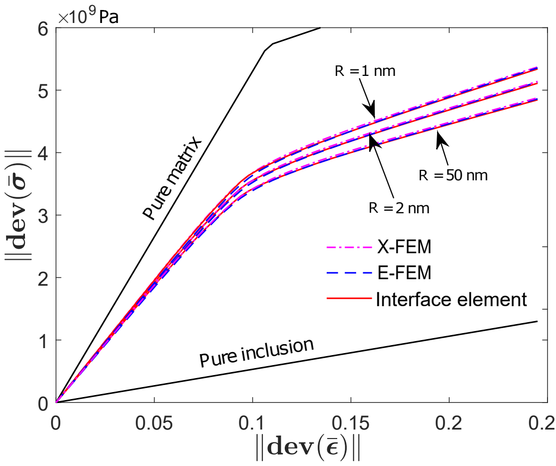

Fig. 13: Homogenized elastoplastic behavior for three different radii of nano-inclusion using X-FEM, E-FEM and Interface element approach for a tensile test with prescribed macroscopic strain $\epsilon^M_{11} = 0.3, \epsilon^M_{22} = \epsilon^M_{33} = \epsilon^M_{12} = 0$.

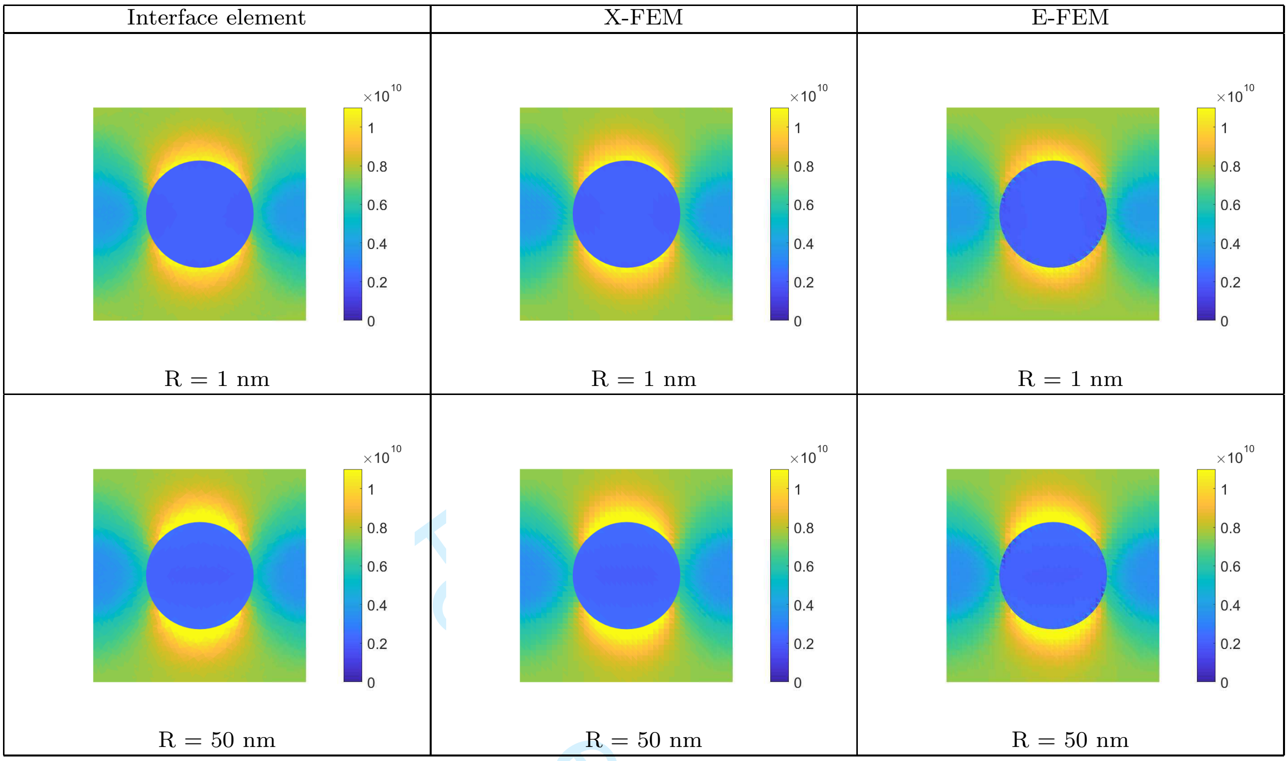

Fig. 14: Comparison of the norm of deviatoric stress tensor $\parallel \mathrm{dev}(\boldsymbol{\sigma}) \parallel$ (Pa) obtained from the three numerical approaches at the end of the test for R = 1 nm and R = 50 nm.

After we found the value of **a** that verifies the local equilibrium, the static condensation given in Eq. (63) is performed. Note that all stiffness matrices $\mathbf{K}^e_{uu}$, $\mathbf{K}^e_{ua}$, $\mathbf{K}^e_{au}$, $\mathbf{K}^e_{aa}$ in Eq. (60) are now computed with the coherent tangent stiffness $\mathbf{C}^{ep}$ (see [46,47]) for the bulk. The linearization for the global equilibrium equation for the computation of $\varDelta\mathbf{u}^{(i)}_{n+1}$ ends up with the form :

$$\mathop{\mathrm{A}}\limits_{e=1}^{Nelem} \left(\mathbf{f}^{e,int,(i)}_{n+1} - \mathbf{f}^{ext}_{n+1}\right) + \mathop{\mathrm{A}}\limits_{e=1}^{Nelem} \widetilde{\mathbf{K}}^{e,(i)}_{n+1} \varDelta\mathbf{u}^{(i)}_{n+1} = \mathbf{0}\ , \quad (70)$$

where $\widetilde{\mathbf{K}}^{e,(i)}_{n+1}$ is obtained using Eq. (63) and

$$\mathbf{f}^{e,int,(i)}_{n+1} = \int\limits_{\varOmega_e \backslash \varGamma_e} \mathbf{B}^T \boldsymbol{\sigma}^{(i)}_{n+1} d\varOmega + \int\limits_{\varGamma_e} \mathbf{B}^T \mathcal{M}^T \boldsymbol{\sigma}^{(i)}_{s,n+1} d\varGamma\ . \quad (71)$$

The number of internal variables to be updated on each enhanced element depends on the number of integration points we use on these elements. In our work, we used 2 integration points per enhanced element (see Fig. 3) resulting in 10 internal variables per element.

A simple traction test is performed on the RVE presented in Fig. 8 with the same material properties as in the previous subsection ($E_m = 70$ GPa, $E_i = 0.1E_m$, $\nu_m = \nu_i = 0.32$; $\lambda_s = 6.842$ N/m, $\mu_s = -0.375$ N/m). The elastic limit stress and hardening modulus of the bulk are set to be equal for both matrix and inclusion : $\sigma_y = 7$ GPa, $K = 20$ GPa. In order to observe the size effect, we chose three different radii for the inclusion R = 1nm, 2nm, and 50 nm. Fig. 13 shows the homogeneous behavior with regard to the mean deviatoric stress with respect to the mean deviatoric strain. The results obtained from the proposed approach are compared to those from the X-FEM and Interface element approach presented in our previous work [36]. The significant influence of the interface is shown not only in terms of effective elastic limit but also in terms of effective behavior both in the elastic and plastic parts of the material. In addition, an excellent agreement between the three numerical approaches is obtained whereas the amount of local nonlinear updating is not the same order for each method. Figures 14 and 15 present, respectively, the distribution of the norm of the deviatoric stress and the cumulative plastic strain field, at the end of the test, for the case R = 1 nm and R = 50 nm considering three different numerical approaches. As can be seen, the results in terms of the stress and strain fields are very similar for the three approaches. We notice that the radius of the inclusion affects the stress distribution around the inclusion (see Fig. 14) and therefore the plasticity evolution (see Fig. 15).

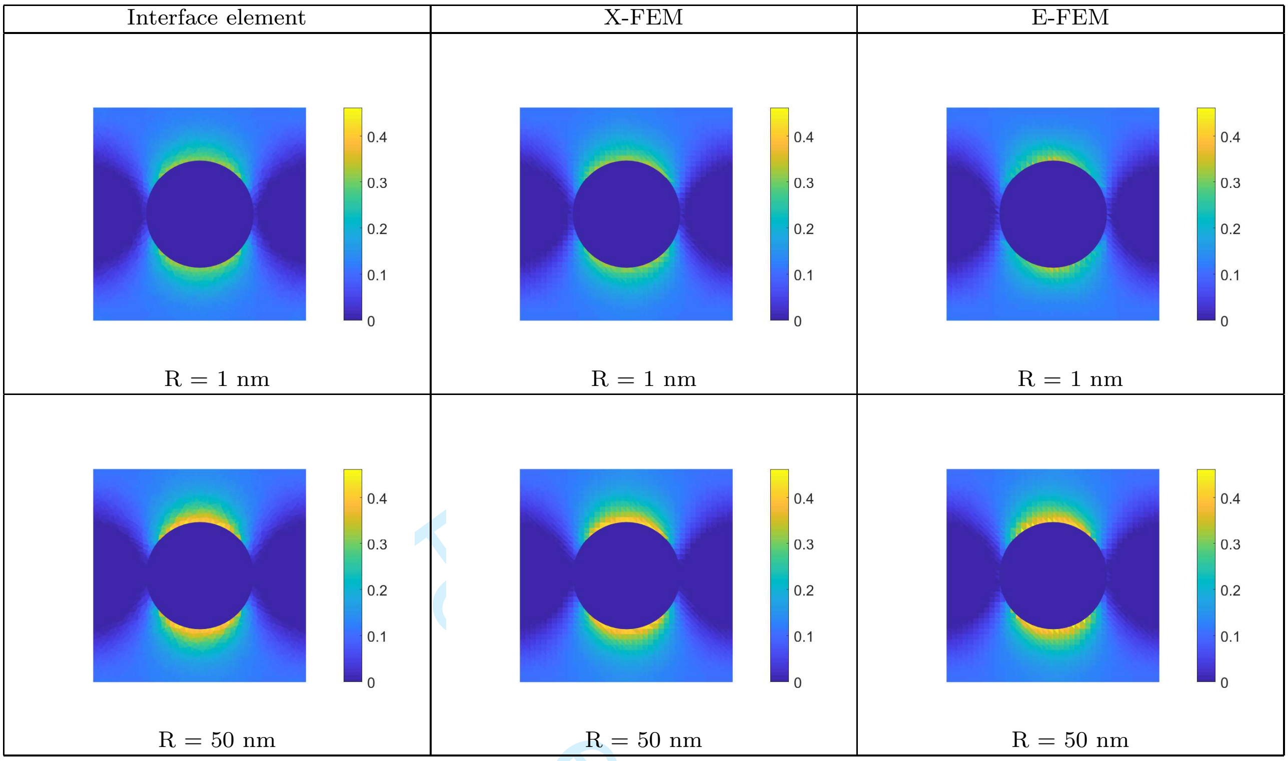

Fig. 15: Comparison of the cumulative plastic deformation obtained from the three numerical approaches at the end of the test for R = 1 nm and R = 50 nm.

At this stage, we can proceed with a comparison in terms of computational cost in handling the nonlinear behavior of the three considered approaches. For the case of circular nano-inclusion presented above, the comparison is presented in Table 2. The enriched FEM approaches (X-FEM, E-FEM) require more than one integration point on the enriched elements resulting in larger computational costs. Compared to X-FEM, E-FEM requires fewer integration points on each enriched elements (E-FEM : 2 points, X-FEM : 9 points). Moreover, the additional d.o.f for E-FEM can technically be considered as internal variables of the enriched element since they are determined and condensed at the local level by the use of the operator split technique. Therefore, among the two enriched FEM approaches, E-FEM is cheaper than X-FEM in terms of computational cost.

With the enriched E-FEM approaches, the test can be performed on more complex geometries of the RVE such as inclusions with non-convex shapes as presented in Fig. 10. For a fixed volume fraction $f = 0.2$, the shape dependence on nonlinear behavior is presented in Fig. 16. The same conclusion as this reported in subsection 5.2 is observed. For a fixed volume fraction, we notice a decrease of the rigidity according to the increase of the number of oscillations in both elastic and plastic phases.

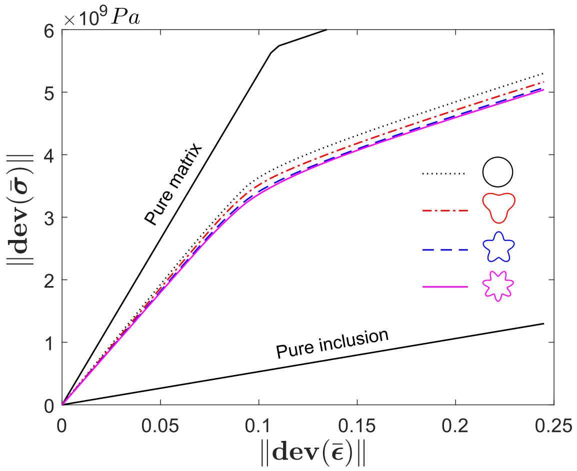

Fig. 16: Homogenized elastoplastic behavior for different shapes of inclusion.

6 Conclusion

In this work, we have proposed a numerical approach based on the Embedded Finite Element Method for predicting the mechanical behavior of nanocomposite by taking into account the size effect. A coherent interface model with a surface elasticity has been added in

	X-FEM	E-FEM	Interface element
Number of standard d.o.f	242	242	338
Number of enriched elements	34	34	0
Number of additional d.o.f	68	68	0
Total unknowns at the global level	310	242	338
Number of integration points for each enriched element	9	2	∅
Number of internal variables for each enriched element	45	10	∅
Final size of global stiffness matrix	484 × 484	242 × 242	338 ×338
Relative computing time	4.80	2.65	1

Table 2: Comparison of computational cost in the case of an elastoplastic behavior (X-FEM vs E-FEM vs Interface element).

the framework of a three-field variational formulation, leading to the introduction of interface terms in both, global and local, equilibrium equations. Instead of the traction continuity condition, the generalized Young-Laplace equation has been introduced at the element level by choosing an appropriate interpolation of the virtual enhanced surface strain. Due to the use of the “operator split method” and “static condensation” at the element level, the global size of the problem does not depend on the number of inclusions and interfaces.

The choice of using the SKON formulation has been made after a performance evaluation of the three formulations of E-FEM in the classical homogenization problems. In addition, the comparison of three numerical methods (X-FEM, E-FEM, and Interface element) in terms of convergence has been performed with and without surface elasticity. The validation of the new approach based on E-FEM has been done by comparison to analytical solutions and to the results provided by X-FEM and Interface Element approaches. The effective moduli predicted by the proposed strategy are very comparable to the one provided by X-FEM or Interface element based approach, a size effect is revealed either for periodic or random microstructures.

In order to assess the influence of the nonlinear behavior of the bulk, a nanocomposite unit cell composed of an elastoplastic bulk with linear isotropic hardening law and an elastic coherent interface has been studied. The results obtained from the proposed approach based on E-FEM showed a very good agreement to those of the X-FEM and the Interface element approach. Moreover, the notable influence of the interface is clearly shown. The size effect is observed both in the elastic part and in the plastic part as well as on the apparent elastic limit of the nanocomposite. These results make it possible to consider more complex and realistic behaviors than those usually considered, in particular nonlinear behaviors with internal variables for the various components. For future works, nonlinear behaviors of the interface could also be investigated.

The comparisons between the three numerical methods (X-FEM, E-FEM, and Interface element) in terms of computational cost have been presented for both linear and nonlinear cases. Due to the use of fewer integration points in the enriched elements and condensation of additional d.o.f, E-FEM appears to be less expensive than X-FEM, while allowing to describe the microstrucutre with non-conforming meshes.

In future works, extension of the proposed approach to 3D problems could be investigated along with a coupling to more complex behaviors of the imperfect interface.

Conflict of interest

The authors declare that they have no conflict of interest.

References

1. Jérôme Douce, Jean-Pierre Boilot, John Biteau, Laurence Scodellaro, and Armel Jimenez. Effect of filler size and surface condition of nano-sized silica particles in polysiloxane coatings. *Thin Solid Films*, 466(1-2):114–122, 2004.
2. S Mishra, SH Sonawane, and RP Singh. Studies on characterization of nano caco3 prepared by the in situ deposition technique and its application in pp-nano caco3

composites. *Journal of Polymer Science Part B: Polymer Physics*, 43(1):107–113, 2005.

3. J Cho, MS Joshi, and CT Sun. Effect of inclusion size on mechanical properties of polymeric composites with micro and nano particles. *Composites Science and Technology*, 66(13):1941–1952, 2006.
4. AS Blivi, F Benhui, J Bai, D Kondo, and F Bédoui. Experimental evidence of size effect in nano-reinforced polymers: Case of silica reinforced pmma. *Polymer Testing*, 56:337–343, 2016.
5. Adoteé Sitou Blivi. *Effet de taille dans les polymères nano-renforcés: caractérisation multi-échelles et modélisation*. PhD thesis, 2018.
6. Ronald E Miller and Vijay B Shenoy. Size-dependent elastic properties of nanosized structural elements. *Nanotechnology*, 11(3):139, 2000.
7. HL Duan, Jian-xiang Wang, ZP Huang, and Bhushan Lal Karihaloo. Size-dependent effective elastic constants of solids containing nano-inhomogeneities with interface stress. *Journal of the Mechanics and Physics of Solids*, 53(7):1574–1596, 2005.
8. Vijay B. Shenoy. Atomistic calculations of elastic properties of metallic fcc crystal surfaces. *Phys. Rev. B*, 71:094104, Mar 2005.
9. Changwen Mi, Sukky Jun, Demitris A. Kouris, and Sung Youb Kim. Atomistic calculations of interface elastic properties in noncoherent metallic bilayers. *Phys. Rev. B*, 77:075425, Feb 2008.
10. D Brown, P Mele, S Marceau, and ND Alberola. A molecular dynamics study of a model nanoparticle embedded in a polymer matrix. *Macromolecules*, 36(4):1395–1406, 2003.
11. D. Brown, V. Marcadon, P. Mélé, and N. D. Albérola. Effect of filler particle size on the properties of model nanocomposites. *Macromolecules*, 41(4):1499 – 1511, 2008.
12. V Marcadon, D Brown, Eveline Hervé, P Mélé, ND Albérola, and André Zaoui. Confrontation between molecular dynamics and micromechanical approaches to investigate particle size effects on the mechanical behaviour of polymer nanocomposites. *Computational Materials Science*, 79:495–505, 2013.
13. Bhasker Paliwal, Mohammed Cherkaoui, and Omar Fassi-Fehri. Effective elastic properties of nanocomposites using a novel atomistic–continuum interphase model. *Comptes Rendus Mecanique*, 340(4-5):296–306, 2012.
14. Thinh-Tien Le, Johann Guilleminot, and Christian Soize. Stochastic continuum modeling of random interphases from atomistic simulations. application to a polymer nanocomposite. *Computer Methods in Applied Mechanics and Engineering*, 303:430–449, 2016.
15. P Sharma, S Ganti, and N Bhate. Effect of surfaces on the size-dependent elastic state of nano-inhomogeneities. *Applied Physics Letters*, 82(4):535–537, 2003.
16. P Sharma and S Ganti. Size-dependent eshelby's tensor for embedded nano-inclusions incorporating surface/interface energies. *Transactions-American society of mechanical engineers journal of applied mechanics*, 71(5):663–671, 2004.
17. P Sharma and S Ganti. Erratum: "Size-Dependent Eshelby's Tensor for Embedded Nano-Inclusions Incorporating Surface/Interface Energies" [Journal of Applied Mechanics, 2004, 71 (5), pp. 663–671]. *Journal of Applied Mechanics*, 72(4):628–628, 2005.
18. P Sharma, S Ganti, and N Bhate. Erratum: "effect of surfaces on the size-dependent elastic state of nano-inhomogeneities" [appl. phys. lett. 82, 535 (2003)]. *Applied Physics Letters*, 89(4):535, 2006.
19. Tungyang Chen, George J Dvorak, and CC Yu. Size-dependent elastic properties of unidirectional nano-composites with interface stresses. *Acta Mechanica*, 188(1-2):39–54, 2007.
20. H. Le Quang and Q. C. He. Estimation of the effective thermoelastic moduli of fibrous nanocomposites with cylindrically anisotropic phases. *Archive of Applied Mechanics*, 79(3):225–248, Mar 2009.
21. Sébastien Brisard, Luc Dormieux, and D Kondo. Hashin–shtrikman bounds on the bulk modulus of a nanocomposite with spherical inclusions and interface effects. *Computational Materials Science*, 48(3):589–596, 2010.
22. Sébastien Brisard, Luc Dormieux, and Djimedo Kondo. Hashin–shtrikman bounds on the shear modulus of a nanocomposite with spherical inclusions and interface effects. *Computational Materials Science*, 50(2):403–410, 2010.
23. Y Benveniste. Models of thin interphases and the effective medium approximation in composite media with curvilinearly anisotropic coated inclusions. *International Journal of Engineering Science*, 72:140–154, 2013.
24. V Marcadon, E Herve, and A Zaoui. Micromechanical modeling of packing and size effects in particulate composites. *International Journal of Solids and Structures*, 44(25-26):8213–8228, 2007.
25. WX Zhang and TJ Wang. Effect of surface energy on the yield strength of nanoporous materials. *Applied Physics Letters*, 90(6):063104, 2007.
26. Luc Dormieux and Djimedo Kondo. An extension of gurson model incorporating interface stresses effects. *International Journal of Engineering Science*, 48(6):575–581, 2010.
27. Luc Dormieux and Djimedo Kondo. Non linear homogenization approach of strength of nanoporous materials with interface effects. *International Journal of Engineering Science*, 71:102–110, 2013.
28. Antoine Lucchetta, Stella Brach, and Djimédo Kondo. Effects of particles size on the overall strength of nanocomposites: Molecular dynamics simulations and theoretical modeling. *Mechanics Research Communications*, page 103669, 2021.
29. Gao Wei, YU Shouwen, and Huang Ganyun. Finite element characterization of the size-dependent mechanical behaviour in nanosystems. *Nanotechnology*, 17(4):1118, 2006.
30. Ali Javili, George Chatzigeorgiou, Andrew T McBride, Paul Steinmann, and Christian Linder. Computational homogenization of nano-materials accounting for size effects via surface elasticity. *GAMM-Mitteilungen*, 38(2):285–312, 2015.
31. Ali Javili, Paul Steinmann, and Jörn Mosler. Micro-to-macro transition accounting for general imperfect interfaces. *Computer Methods in Applied Mechanics and Engineering*, 317(Supplement C):274 – 317, 2017.
32. Julien Yvonnet, H Le Quang, and Q-C He. An xfem/level set approach to modelling surface/interface effects and to computing the size-dependent effective properties of nanocomposites. *Computational Mechanics*, 42(1):119–131, 2008.
33. Mehdi Farsad, Franck J Vernerey, and Harold S Park. An extended finite element/level set method to study surface effects on the mechanical behavior and properties of nanomaterials. *International Journal for Numerical Methods in Engineering*, 84(12):1466–1489, 2010.
34. Q-Z Zhu, S-T Gu, Julien Yvonnet, J-F Shao, and Q-C He. Three-dimensional numerical modelling by xfem

of spring-layer imperfect curved interfaces with applications to linearly elastic composite materials. *International Journal for Numerical Methods in Engineering*, 88(4):307–328, 2011.
35. Brahim Elkhalil Hachi, Abdelfattah Elhadj Benkhechiba, Mohammed Riad Kired, Dahmane Hachi, and Mohamed Haboussi. Some investigations on 3d homogenization of nano-composite/nano-porous materials with surface effect by fem/xfem methods combined with level-set technique. *Computer Methods in Applied Mechanics and Engineering*, 371:113319, 2020.
36. Dang Phong Bach, Delphine Brancherie, and Ludovic Cauvin. Size effect in nanocomposites: Xfem/level set approach and interface element approach. *Finite Elements in Analysis and Design*, 165:41 – 51, 2019.
37. D Brancherie and Adnan Ibrahimbegovic. Novel anisotropic continuum-discrete damage model capable of representing localized failure of massive structures: Part i: theoretical formulation and numerical implementation. *Engineering Computations*, 26(1/2):100–127, 2009.
38. A Ibrahimbegovic and D Brancherie. Combined hardening and softening constitutive model of plasticity: precursor to shear slip line failure. *Computational Mechanics*, 31(1-2):88–100, 2003.
39. Emmanuel Roubin, Alexis Vallade, Nathan Benkemoun, and Jean-Baptiste Colliat. Multi-scale failure of heterogeneous materials: A double kinematics enhancement for embedded finite element method. *International Journal of Solids and Structures*, 52:180–196, 2015.
40. Nathan Benkemoun, Martin Hautefeuille, J-B Colliat, and Adnan Ibrahimbegovic. Failure of heterogeneous materials: 3d meso-scale fe models with embedded discontinuities. *International Journal for Numerical Methods in Engineering*, 82(13):1671–1688, 2010.
41. Milan Jirásek. Comparative study on finite elements with embedded discontinuities. *Computer methods in applied mechanics and engineering*, 188(1-3):307–330, 2000.
42. Fabien Cazes, Guenther Meschke, and Meng-Meng Zhou. Strong discontinuity approaches: An algorithm for robust performance and comparative assessment of accuracy. *International Journal of Solids and Structures*, 96:355–379, 2016.
43. Morton E. Gurtin and A. Ian Murdoch. A continuum theory of elastic material surfaces. *Archive for Rational Mechanics and Analysis*, 57(4):291–323, Dec 1975.
44. Yu Z Povstenko. Theoretical investigation of phenomena caused by heterogeneous surface tension in solids. *Journal of the Mechanics and Physics of Solids*, 41(9):1499–1514, 1993.
45. ME Gurtin, J Weissmüller, and F Larche. A general theory of curved deformable interfaces in solids at equilibrium. *Philosophical Magazine A*, 78(5):1093–1109, 1998.
46. Juan C Simo and Thomas JR Hughes. *Computational inelasticity*, volume 7. Springer Science & Business Media, 2006.
47. Adnan Ibrahimbegovic. *Nonlinear solid mechanics: theoretical formulations and finite element solution methods*, volume 160. Springer Science & Business Media, 2009.
48. Juan C Simo and MS Rifai. A class of mixed assumed strain methods and the method of incompatible modes. *International journal for numerical methods in engineering*, 29(8):1595–1638, 1990.
49. Edward L Wilson and Adnan Ibrahimbegovic. Use of incompatible displacement modes for the calculation of element stiffnesses or stresses. *Finite Elements in Analysis and Design*, 7(3):229–241, 1990.
50. Adnan Ibrahimbegovic and EL Wilson. A modified method of incompatible modes. *Communications in Applied Numerical Methods*, 7(3):187–194, 1991.
51. Jack Chessa and Ted Belytschko. An enriched finite element method and level sets for axisymmetric two-phase flow with surface tension. *International Journal for Numerical Methods in Engineering*, 58(13):2041–2064, 2003.
52. Edward L Wilson. The static condensation algorithm. *International Journal for Numerical Methods in Engineering*, 8(1):198–203, 1974.
53. Natarajan Sukumar, David L Chopp, Nicolas Moës, and Ted Belytschko. Modeling holes and inclusions by level sets in the extended finite-element method. *Computer methods in applied mechanics and engineering*, 190(46-47):6183–6200, 2001.
54. Tung Doan, Hung Le-Quang, and Quy-Dong To. effective elastic stiffness of 2d materials containing nanovoids of arbitrary shape. *International Journal of Engineering Science*, 150:103234, 2020 .
55. Peter Wriggers. *Nonlinear finite element methods*. Springer Science & Business Media, 2008.

Answer to the reviewers on revised version of paper Computational Mechanics

An Embedded-FEM approach accounting for the size effect in nanocomposites

First of all, we would like to thank the reviewers for their constructive comments, which for sure help us improve our paper. Please note that all the changes in the revised version are marked in red.

Reviewer # 1

1. *The curvature tensor is introduced in Equation 6 but specified not before Equation 50 (moreover, Equation 50 restricts the curvature tensor to the 2D case; see comments below). The paper may benefit form providing some information on (the general format of) the curvature tensor when it is introduced (for example directly after Equation 6).*

The general format and a brief introduction of the curvature tensor has been added after equation (6) (see equations (7) and (8)).

2. *The contribution delta-Gamma in Equation 13 and 16 could be specified. ("activation" of the surface contribution on Gamma, I think; cf. Equation 14 and 15, where "on Gamma" is explicitly mentioned so that delta-Gamma = 1 on Gamma and 0 otherwise, correct?)*

It's true that $\delta_\Gamma = 1$ on Γ and 0 otherwise. The definition of δ_Γ has been added after Equation (17) (previously numbered equation (13)) to clarify. Thank you for your suggestion.

3. *Equation 50 specifies the curvature tensor for the 2D case. It should be mentioned (in text or, for example, in a Remark) how this extends to the 3D case.*

The extension to 3D case of the definition of the curvature tensor has been added.

4. *The paragraph after Equation 53 briefly discusses the general computation of the curvature (reference 49 is restricted to the axisymmetric case). The paper would benefit from further specifying this (is the mean curvature based on the divergence of the normalized gradient of phi sufficient? how to deal with "noisy" distributions of phi?). I consider this information to be important, since all examples included in the paper directly prescribe the radius of curvature so that it is not addressed, respectively clear, how the framework can be applied to more general, i.e. non-perfect, real microstructures based on, e.g., experimentally determined micrographs.*

We have to admit that we did not have the opportunity to test the strategy on real non-perfect microstructures based on micrographs. The proposed approach requires prior processing (filtering) of images derived from micrographs of real microstructures. It is clear that the image segmentation phase, the choice of the segmentation parameters, and the choice of discretization may affect the effectiveness of the proposed strategy and must be carried out carefully.

5. *The formulation is based on a small strain setting. The examples, for example in Section 4, consider strains of 50 percent - is this realistic, respectively needed (could be scaled anyways - maybe a typo).*

It's truly a typo, the considered strain is 0.5 percent (not 50 percent). Thank you for noticing and pointing it out, we have corrected it in the revised version.

***6.** The paper is well written. However, few wordings could be checked such as "Injecting" (Inserting?) in the first sentence of Section 3.2 and "submitted" (subjected?) in paragraph after Figure 4, to name but two.*

The whole text has been carefully checked and typos corrected.

Reviewer # 2

***7.** Section 2 : Governing equations The content of this section is clear; some points dealing with surface elasticity suitably complete the presentation already done in the reference 36 of the authors in which a XFEM/level-set approach for nanocomposites has been proposed. The constitutive equations described in subsection 2.2 are restricted to linear elastic behavior while the non linear behavior is not mentioned. Please, correct.*

The constitutive equations for the non linear behavior have been added in subsection 2.2.

***8.** Section 3 : Finite Element interpolation. Strain field interpolation is first presented. It is important to clearly indicate here what is the novelty, since the displacement field is continuous? Is it the account of the strain field discontinuity or of the surface strain associated to the interface?. The authors must clearly indicated the original point(s) of the present section.*

The novelty is the extension of the E-FEM approach to take into account imperfect interfaces with surface elasticity. More precisely, the main contribution is the enhancement of the interpolation of the interface/surface strain. We have added a comment on this point at the beginning of section 3. We thank you for the precious comment.

***9.** Section 4 : The authors aim at assessing the performance of the SKON-based approach of E-FEM with respect to that obtained with SOS and KOS based computations, such comparison being already done by other authors (cited in the paper) for problems with strong discontinuities. My main criticism here is that such evaluation is made only in the case of linear elastic Eshelby problem with perfect interface. What is the guarantee that the SKON formulation will show the best performance in the context of nano composites (for wh imperfect interface) and more critically in the case of a nano composite with an elastoplastic matrix? If possible, the authors must provide at this stage a numerical complement on these points and/or present strong and convincing arguments which may support the numerical results that will be presented in section 5.*

As SKON formulation shows better results for the limit case of a perfect interface (corresponding to an imperfect elastic interface with null elasticity parameters), we have chosen to continue our developments with this approach so as to have a general formulation valid in the general case. This is, moreover, consistent with the observations made in the case of cohesive interfaces (or strong discontinuities) where the SKON method remains the formulation of choice.

***10.** Section 5 : Numerical results This section is devoted to a plane strain modeling of nanocomposites, with emphasis on inclusions size effects; i find it particularly interesting in view of results obtained from simulations with multiple inclusions or complex shape. All the numerical results presented in the paper are obtained for inclusions which are ten times softer than the matrix. What is the reason of such choice? Are the conclusions the same when the matrix is reinforced by stiffer nano inclusions? Moreover, I am wondering if some results in section 5.2 cannot be compared in the linear elastic cases to analytical bounds established by Le Quang and He (Variational principles and bounds for elastic inhomogeneous materials with coherent imperfect interfaces. Mechanics of Materials 40 (2008) 865–884). A recent and probably useful paper in the same vein, but on linear elastic nanoporous materials with voids having arbitrary shape is by Doan et al. (Effective elastic stiffness of 2D materials containing* *nanovoids of arbitrary shape. International Journal of Engineering Science 150 (2020) 103234). Concerning the effective bulk modulus shown on Figs 8 to 12, can the authors explain how it has been computed. Is there a proof of the isotropy of the effective properties? Subsection 5.4 constitutes a preliminary study dealing with a von Mises type elastoplastic matrix reinforced by cylindrical inclusions. The effective response is compared to results obtained in the previous work of the authors based on X-FEM computation. I suggest to the authors to complete these comparative results by showing strains and or stress map in the cell.*

The study of the contrast effect carried out in our previous work [1] showed that the size effect is affected by the stiffness contrast. The size effect is greater for nanoporous materials (contrast=0) and decreases as the contrast increases. The choice made here of a contrast of 0.1 is an intermediate choice. The results, in terms of comparison of the different approaches, remain valid for other levels of contrast.

The results in section 5.2 are compared to the analytical results obtained with the GSCM model presented in [2] (H. Le Quang and Q. C. He. Estimation of the effective thermoelastic moduli of fibrous nanocomposites with cylindrically anisotropic phases. Archive of Applied Mechanics, 79(3):225–248, Mar 2009). We chose GSCM because this model has the advantage of taking into account the interactions between the different phases (inclusions and matrix). This is not the case for Voigt and Reuss bounds, even if a size effect has been added in "(Le Quang and He (Variational principles and bounds for elastic inhomogeneous materials with coherent imperfect interfaces. Mechanics of Materials 40 (2008) 865–884)".

The paper of Doan et al. (Effective elastic stiffness of 2D materials containing nanovoids of arbitrary shape. International Journal of Engineering Science 150 (2020) 103234) is interesting and has been added to the references of this paper. Thank you for your contribution.

The effective bulk modulus is calculated through the total deformation energy (bulk energy + interface energy) and the assumption of isotropy of the effective properties. In order to show the ability of the numerical approach in dealing with more complex geometries, several cases with ellipse and non-convex arbitrary shapes of inclusions are considered in section 5.2. In these cases, for the purposes of the comparison, we have chosen to construct an effective "bulk modulus" on the basis of the isotropy assumption although that may not be the case for arbitrary microstructures. Note that this choice does not affect the conclusions on the observed size effects. These points have been clarified in subsection 5.2 of the revised paper.

Following your suggestion, the results and comments related to the stress and strain map in the cell (the norm of deviatoric stress tensor and the cumulative plastic deformation on the RVE) have been added to complete the comparison.

References

[1] Dang Phong Bach, Delphine Brancherie, and Ludovic Cauvin. Size effect in nanocomposites: Xfem/level set approach and interface element approach. *Finite Elements in Analysis and Design*, 165:41 – 51, 2019.

[2] H. Le Quang and Q. C. He. Estimation of the effective thermoelastic moduli of fibrous nanocomposites with cylindrically anisotropic phases. *Archive of Applied Mechanics*, 79(3):225–248, Mar 2009.

Dang Phong Bach
Laboratoire Roberval
Université de Technologie de Compiègne, France
Mail: dang-phong.bach@utc.fr

Editor
Computational Mechanics

July 20, 2021

Dear Editor,

We are pleased to submit the following paper to your journal:

An Embedded-FEM approach accounting for the size effect in nanocomposites

by Dang Phong Bach, Delphine Brancherie and Ludovic Cauvin.

We certify that the submission is an original work and is not under review for any other publication.

With the increasing interest in the development of nanocomposite materials, arises the necessity to make use of dedicated numerical approaches to better understand the behavior of such materials. A numerical approach based on the Embedded Finite Element Method (E-FEM) has been elaborated in order to model size effect in nanocomposites. For this purpose, the E-FEM standard Statically and Kinematically Optimal Nonsymmetric (SKON) formulation is enhanced to incorporate a surface elasticity at the interface between the matrix and the inclusions. The developed approach is shown to be an efficient tool for the evaluation and prediction of the mechanical behavior of nanocomposite materials.

Sincerely yours,
Dang Phong Bach, on the behalf of the authors

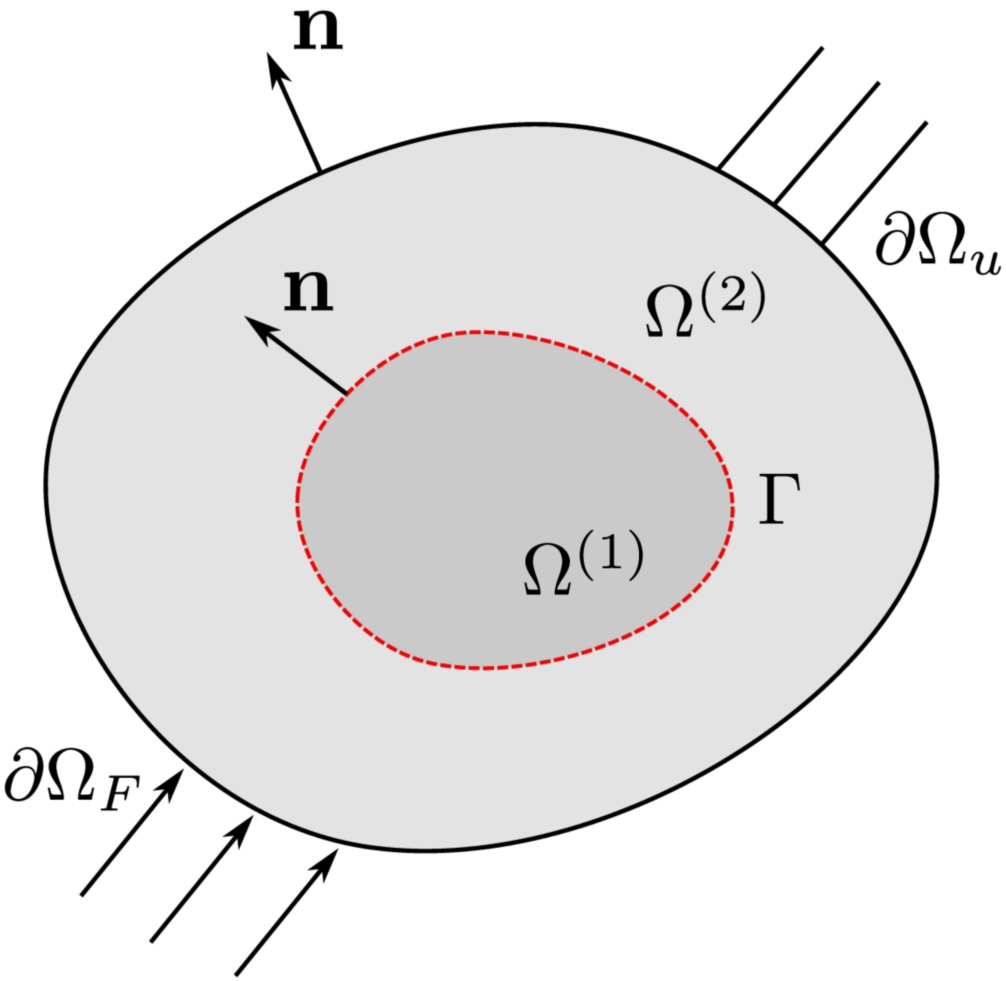

Problem definition: two phases material with imperfect interface.

176x174mm (600 x 600 DPI)

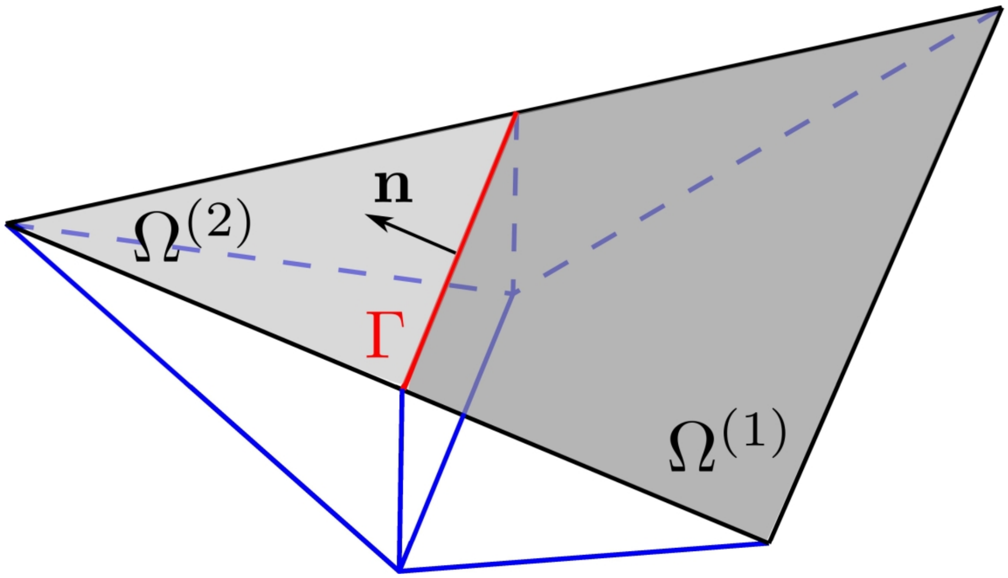

Shape function $ \bldM(\bldx) $ in an enhanced element

180x102mm (600 x 600 DPI)

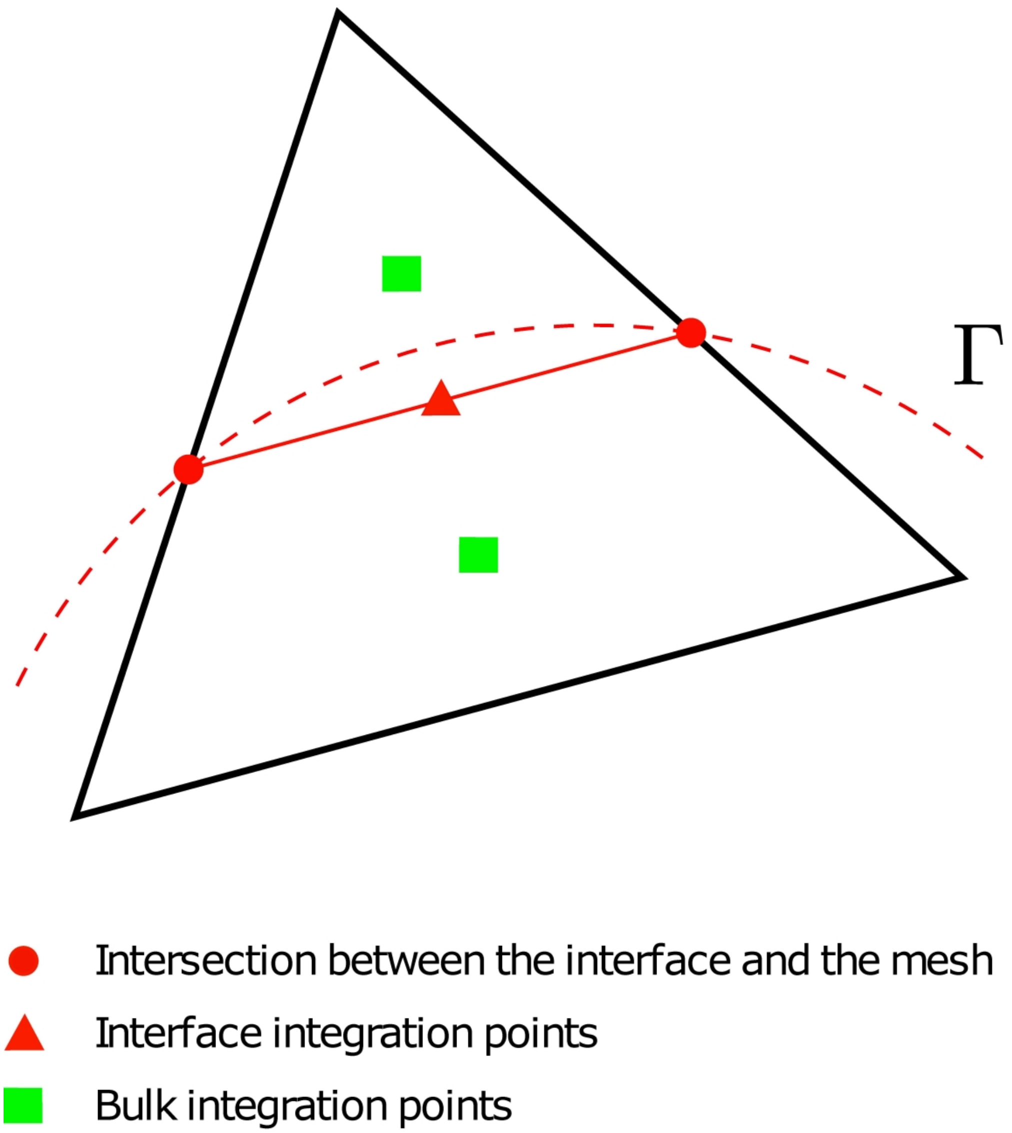

Element cut by the interface $ \Gamma $, approximated interface and integration points in E-FEM.

201x225mm (600 x 600 DPI)

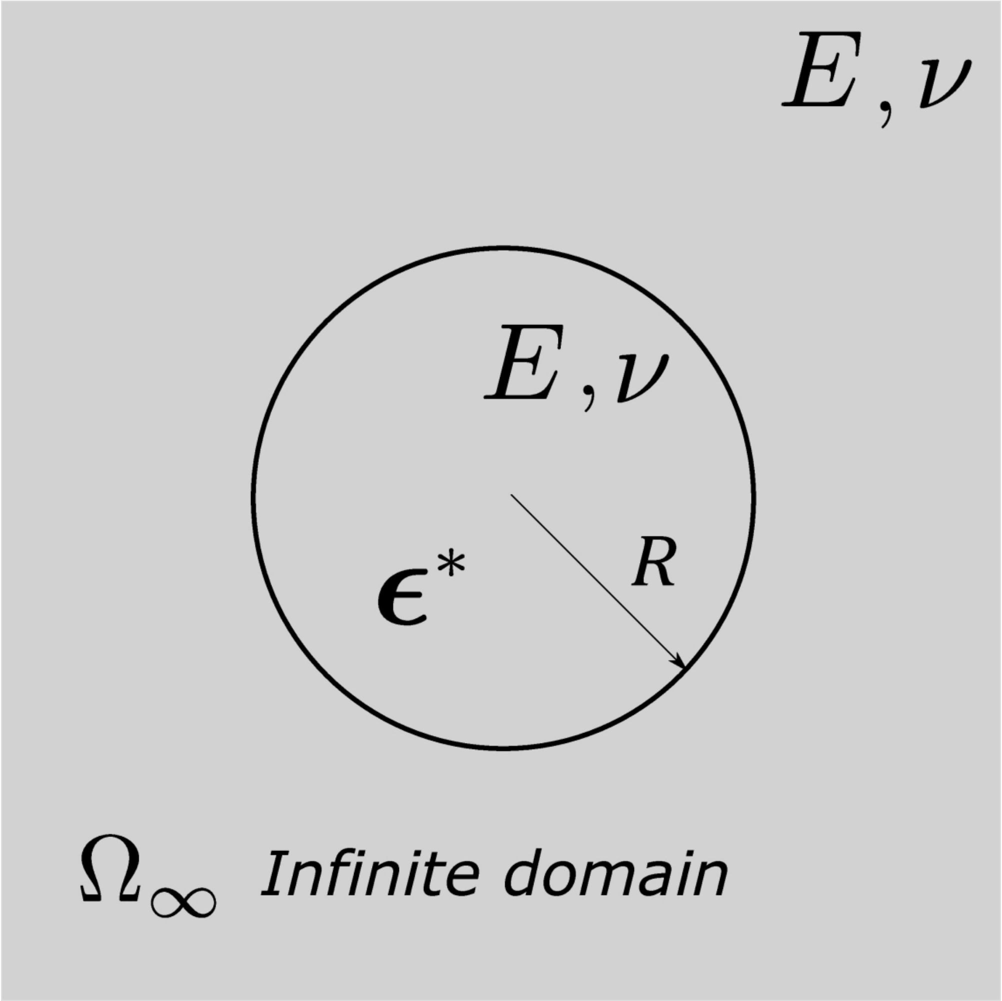

Classical first Eshelby problem and two-phase problem ($ R=1nm, f=0.2 $). (a) Eshelby problem

112x112mm (600 x 600 DPI)

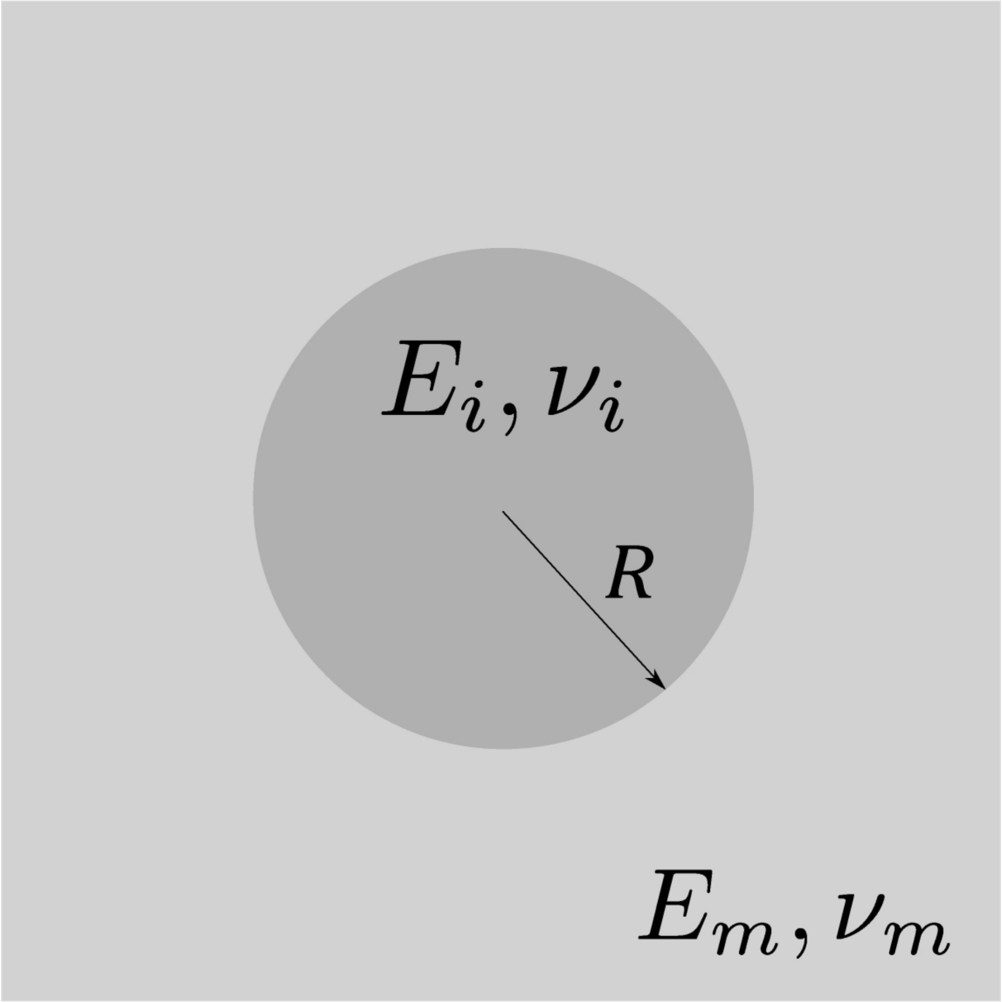

Classical first Eshelby problem and two-phase problem (\$ R=1nm, f=0.2 \$). (b) two-phase problem

105x105mm (600 x 600 DPI)

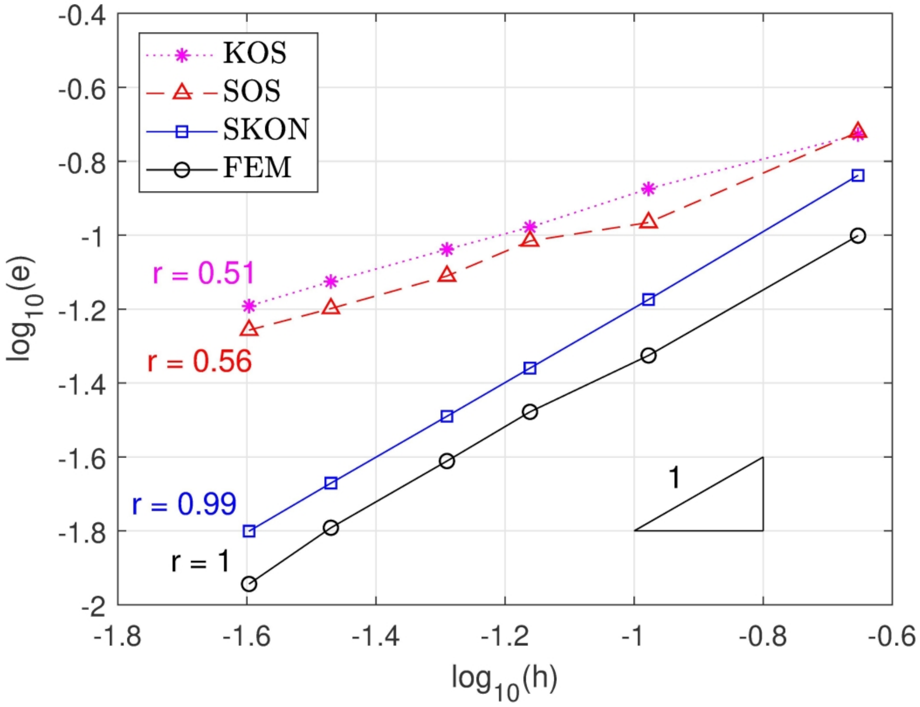

Convergence analysis of three formulations of E-FEM in treating the first Eshelby problem and the two-phase material problem. (a) Eshelby problem

148x111mm (600 x 600 DPI)

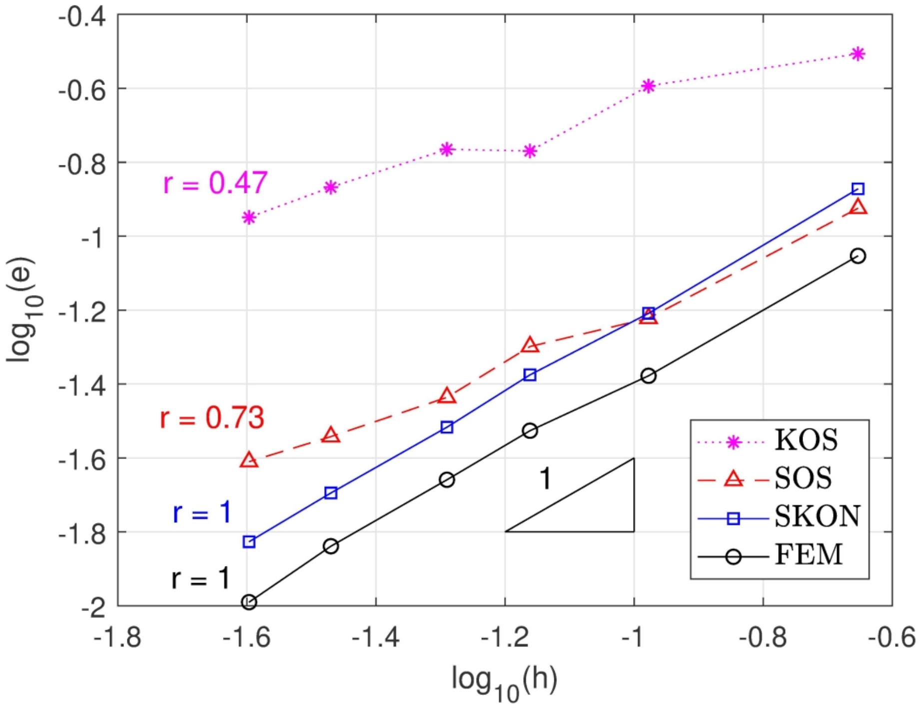

Convergence analysis of three formulations of E-FEM in treating the first Eshelby problem and the two-phase material problem. (b) Two-phase material

148x111mm (600 x 600 DPI)

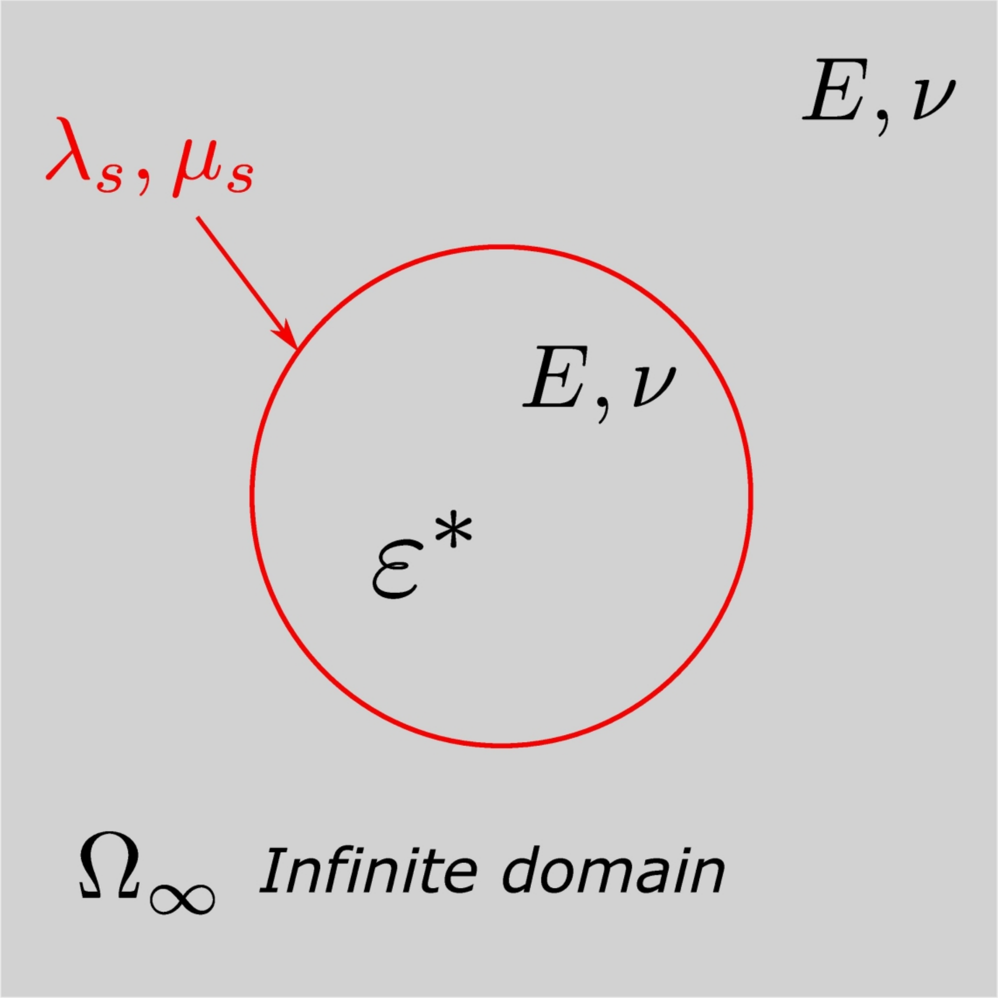

Surface elasticity is taken into account in the plane strain model. (a) Eshelby problem

113x113mm (600 x 600 DPI)

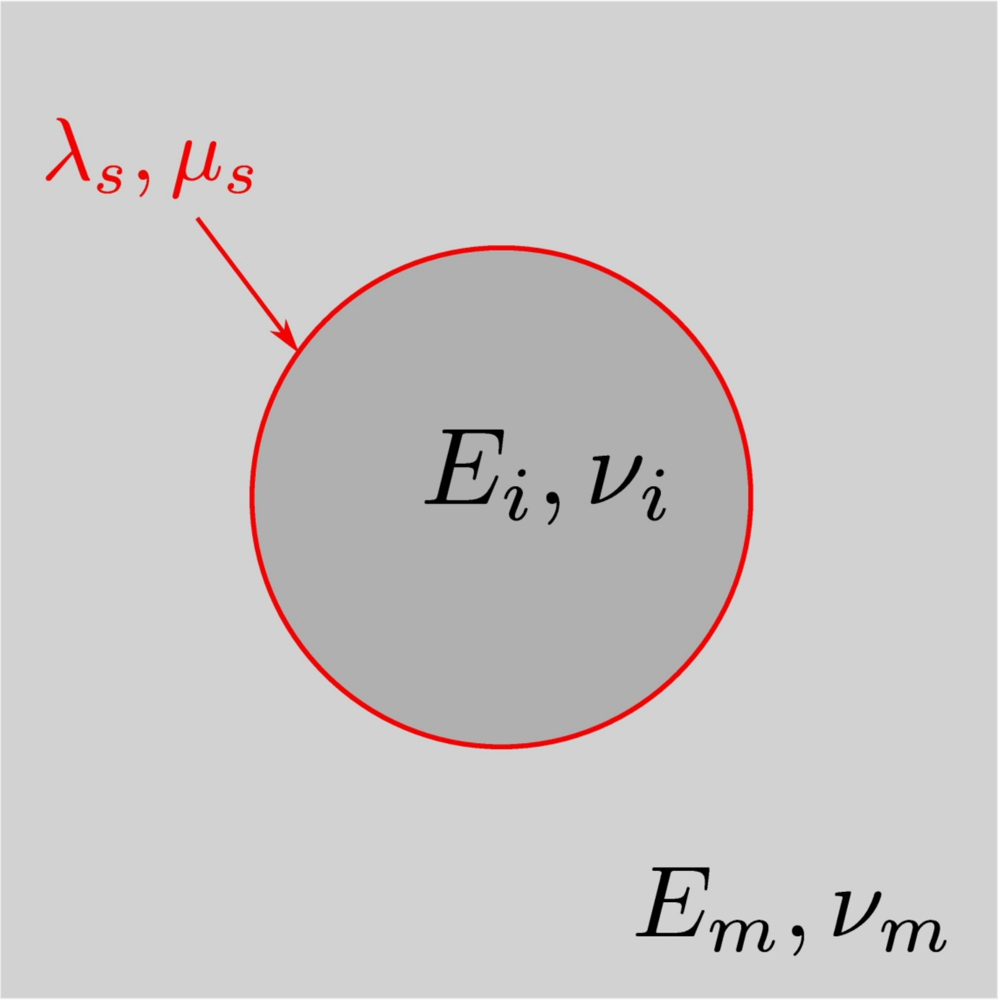

Surface elasticity is taken into account in the plane strain model. (b) Two phases material

113x113mm (600 x 600 DPI)

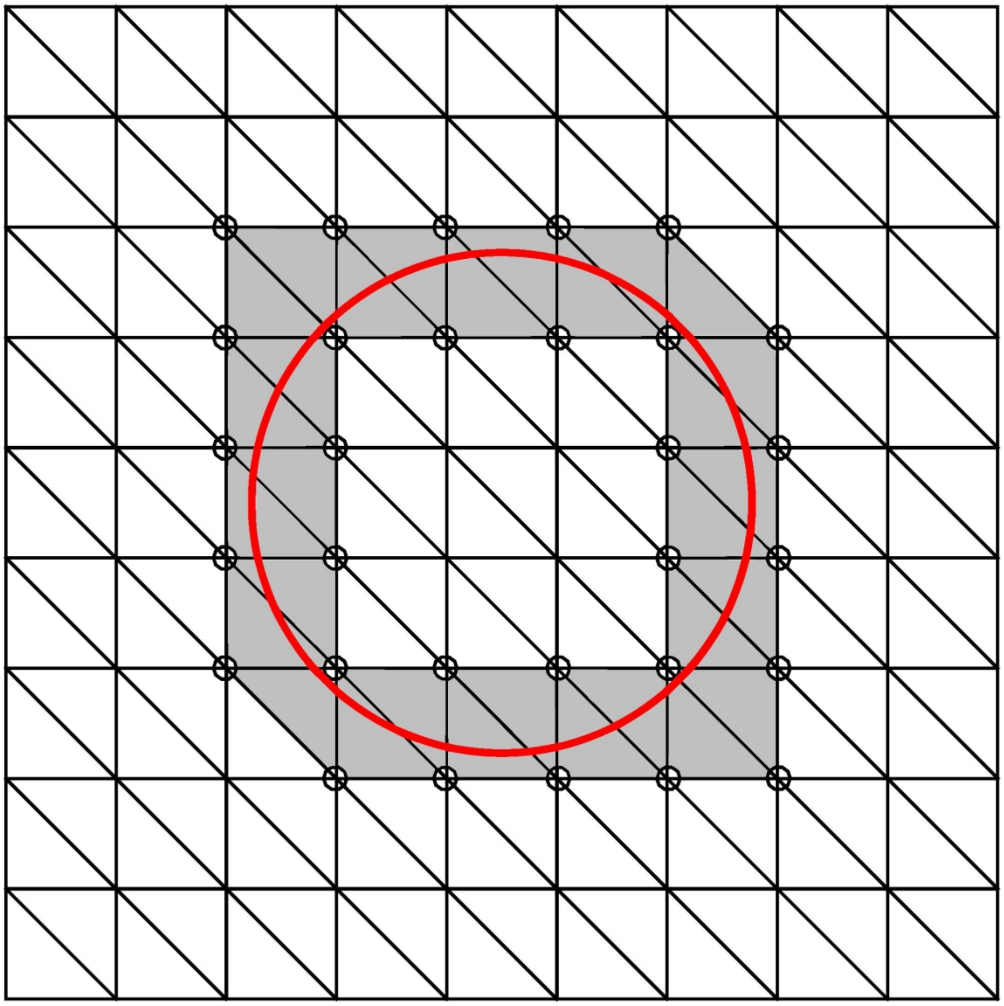

Surface elasticity is taken into account in the plane strain model. (c) X-FEM mesh

91x91mm (600 x 600 DPI)

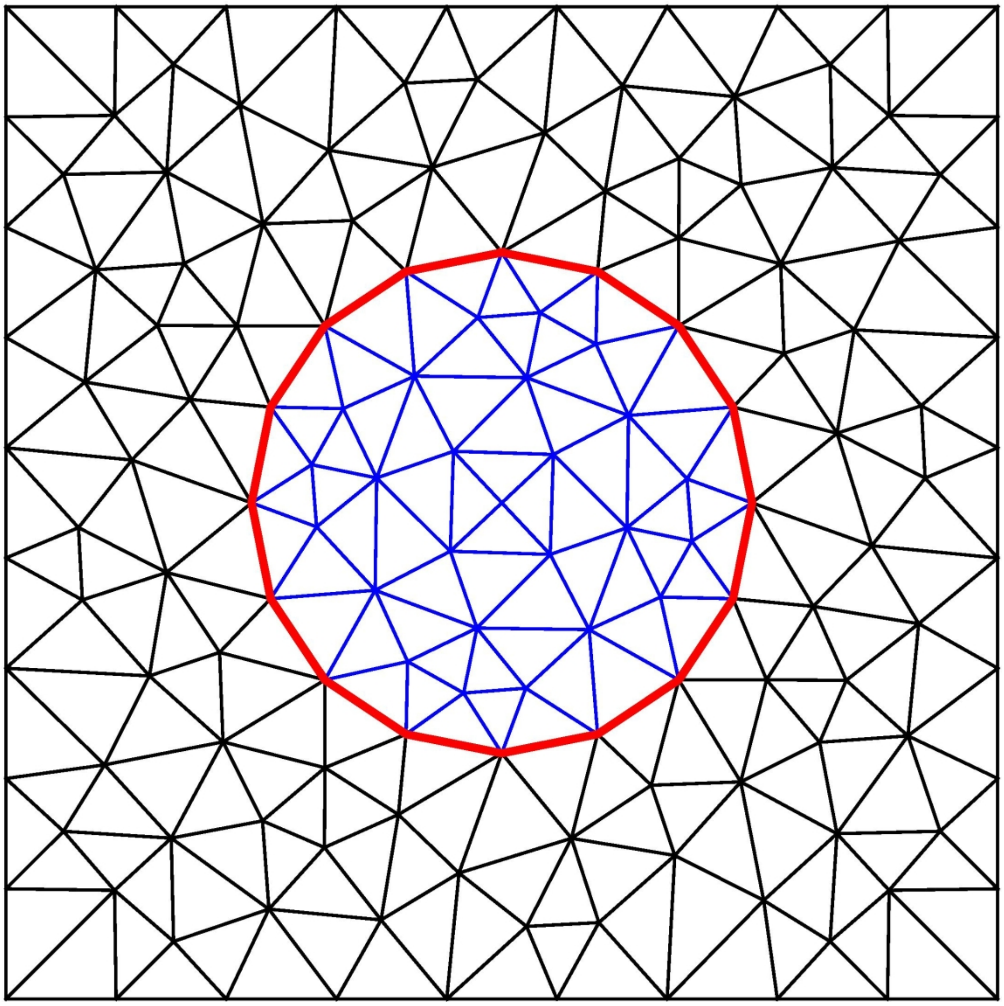

Surface elasticity is taken into account in the plane strain model. (d) Interface element

91x91mm (600 x 600 DPI)

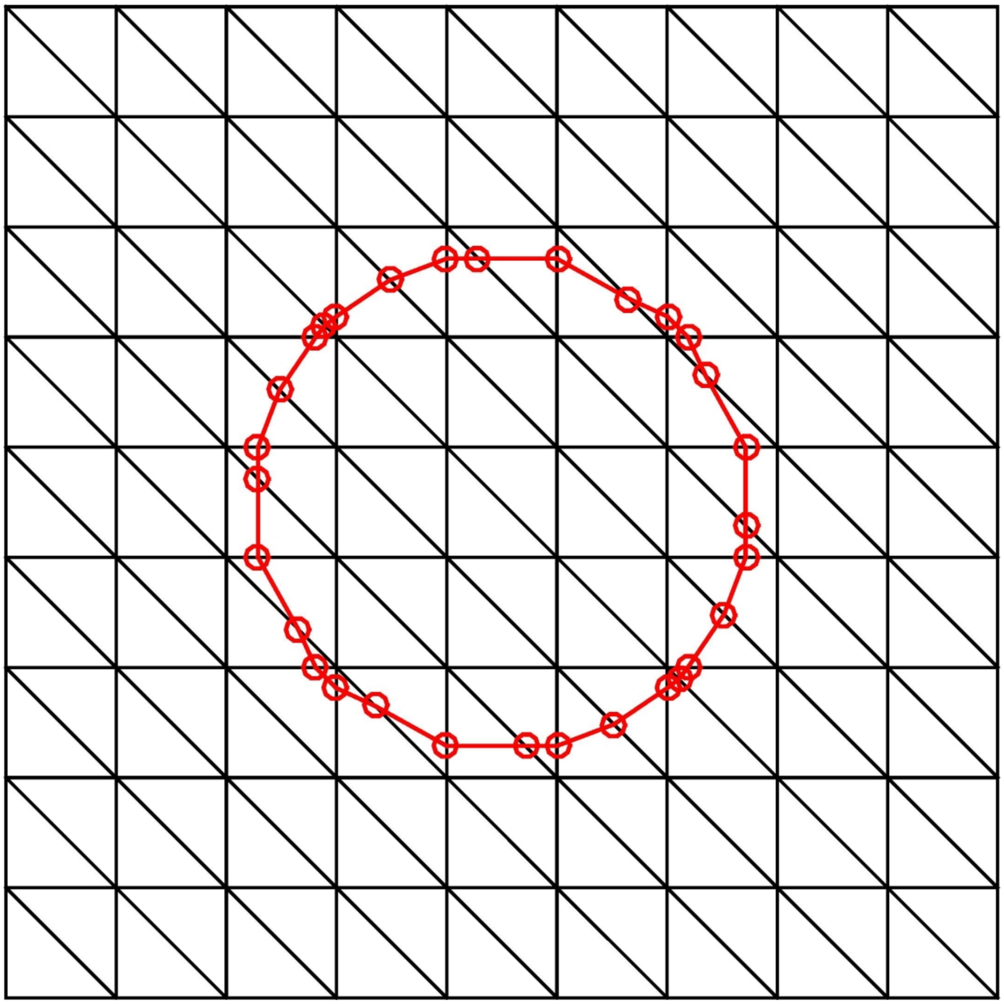

Surface elasticity is taken into account in the plane strain model. (e) E-FEM mesh

91x91mm (600 x 600 DPI)

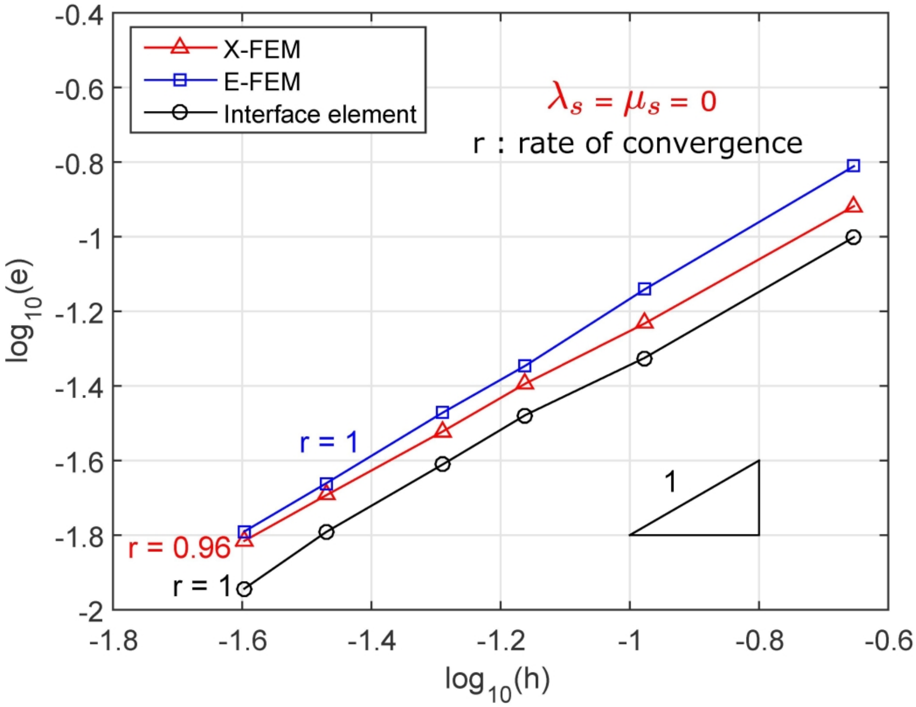

Convergence analysis for the Eshelby problem with and without surface elasticity for the three methods: E-FEM, X-FEM, and Interface element. (a) Without surface elasticity

148x111mm (600 x 600 DPI)

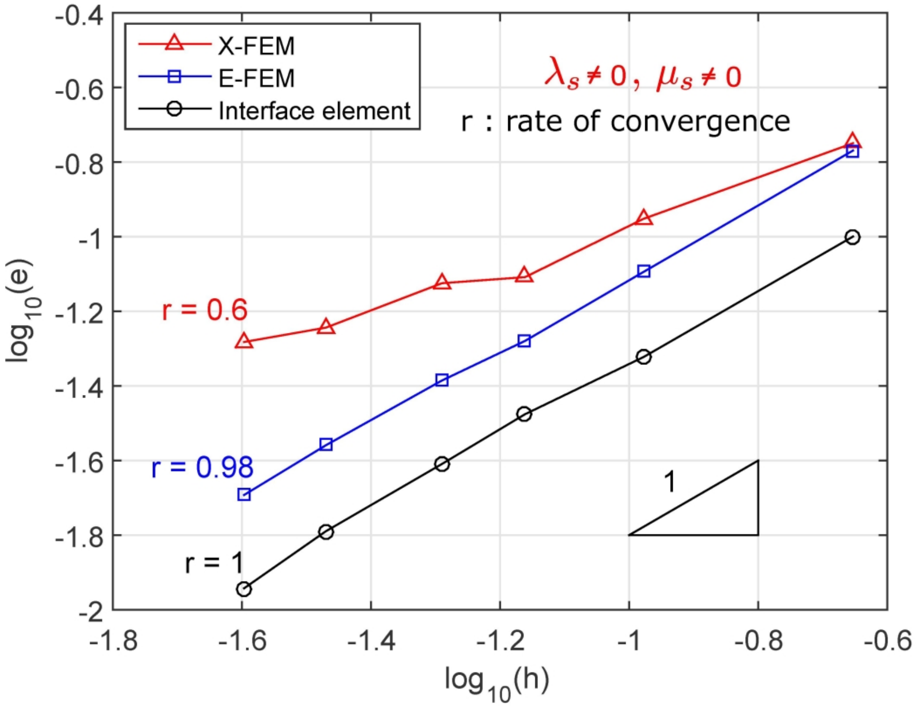

Convergence analysis for the Eshelby problem with and without surface elasticity for the three methods: E-FEM, X-FEM, and Interface element. (b) With surface elasticity

148x111mm (600 x 600 DPI)

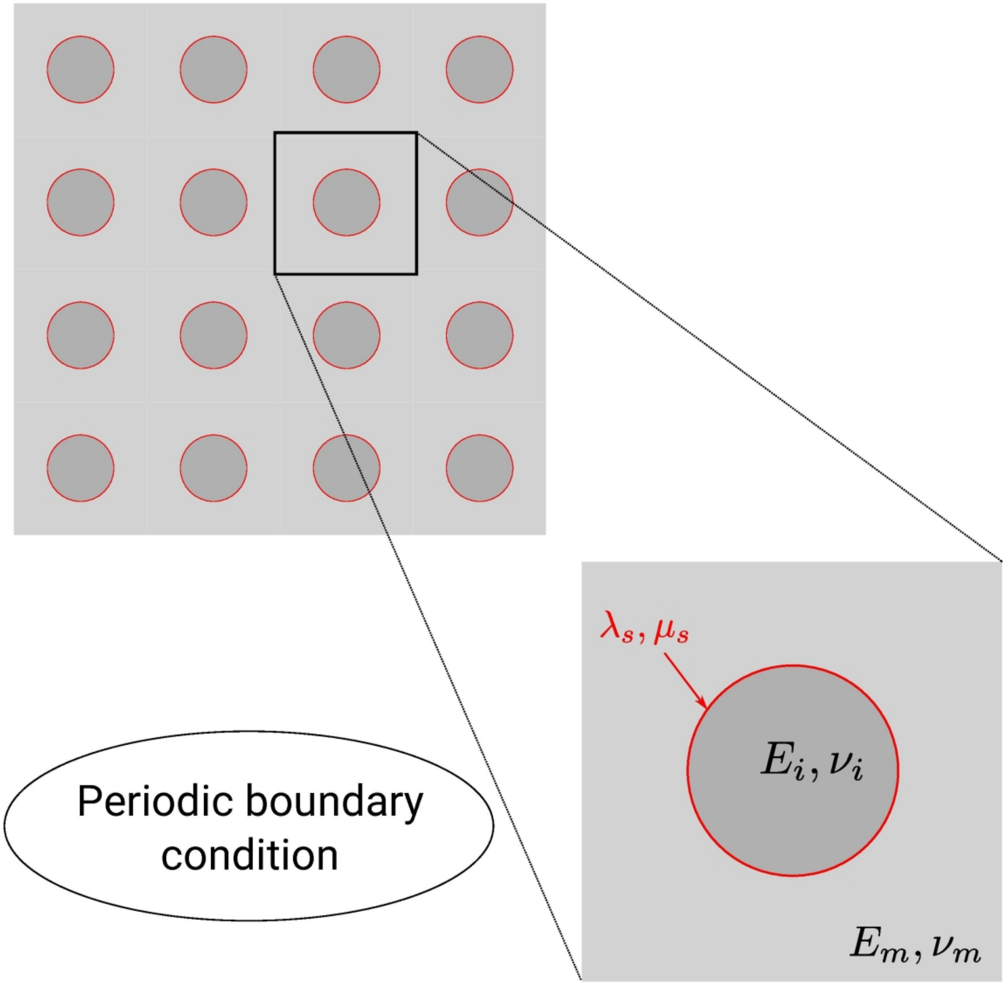

Size effect in effective plane-strain bulk modulus for circular inclusion ($ f=0,2 $, $ E_{m} = 70 $ GPa, $E_{i}=0,1E_{m}$, $\nu_{m} = \nu_{i} = 0,32 $). (a) Periodic microstructure

108x106mm (600 x 600 DPI)

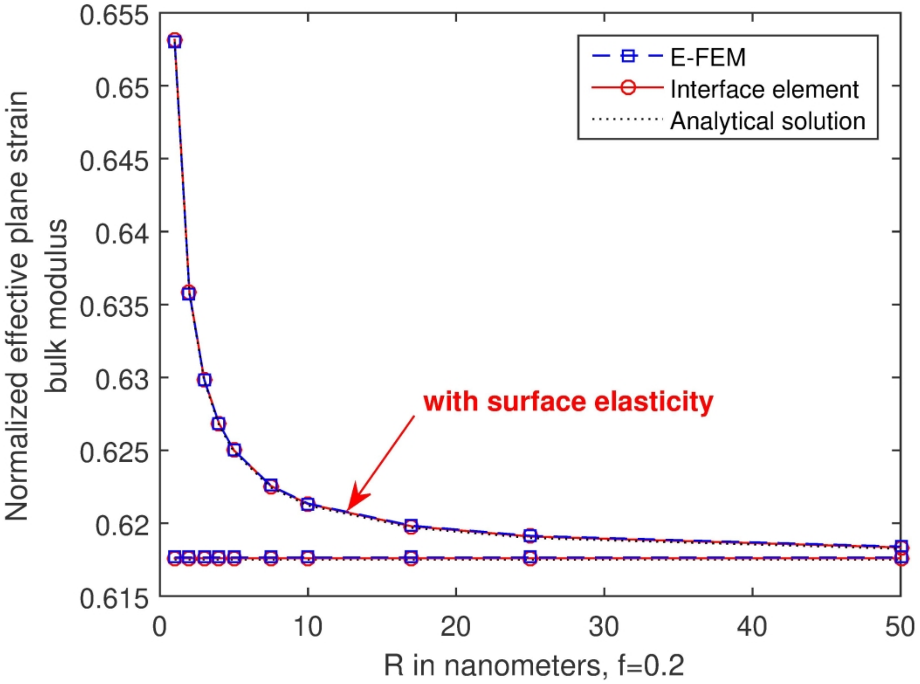

Size effect in effective plane-strain bulk modulus for circular inclusion ($ f=0,2 $, $ E_{m} = 70 $ GPa, $E_{i}=0,1E_{m}$, $\nu_{m} = \nu_{i} = 0,32 $). (b) Normalized effective bulk modulus

151x109mm (600 x 600 DPI)

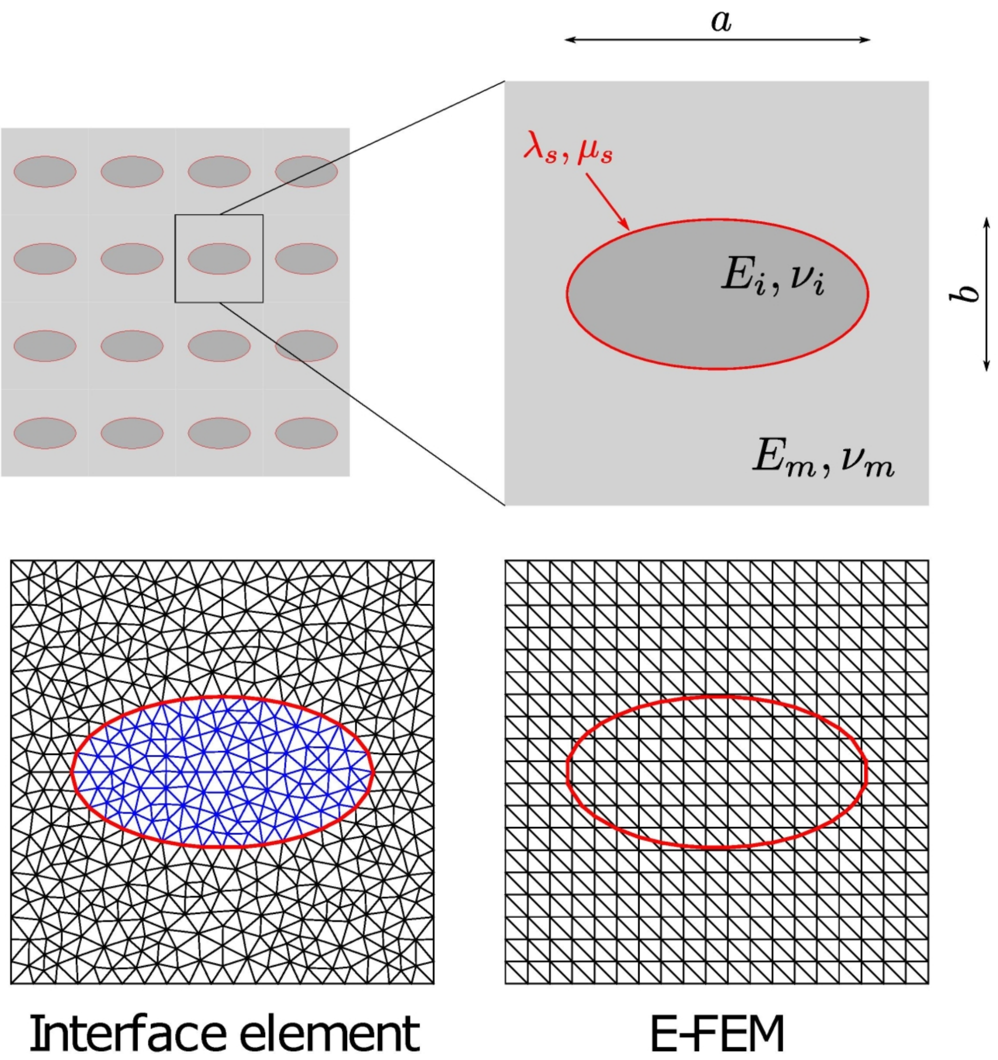

Size effect in effective plane-strain bulk modulus for ellipse inclusion ($ f=0.2 $, $ E_{m} = 70 $ GPa, $E_{i}=0.1E_{m}$, $\nu_{m} = \nu_{i} = 0.32 $). (a) Ellipse cylindrical inclusions

97x101mm (600 x 600 DPI)

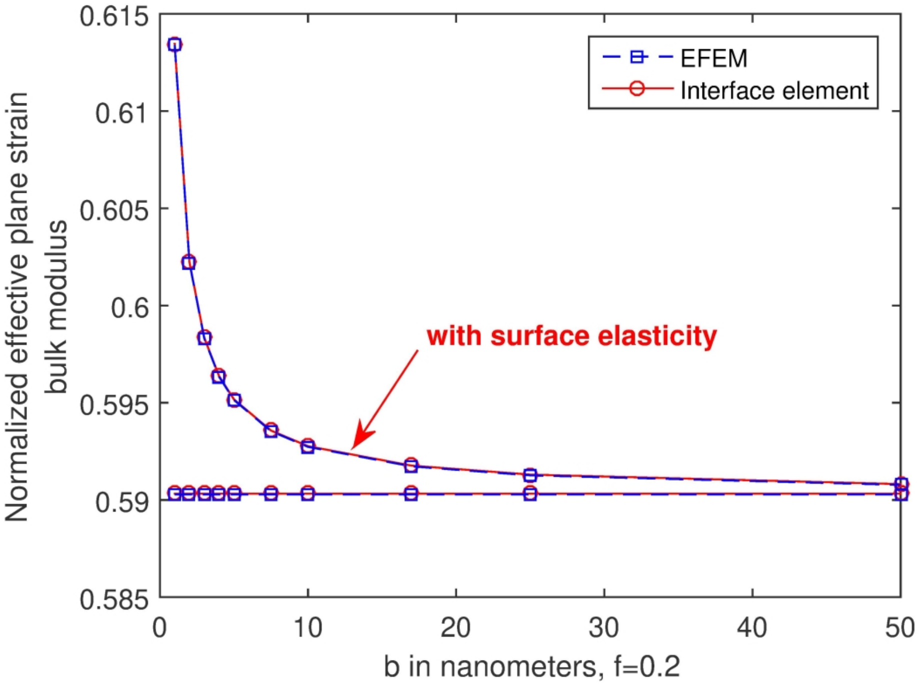

Size effect in effective plane-strain bulk modulus for ellipse inclusion ($ f=0.2 $, $ E_{m} = 70 $ GPa, $E_{i}=0.1E_{m}$, $\nu_{m} = \nu_{i} = 0.32 $). (b) Normalized effective bulk modulus

151x109mm (600 x 600 DPI)

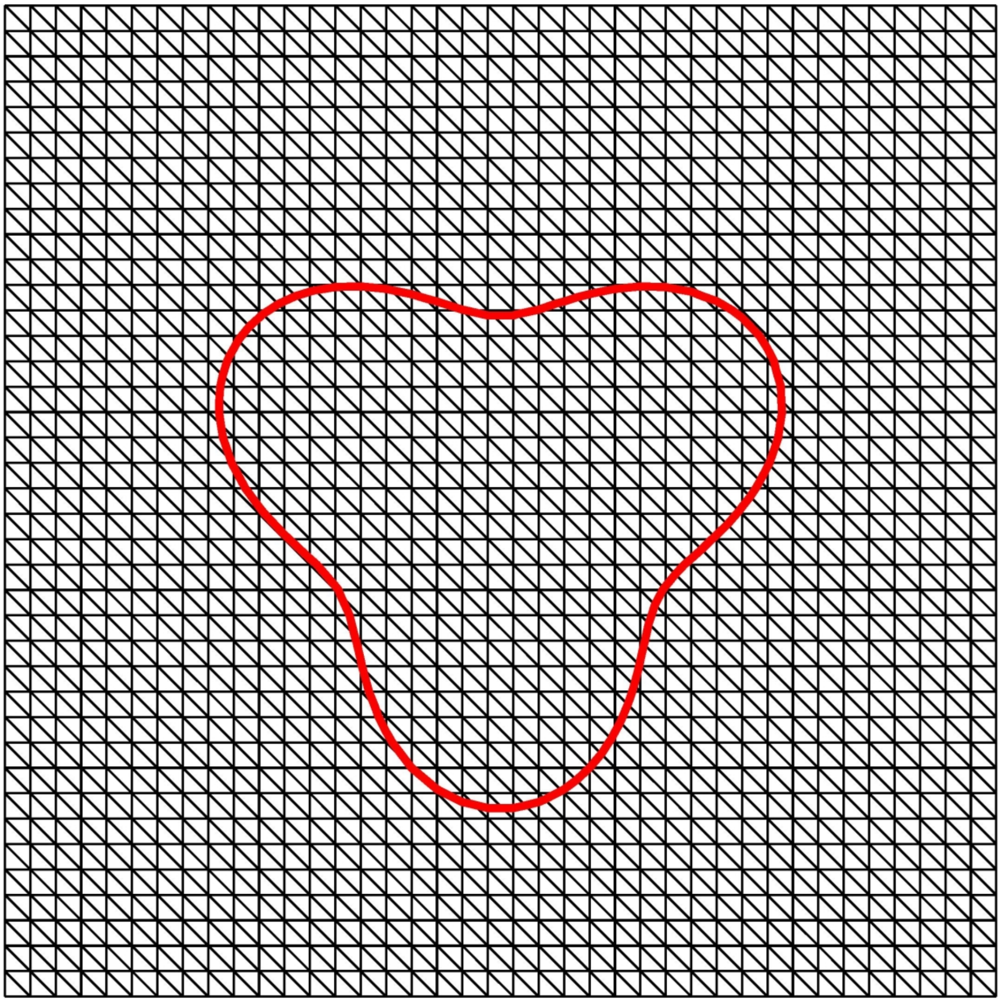

Size effect and shape dependence in normalized effective bulk modulus ($f=0.2$, $E_{m} = 70$ GPa, $E_{i}=0.1E_{m}$, $\nu_{m} = \nu_{i} = 0.32$). (a) $A=0.25R_{o}$ and $B = 3$

91x91mm (600 x 600 DPI)

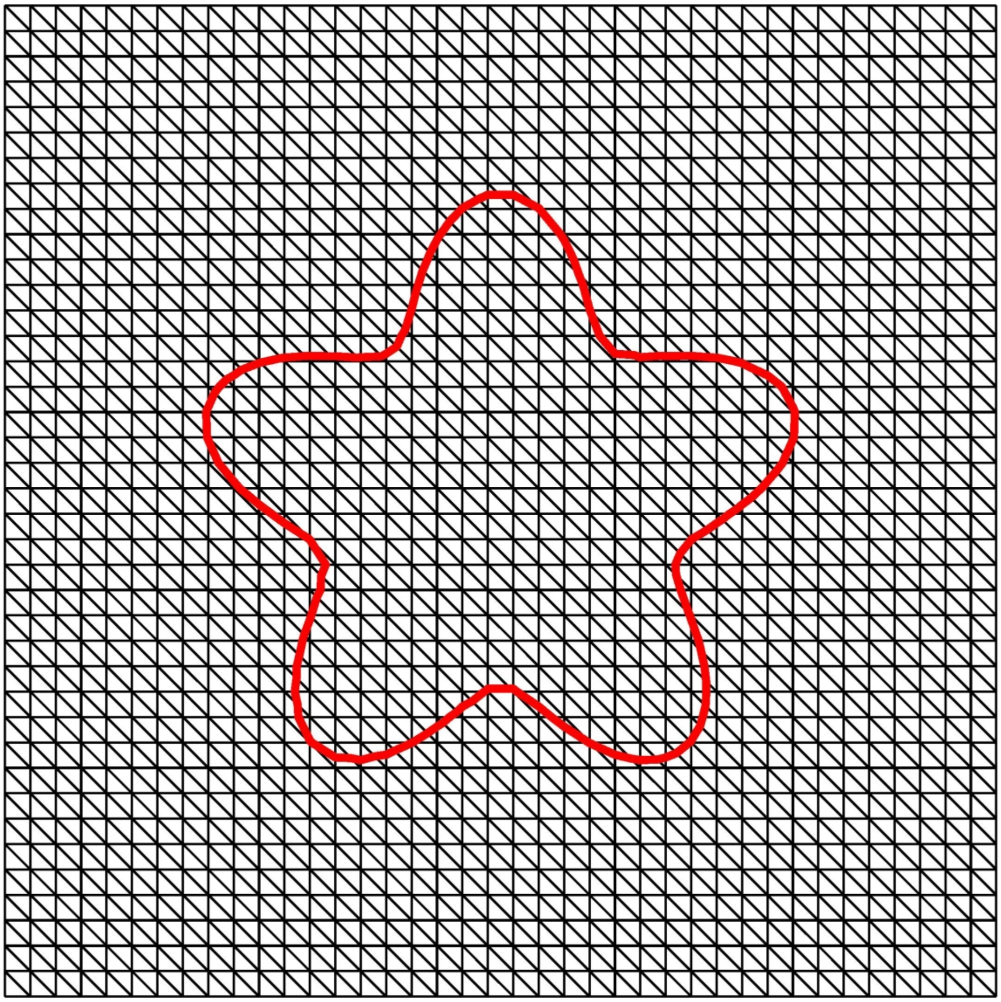

Size effect and shape dependence in normalized effective bulk modulus ($f=0.2$, $E_{m} = 70$ GPa, $E_{i}=0.1E_{m}$, $\nu_{m} = \nu_{i} = 0.32$). (b) $A=0.25R_{o}$ and $B = 5$

91x91mm (600 x 600 DPI)

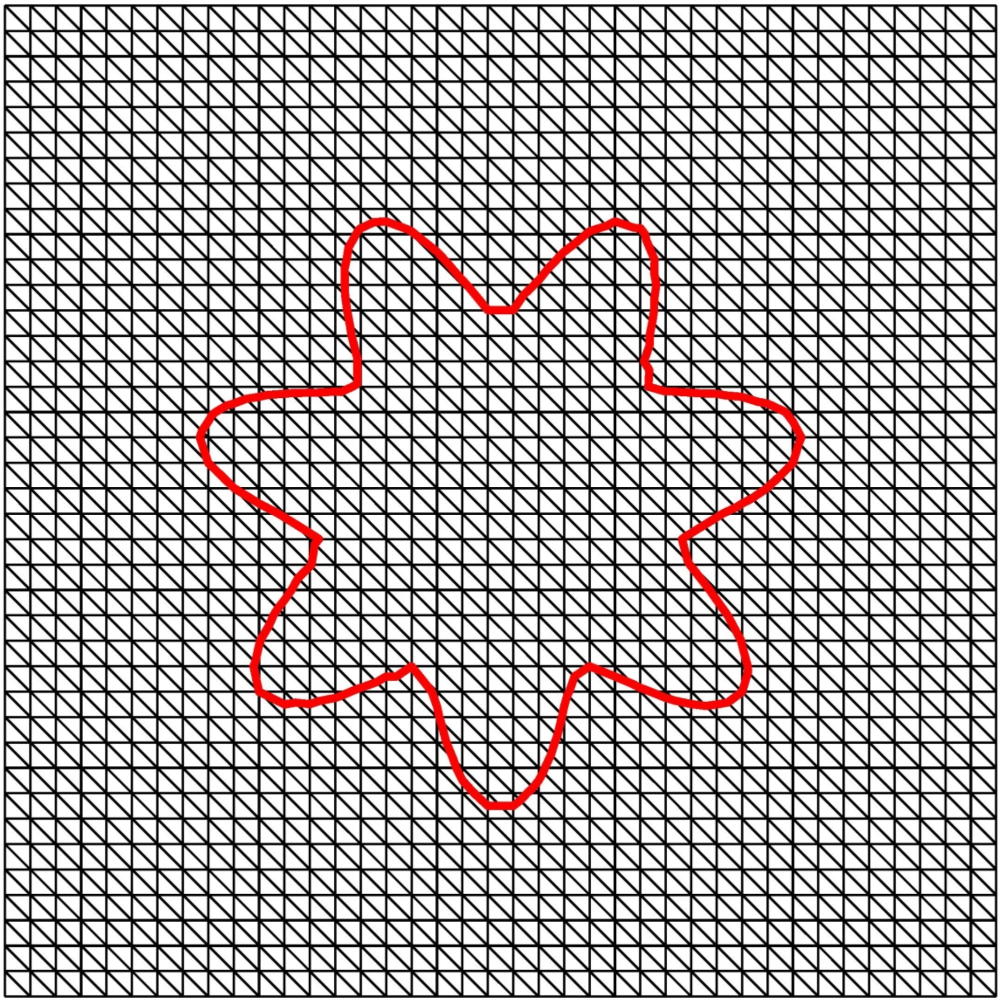

Size effect and shape dependence in normalized effective bulk modulus ($f=0.2$, $E_{m} = 70$ GPa, $E_{i}=0.1E_{m}$, $\nu_{m} = \nu_{i} = 0.32$). (c) $A=0.25R_{o}$ and $B = 7$

91x91mm (600 x 600 DPI)

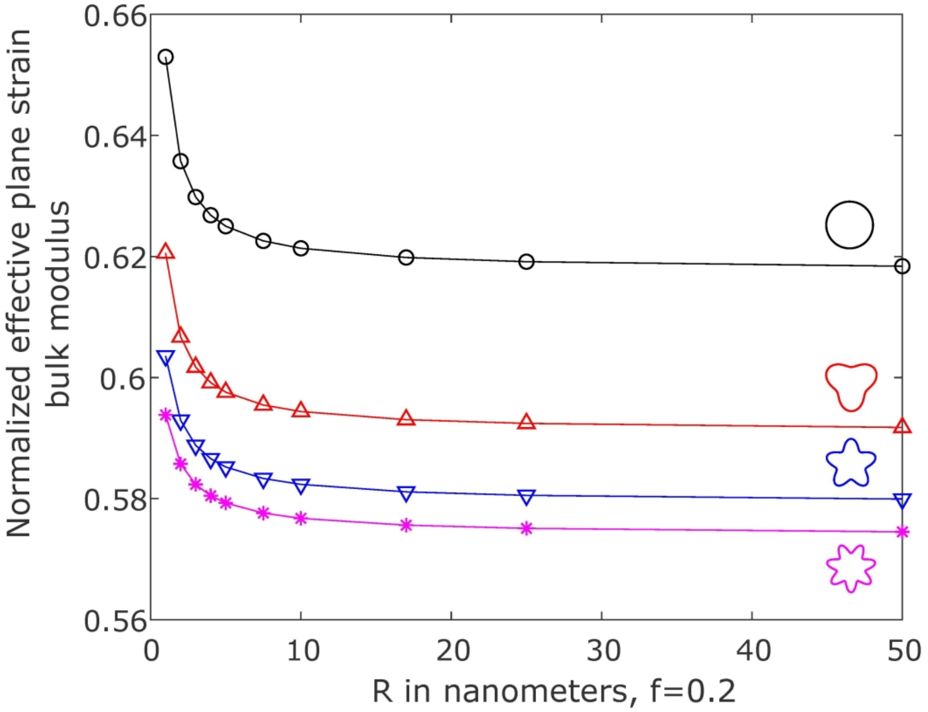

Size effect and shape dependence in normalized effective bulk modulus ($ f=0.2 $, $ E_{m} = 70 $ GPa, $E_{i}=0.1E_{m}$, $\nu_{m} = \nu_{i} = 0.32 $). (d) Normalized effective bulk modulus

148x111mm (600 x 600 DPI)

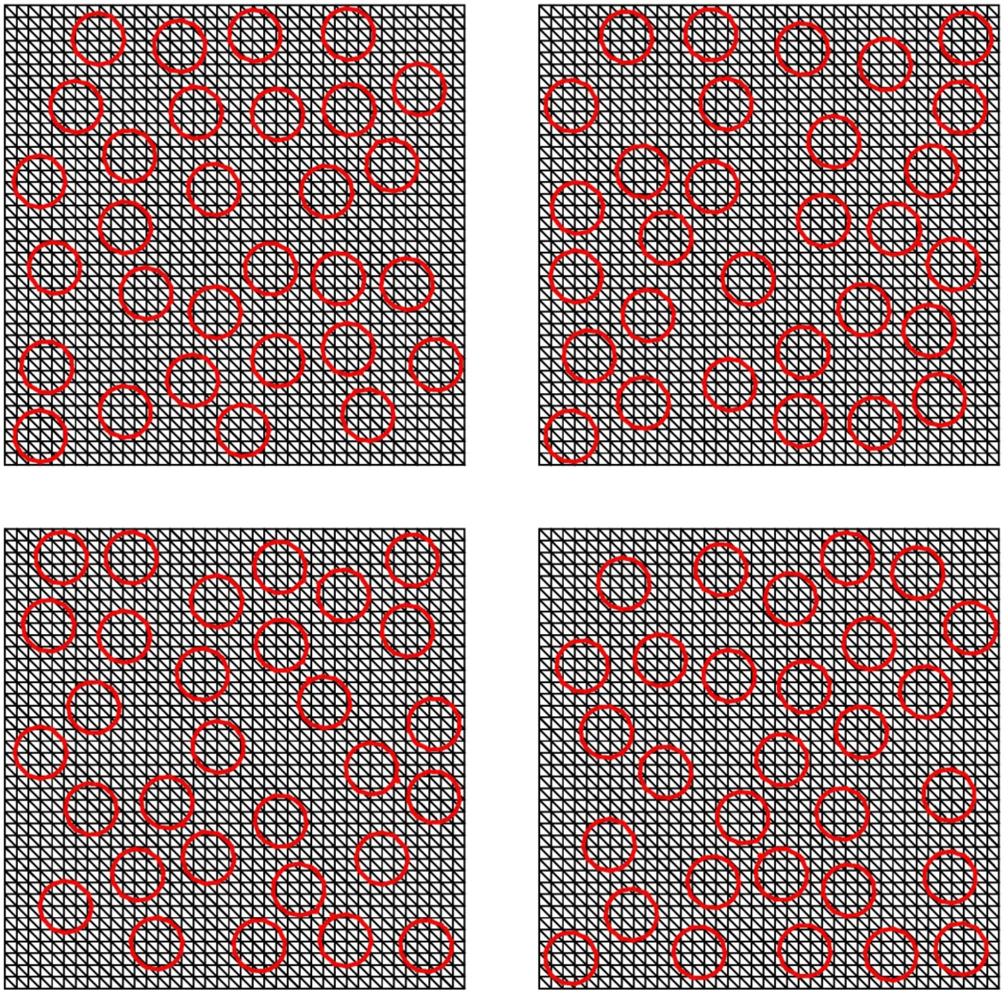

Several samples for 30 randomly distributed nano-inclusions. (a) E-FEM

91x90mm (600 x 600 DPI)

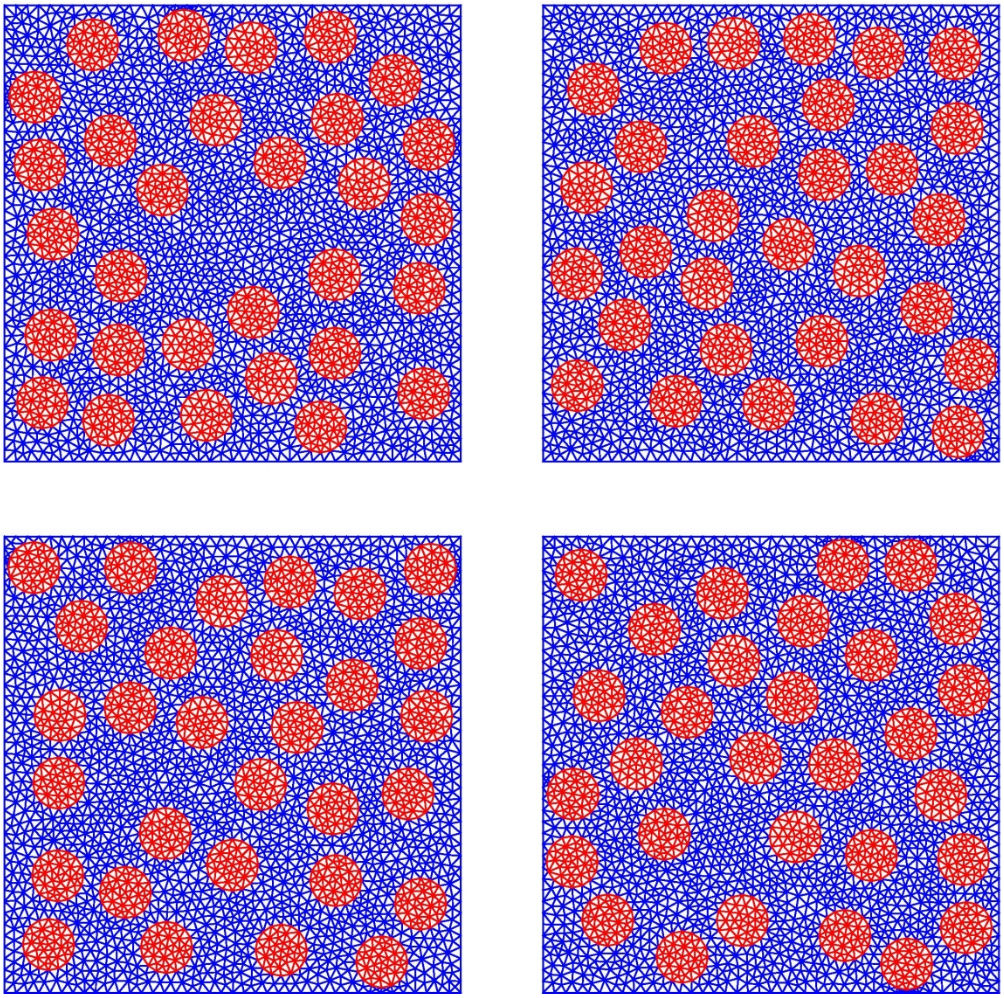

Several samples for 30 randomly distributed nano-inclusions. (b) Interface element

92x91mm (600 x 600 DPI)

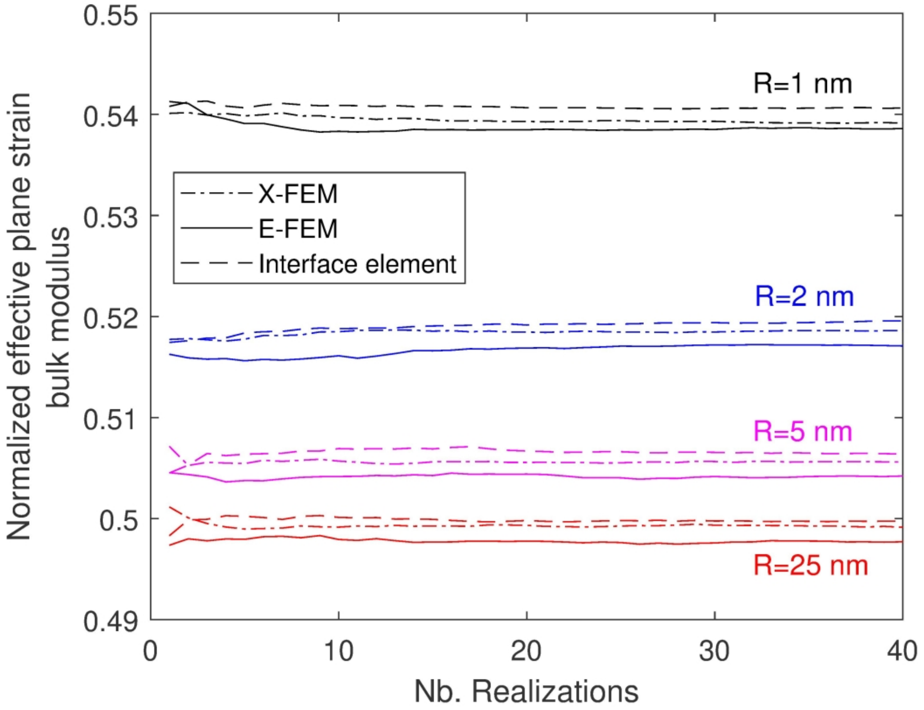

Size effect for effective plane-strain bulk modulus with randomly distributed nano-inclusions ($ f=0.3 $, $ E_{m} = 70 $ GPa, $E_{i}=0.1E_{m}$, $\nu_{m} = \nu_{i} = 0.32; $ $ \lambda_{s} = 6.842 $ N/m, $ \mu_{s} = -0.375 $ N/m, corresponding to $ k_{s} = 6.092 $ N/m). (a) Statistical convergence

148x111mm (600 x 600 DPI)

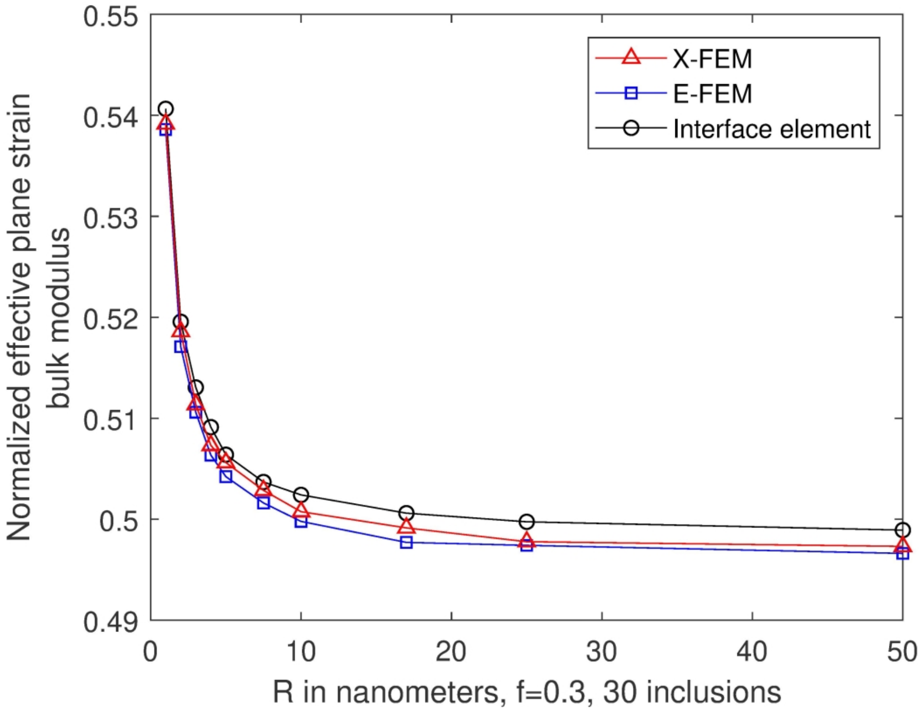

Size effect for effective plane-strain bulk modulus with randomly distributed nano-inclusions ($ f=0.3 $, $ E_{m} = 70 $ GPa, $E_{i}=0.1E_{m}$, $\nu_{m} = \nu_{i} = 0.32; $ $ \lambda_{s} = 6.842 $ N/m, $ \mu_{s} = -0.375 $ N/m, corresponding to $ k_{s} = 6.092 $ N/m). (b) Size effect

148x111mm (600 x 600 DPI)

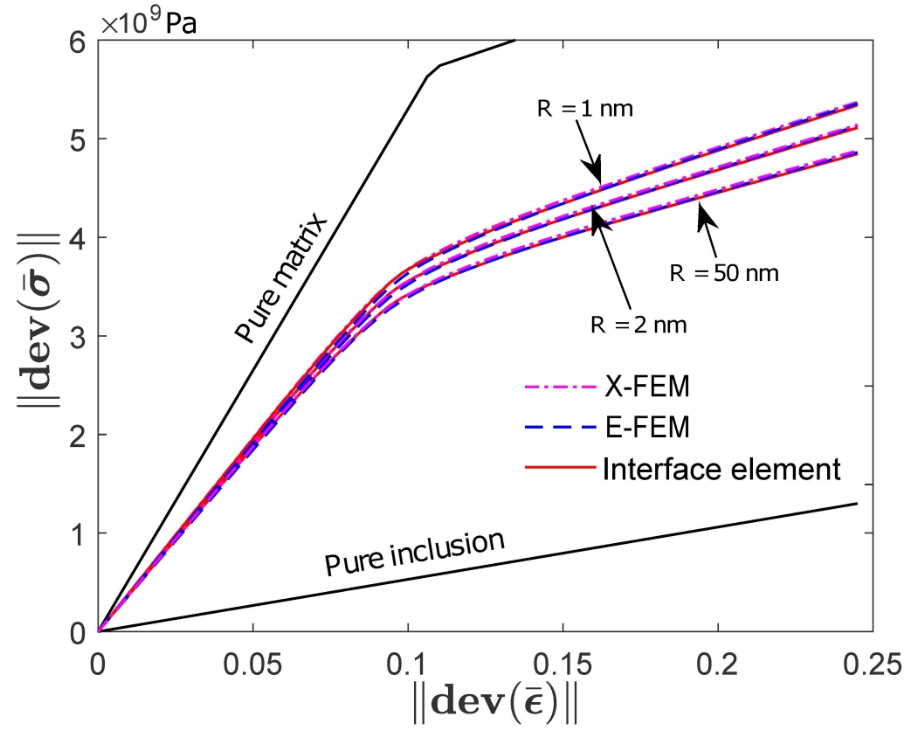

Homogenized elastoplastic behavior for three different radii of nano-inclusion using X-FEM, E-FEM and Interface element approach for a tensile test with prescribed macroscopic strain $ \epsilon_{11}^{M} = 0.3, \epsilon_{22}^{M} = \epsilon_{33}^{M} = \epsilon_{12}^{M} = 0 $.

148x111mm (600 x 600 DPI)

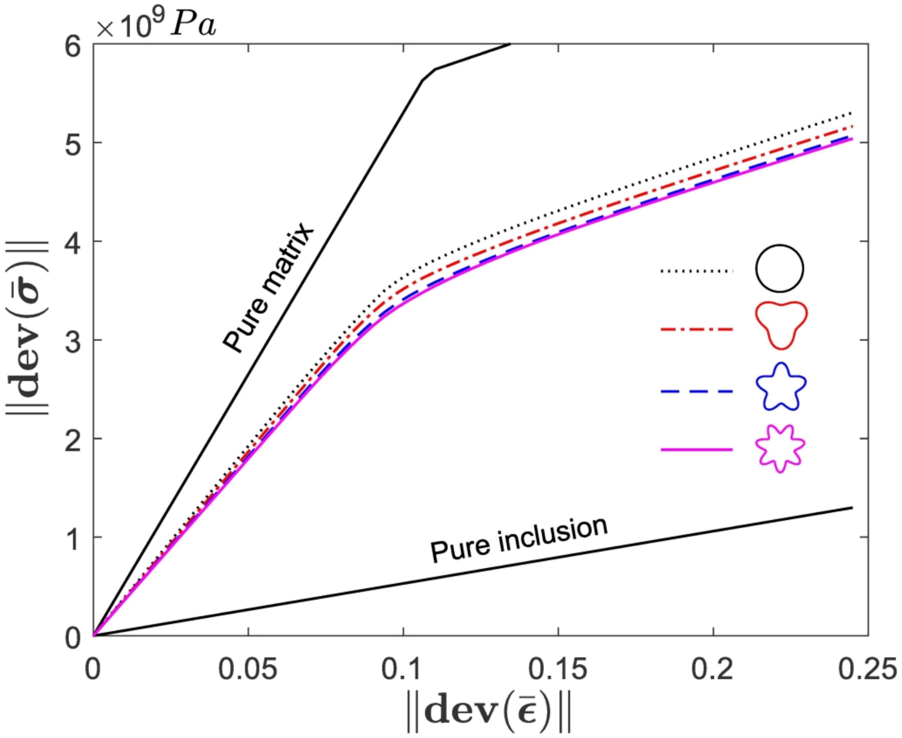

Homogenized elastoplastic behavior for different shapes of inclusion.

148x111mm (600 x 600 DPI)

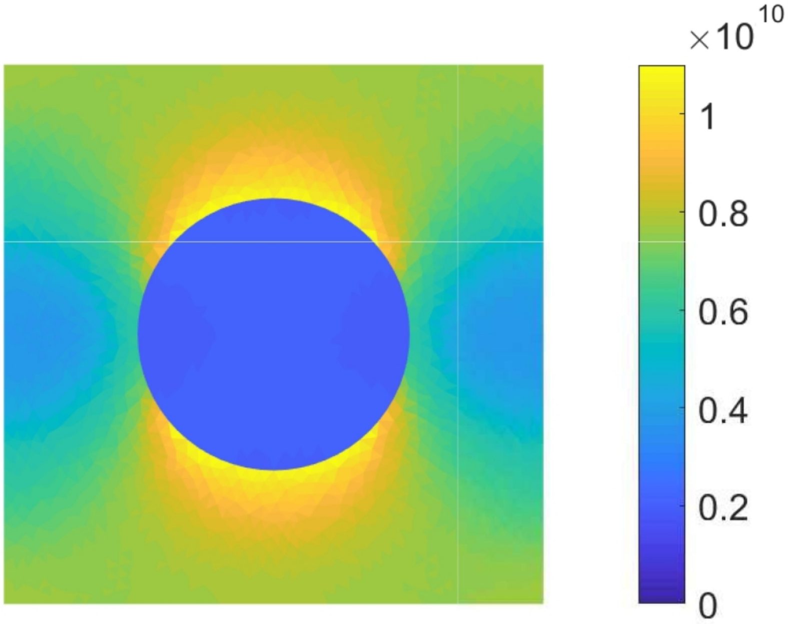

Comparison of the norm of deviatoric stress tensor $ \parallel \text{dev} (\bldsig) \parallel $ (Pa) obtained from the three numerical approaches at the end of the test for R = 1 nm and R = 50 nm.

148x111mm (300 x 300 DPI)

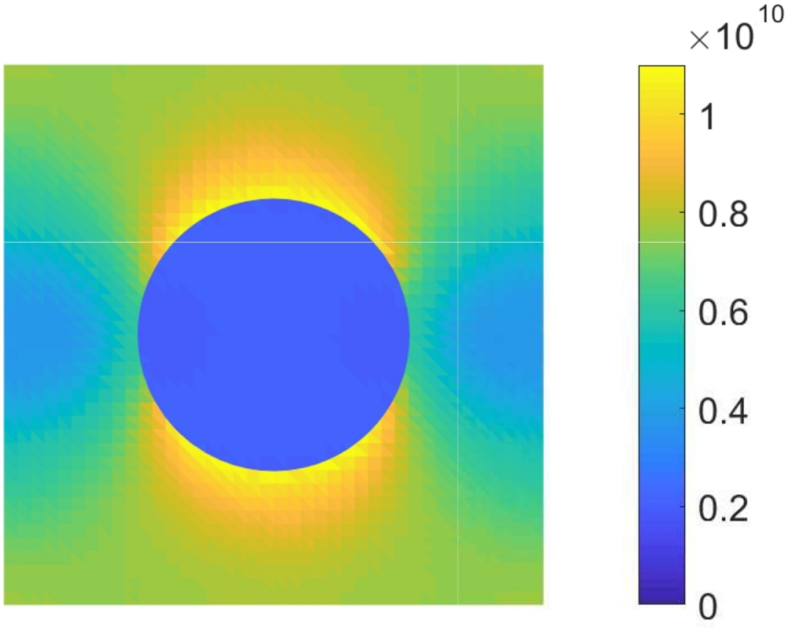

Comparison of the norm of deviatoric stress tensor $ \parallel \text{dev} (\bldsig) \parallel $ (Pa) obtained from the three numerical approaches at the end of the test for R = 1 nm and R = 50 nm.

148x111mm (300 x 300 DPI)

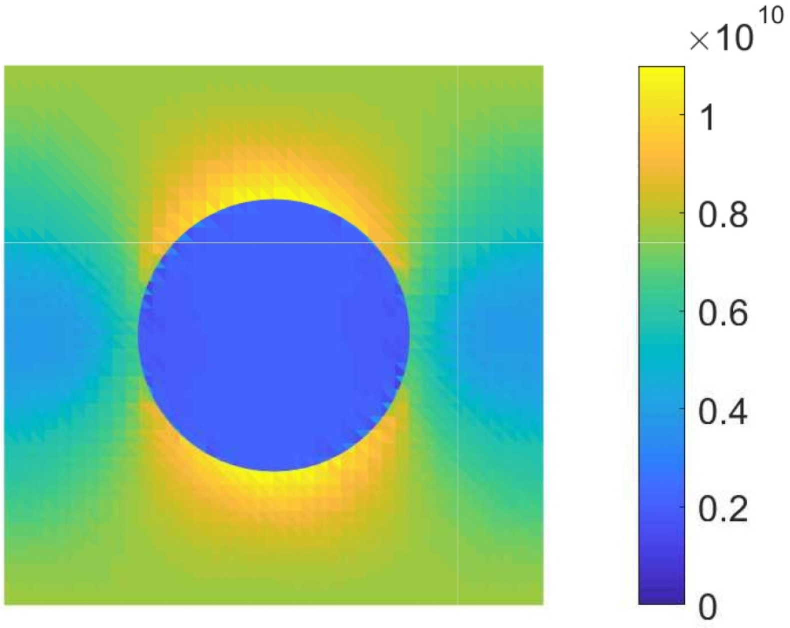

Comparison of the norm of deviatoric stress tensor $ \parallel \text{dev} (\bldsig) \parallel $ (Pa) obtained from the three numerical approaches at the end of the test for R = 1 nm and R = 50 nm.

148x111mm (300 x 300 DPI)

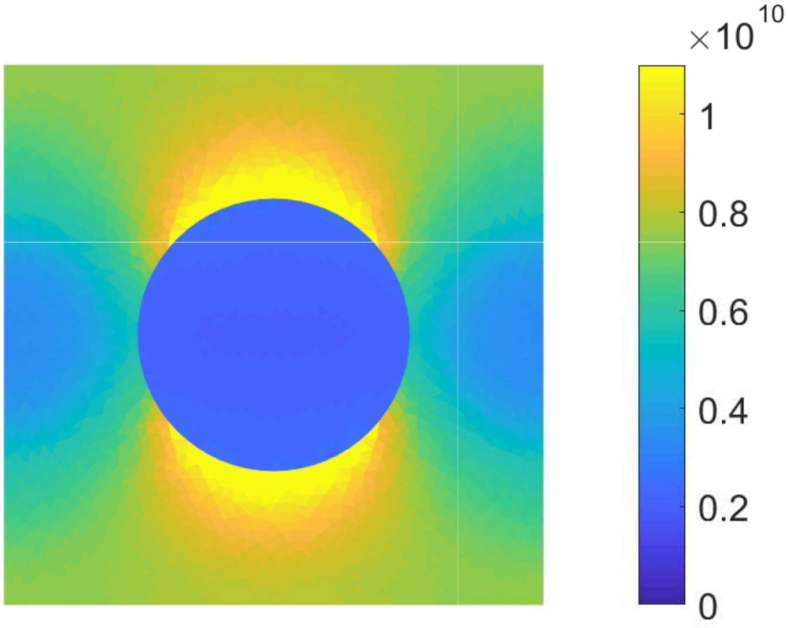

Comparison of the norm of deviatoric stress tensor $ \parallel \text{dev} (\bldsig) \parallel $ (Pa) obtained from the three numerical approaches at the end of the test for R = 1 nm and R = 50 nm.

148x111mm (300 x 300 DPI)

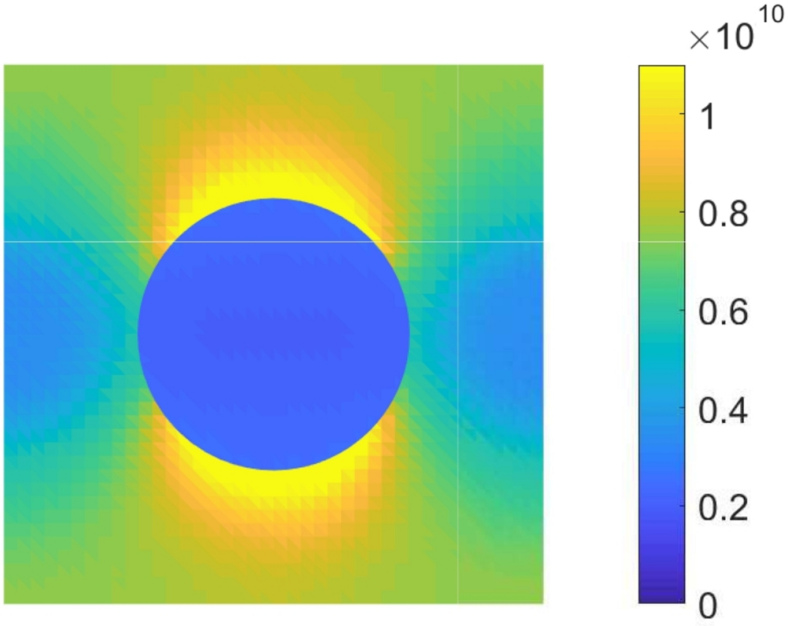

Comparison of the norm of deviatoric stress tensor $ \parallel \text{dev} (\bldsig) \parallel $ (Pa) obtained from the three numerical approaches at the end of the test for R = 1 nm and R = 50 nm.

148x111mm (300 x 300 DPI)

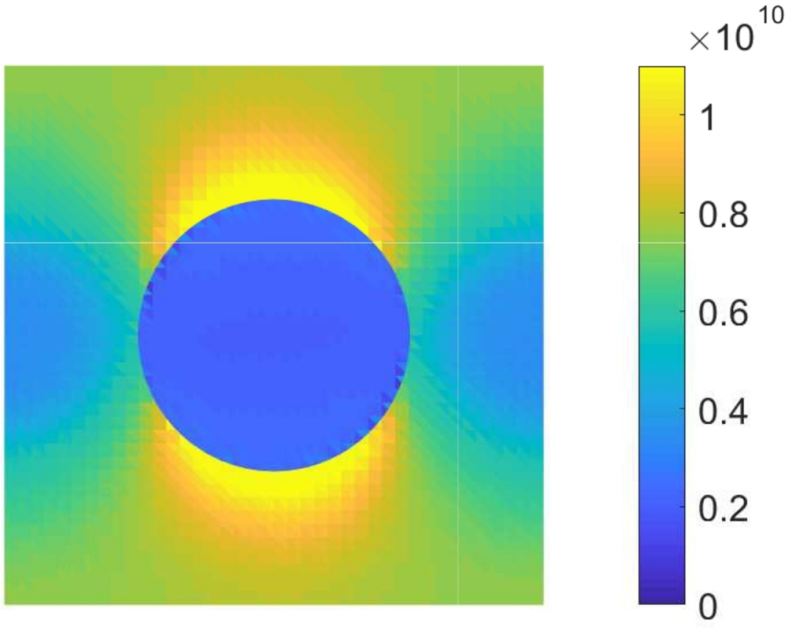

Comparison of the norm of deviatoric stress tensor $ \parallel \text{dev} (\bldsig) \parallel $ (Pa) obtained from the three numerical approaches at the end of the test for R = 1 nm and R = 50 nm.

148x111mm (300 x 300 DPI)

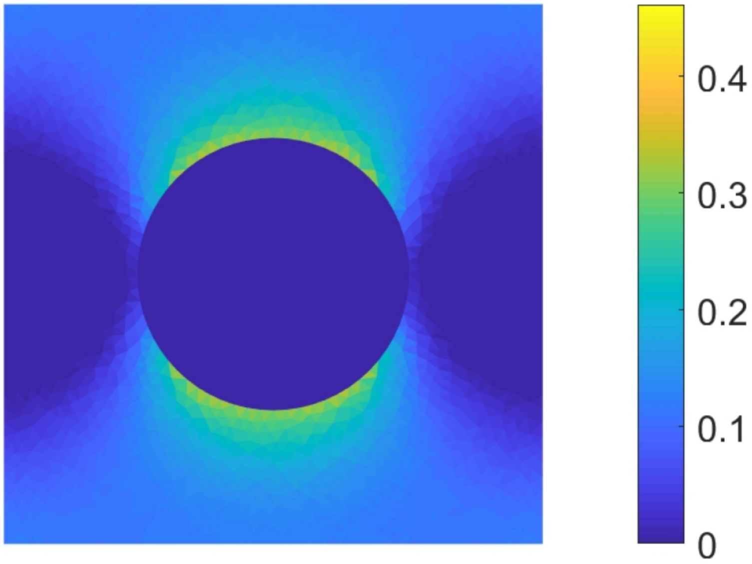

Comparison of the cumulative plastic deformation obtained from the three numerical approaches at the end of the test for R = 1 nm and R = 50 nm.

148x111mm (300 x 300 DPI)

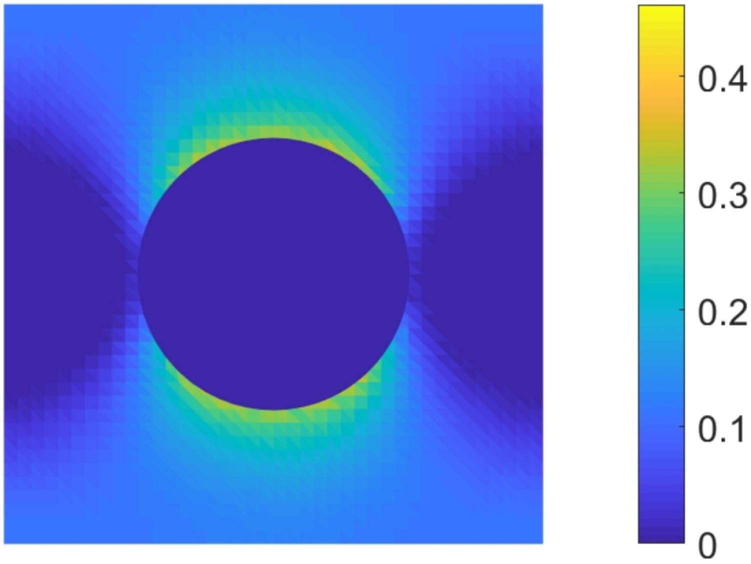

Comparison of the cumulative plastic deformation obtained from the three numerical approaches at the end of the test for R = 1 nm and R = 50 nm.

148x111mm (300 x 300 DPI)

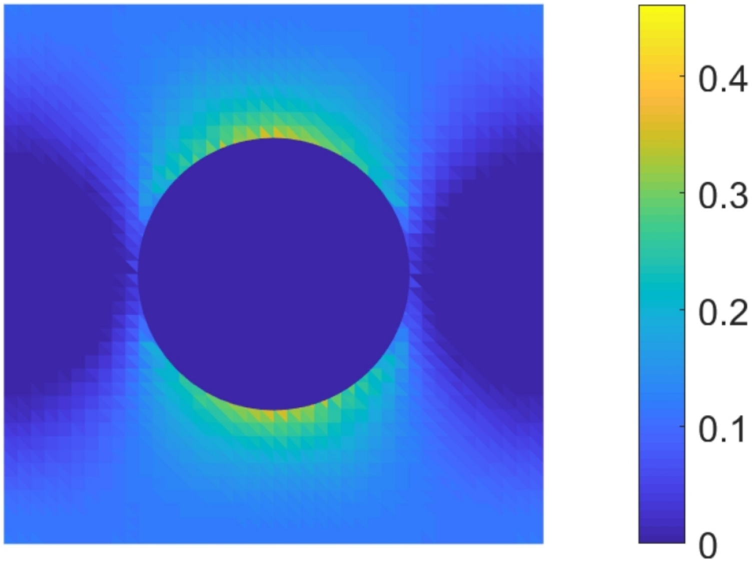

Comparison of the cumulative plastic deformation obtained from the three numerical approaches at the end of the test for R = 1 nm and R = 50 nm.

148x111mm (300 x 300 DPI)

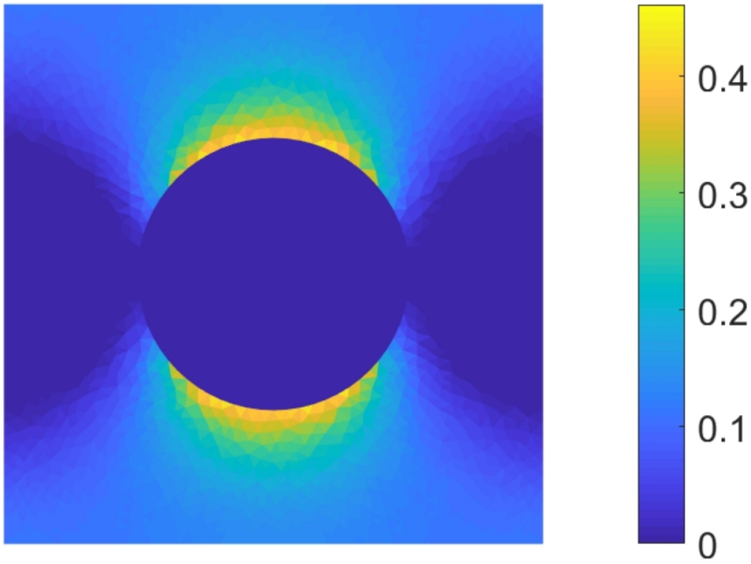

Comparison of the cumulative plastic deformation obtained from the three numerical approaches at the end of the test for R = 1 nm and R = 50 nm.

148x111mm (300 x 300 DPI)

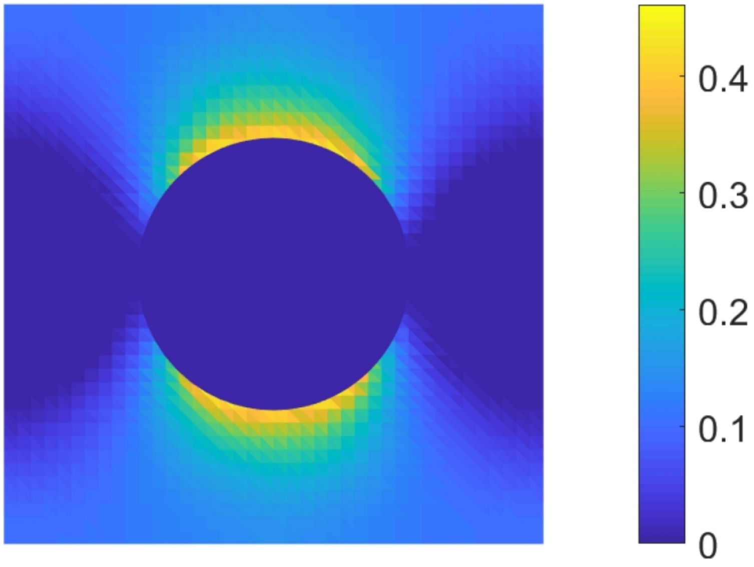

Comparison of the cumulative plastic deformation obtained from the three numerical approaches at the end of the test for R = 1 nm and R = 50 nm.

148x111mm (300 x 300 DPI)

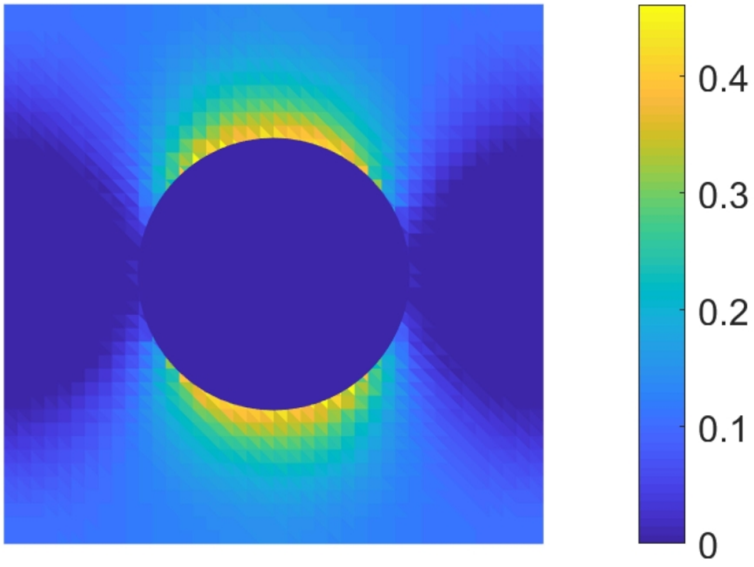

Comparison of the cumulative plastic deformation obtained from the three numerical approaches at the end of the test for R = 1 nm and R = 50 nm.

148x111mm (300 x 300 DPI)